MODELLING THE INORGANIC OCEAN CARBON CYCLE UNDER PAST AND FUTURE CLIMATE CHANGE

by

Tracy L. Ewen

B.Sc., University of Manitoba, 1996
M.Sc., University of Manitoba, 1999

A Dissertation Submitted in Partial Fulfillment of the
Requirements for the Degree of

DOCTOR OF PHILOSOPHY

in the School of Earth and Ocean Sciences

University of Victoria

Supervisor: Professor Andrew J. Weaver

Abstract

The increase in atmospheric CO_2 concentration over the last 150 years is unprecedented during the past 420,000 years of Earth's history. The oceans are the largest sink for CO_2 and it is unknown how the ocean carbon cycle will respond to increasing anthropogenic CO_2 concentrations in the future. It is possible that climate feedbacks may act to reduce further uptake of carbon by the ocean. This thesis examines the inorganic ocean carbon cycle and how climate feedbacks influence future uptake using a coupled ocean-atmosphere-sea ice model with an inorganic carbon component. Past climate transitions are also studied, including both abrupt and glacial-interglacial climate transitions.

The sensitivity of the inorganic carbon cycle to increased atmospheric CO_2 is examined and atmospheric carbon dioxide levels are projected under global warming scenarios. A transient weakening of the North Atlantic overturning is found in most simulations and increased SSTs are found in all simulations. Although these positive feedbacks act on the carbon system to reduce uptake, the ocean has the capacity to take up 65-75% of the anthropogenic CO_2 increase once the forcing is stopped. The effects of climate feedbacks on future carbon uptake are analyzed and it is found that the ocean stores 7% more carbon when there are no climate feedbacks acting on the system. Sensitivity experiments are conducted with respect to the representation of ocean mixing and sea ice dynamics. The inclusion of the Gent McWilliams parameterization for mixing associated with mesoscale eddies leads to a further 6% increase in oceanic uptake, whereas the inclusion of sea ice dynamics leads to a 2% global difference in uptake.

Past climates have been marked by abrupt transitions from cold to warm states and mechanisms which led to these transitions most likely include variability in the thermohaline circulation (THC). Changes in atmospheric CO_2 concentration that arise during abrupt climate change events are investigated. This is accomplished through the use of meltwater pulse scenarios applied to the coupled model. Transient simulations are carried out under a glacial equilibrium climate with increased freshwater discharge to high latitude regions in both hemispheres in order to simulate meltwater episodes. Changes in ocean circulation and carbon solubility are found to lead to significant increases in atmospheric CO_2 concentrations when meltwater

episodes are simulated in both hemispheres. The magnitude of increase in atmospheric CO_2 is between 10-40 ppmv, which accounts for some of the changes in CO_2 as recorded in the ice core records.

The response of the carbon cycle during glacial-interglacial transition is investigated by applying 8 kyr BP boundary conditions to an LGM equilibrium climate. An LGM equilibrium with orbital parameters set to 21 kyr BP and CO_2 radiative forcing to 200 ppmv is used and 8 kyr BP boundary conditions, namely orbital parameters for 8 kyr BP and CO_2 radiative forcing of 280 ppmv, are then imposed on this equilibrium. Atmospheric CO_2 is then allowed to evolve and we find an increase of only $\sim$ 5 ppmv. Changes due to CO_2 radiative forcing alone account for almost all of the change in atmospheric CO_2 with effects of changing the orbital parameters almost negligible on global carbon uptake. It is suggested that the the inclusion of both biological and carbonate pumps may be important components to unlocking the mystery surrounding the glacial-interglacial cycles.

Acknowledgement

I would like to thank NSERC and the University of Victoria for scholarship funding during my PhD program and Andrew Weaver for financial support and the opportunity to attend conferences and summer schools over the last few years. I would also like to thank Andrew for allowing me to continue my work while living in Switzerland over the last year and a half. In the Climate Modelling Group I would like to thank Ed Wiebe and Mike Eby for technical and modelling support, Wanda Lewis for taking care of all the paper work and everyone else in the lab for their friendship and support both at work and outside of work during my time spent in Victoria. While living in Switzerland, I would like to thank the Theoretical Physics group at the University of Zürich for welcoming me and giving me a space to work. Lastly, I would like to thank Oleg Saenko, Gus Fanning, Daithi Stone, Linda Waterman and Andreas Schmittner for many interesting scientific discussions and Joachim Stadel for being my biggest source of scientific inspiration over the years.

Table of Contents

List of Tables

List of Figures

1 Introduction

The increase in atmospheric CO_2 concentration from ~280 ppmv in 1750 to today's values of ~370 ppmv are unprecedented during the past 420,000 years (Petit et al., 1999), and likely during the past 20 million years of Earth's history (Pagani et al., 1999; Pearson and Palmer, 2000). This increase is primarily due to fossil fuel burning and secondarily to land use changes including deforestation. An increase in greenhouse gases acts to perturb the radiation balance of the earth. The amount of outgoing longwave radiation near the surface that is re-radiated to earth increases with increasing greenhouse gases, thereby warming the surface. CO_2 is the dominant anthropogenic greenhouse gas accounting for ~60% of the increase in radiative forcing among all greenhouse gases (Farquhar et al., 2001). This increased radiative forcing acts to change Earth's climate and it is not known how these changes will affect the global carbon cycle.

1.1 The carbon cycle

The oceans are the largest reservoir for CO_2 and the amount of dissolved inorganic carbon (hereafter DIC) in the oceans is about 50 times more than that of the atmosphere (Broecker and Peng, 1982) and thus may play a key role in controlling atmospheric CO_2 levels. Uptake of carbon in the oceans is controlled primarily by carbonate chemistry and ocean circulation. CO_2 is more soluble in colder waters and the general pattern of CO_2 flux is outgassing in equatorial regions and uptake in the high latitudes. CO_2 equilibrates quickly at the atmosphere ocean interface (~1 year) and although the deep oceans have a large capacity for further uptake, it is limited by the rate at which the surface layers and deep waters mix. Net heating of the surface waters will tend to decrease CO_2 uptake and net cooling will tend to increase uptake. The transport of ocean carbon is thus connected to the transport of heat in the ocean meridionally via ocean circulation (Broecker and Peng, 1982).

Changes in circulation affect solubility through changes in heat transport, but more immediately through physical transport of the DIC tracer. Transport and storage of carbon in the ocean is carried out by the same mechanisms that govern the transport and storage of heat and freshwater. It is thought that during preindustrial times, carbon was taken up in the northern hemisphere high latitudes and transported to the southern hemisphere where it outgassed and drove a return flow in the

atmosphere (Keeling and Peng, 1995; Gloor et al., 2003). The primary mechanism accounting for most of the meridional and vertical transport of carbon in the oceans is the large scale overturning circulation. Regions where cold dense waters sink, particularly in the North Atlantic and Southern Ocean, are regions of high carbon uptake. Carbon is carried to depth when these water masses are convected, and the lower partial pressure in the surface waters increases the downward flux of CO_2 in these regions.

Although most of the carbon in the oceans is in the form of dissolved inorganic carbon (comprised of dissolved CO_2, CO_3^{2-} and HCO_3^- ions), biological and carbonate pumps also cycle carbon and affect the vertical gradient of DIC. Phytoplankton in the upper surface waters decrease the partial pressure of CO_2 through photosynthesis and thus increase uptake of CO_2 from the atmosphere. Dissolved organic carbon (DOC) together with particulate organic carbon (POC), resulting from detritus and dead organisms, provide a downward flux of organic matter to the deep oceans. A small amount of this ends up in sediments and most is converted to DIC through heterotrophic respiration. This biological cycling of carbon allows the maintenence of higher DIC stores in the deep ocean and atmospheric CO_2 concentrations to be about 150 to 200 ppmv lower than they would be without the biological carbon cycle operating (Farquhar et al., 2001). In addition to the organic cycling of carbon, carbonate is cycled over century time scales and affects the vertical DIC gradient. Species of phytoplankton and zooplankton form carbonate shells in the surface waters, using bicarbonate ions and producing CO_2 thereby reducing both DIC and alkalinity (in a 1:2 ratio) in the surface waters and increasing outgassing. This continuous cycling of carbon between atmosphere and ocean is a steady state system and the activities of man perturb this balance.

1.2 Anthropogenic CO_2

Prior to industrialization, around the mid-1800s, it is thought that the global carbon cycle was in a steady state. Superimposed on the global ocean carbon steady state is the excess CO_2 due to the uptake of anthropogenic CO_2 which is currently thought to be controlled by chemical and physical processes (Maier-Reimer and Hasselmann, 1987; Farquhar et al., 2001). We do not however, fully understand the biogeochemical role in maintaining the steady-state ocean carbon cycle, so it is difficult to address the related changes associated with these systems under a changing climate. Changes in the carbonate chemistry however, which affect the ocean pH, may affect marine

biology through increased calcification rates and over century time scales may increase uptake of CO_2 by the oceans slightly (Farquhar et al., 2001). François et al. (1997) suggest that surface water stratification may contribute to increased CO_2 uptake in the Southern Ocean through changes in nutrient availability. Changes in sea ice cover may also impact biological productivity due to the availability of light. It is essential to obtain improved observational support for these biological complexities, especially at high latitudes, which have been introduced into current general circulation models (GCMs) (see for e.g., Sarmiento and Le Quéré, 1996; Maier-Reimer and Hasselmann, 1987; Joos et al., 1999). A more fundamental step is to gain a thorough understanding of the inorganic carbon cycle against which future numerical experiments, including marine biology and a terrestrial carbon component, can be carried out.

Regional, annual and inter-annual uptake of CO_2 varies considerably (Gruber et al., 2002; Le Quéré et al., 2000) although it is generally assumed that on decadal or longer time scales there is much less variability (Wallace, 2001). Determination of anthropogenic CO_2 inventories from the large natural background variability of DIC has been carried out using a method developed by Gruber et al. (1996) for the Atlantic, Indian (Gruber, 1998) and Southern oceans (Sabine et al., 1999). These estimates have been found to be more consistent with three-dimensional global circulation modelling studies of anthropogenic CO_2 than with two-dimensional zonally averaged models (Wallace, 2001). Since CO_2 is more soluble in colder waters, most of the net absorption of CO_2 in the oceans occurs in the polar regions (Jones et al., 1990) and modelling studies have shown the Southern Ocean to be an important sink for anthropogenic CO_2 (Maier-Reimer and Hasselmann, 1987; Sarmiento and Le Quéré, 1996; Sarmiento et al., 2000; Orr et al., 2001). Caldeira and Duffy (2000) have also shown that the Southern Ocean is an important region for anthropogenic CO_2 uptake when compared to tracer observations (Gruber, 1998; Sabine et al., 1999) although not for long term storage of carbon.

The interaction of climate feedbacks with the carbon cycle under increasing atmospheric CO_2 is still a source of uncertainty. It is thought that the oceans have the capacity to take up 70-80% of the anthropogenic CO_2 through increased dissolution (Archer et al., 1997; Ewen et al., 2004a). The uptake is limited by the rate of ocean mixing, on the time scale of hundreds of years (Maier-Reimer, 1993), which is much longer than the annual rate of anthropogenic CO_2 increase. The use of climate models allows us to study the potential effects of climate change on the future uptake of CO_2. Certainly many studies have attempted to address the role of feedback mechanisms on future carbon uptake using various climate models (including Siegen-

thaler and Oeschger, 1978; Manabe and Stouffer, 1994; Sarmiento and Le Quéré, 1996; Sarmiento et al., 1998; Joos et al., 1999; Cox et al., 2000; Friedlingstein et al., 2001; Plattner et al., 2001). As the climate warms anthropogenic carbon will continue to be taken up, and it is generally thought that this will occur at a decreasing rate due to the climate feedbacks acting on the carbon system. The main feedbacks are thought to include reduced buffering capacity of the carbonate system, increased SSTs which reduce pCO_2 solubilities and changes in ocean circulation. Most models show a weakening in the thermohaline circulation which leads to both decreased heat transport to the North Atlantic and also to a reduction in carbon flux to this region. Northern hemisphere sea ice extent is also projected to decrease (Christy et al., 2001) which will increase air sea interaction and may increase carbon flux to the oceans although modelling studies have also shown that surface freshening may lead to increased stratification in high latitudes, thereby reducing carbon uptake (Sarmiento et al., 1998).

Although many of these modelling studies agree that the high latitude regions are important for anthropogenic carbon uptake (Orr et al., 2001) and are regions highly sensitive to climate change, few have incorporated sea ice components in their models, or have addressed these studies using thermodynamic sea ice models. It is thought that model parameterizations of both sea ice and sub-grid-scale mixing processes lead to the largest discrepancies between model CO_2 uptake in the high latitude regions (Wallace, 2001) and have also been found to affect CFC tracer distributions when compared to observations (Robitaille and Weaver, 1995; Dutay et al., 2002; Saenko et al., 2002). In Chapter 3 carbon uptake under anthropogenic forcing is addressed and the role of climate feedbacks on future uptake is examined. An investigation of model parameterizations for both sea ice and sub-grid-scale mixing is also carried out.

1.3 Abrupt climate change and CO_2

Understanding climate variability in the past is critical if we are to improve our understanding of future climate change. The mechanisms which led to abrupt climate changes in the past are still not fully understood although paleoclimate records reveal that variability in the thermohaline circulation (THC) was involved in the rapid transitions between cold and warm states. These abrupt transitions, termed Dansgaard-Oeschger (D-O) oscillations (Dansgaard et al., 1984; Oeschger et al., 1984), occurring over the last glacial period (Stocker, 2000; Clark et al., 2002b) are marked by abrupt

warming events of several degrees occurring over decades or less (Grootes et al., 1993) which are recorded in the stable oxygen isotopes (^{18}O) of the Greenland ice cores. The sequence of D-O oscillations often terminates with meltwater episodes (Bond and Lotti, 1995) as evident in layers of ice-rafted debris found in marine sediments (Heinrich, 1988).

Climate modelling simulations show that meltwater discharges reduce the overturning strength of the THC through changes in North Atlantic Deep Water (NADW) formation (Manabe and Stouffer, 1995; Clark et al., 2002b; Schmittner et al., 2002). At the centennial timescale, a reduction in the Atlantic overturning impacts the carbon balance through diminishing the transport of inorganic carbon from the surface to the deep ocean. Changes in sea ice cover, corresponding to changes in the poleward heat transport, also effect CO_2 uptake by changing air-sea interaction in the high latitude regions. Associated changes in sea surface temperatures (SSTs), salinities (SSSs) and alkalinity further affect CO_2 solubility and uptake in both hemispheres.

Antarctic ice cores further reveal that atmospheric CO_2 concentrations increased by 10-20 ppmv during strong D-O oscillations (Stauffer et al., 1998; Indermühle et al., 2000) during warm interstadial phases. Increases in atmospheric CO_2 between 20 kyr and 70 kyr BP parallel warming events in Antarctica (Indermühle et al., 2000) and seem to be connected with large iceberg discharges in the North Atlantic.

Abrupt transitions have also occurred between the LGM and the Holocene as recorded in, for example, the GISP2 (Greenland) oxygen isotope records (Grootes et al., 1993). The Oldest Dryas cold period was followed by the Bølling-Allerød warm interval, in which a warming of several degrees took place over a few hundred years, bringing an end to the last glacial period. The Bølling-Allerød interstadial event (14,600 kyr BP in the GISP2 oxygen isotope record) was a rapid warming event which corresponds to the Antarctic Cold Reversal (ACR) in the Southern Ocean and a rapid increase in atmospheric CO_2 concentrations as seen in the Dome C CO_2 data (Monnin et al., 2001). Coincident with the onset of the Bølling-Allerød was an abrupt increase in atmospheric CO_2 of about 8 ppmv in <300 years (Monnin et al., 2001). This interval is also thought to have coincided with a large meltwater pulse (mwp-1A) in the Southern Ocean (Clark et al., 2002a; Weaver et al., 2003). It is thought that the Southern Ocean played a key role in abrupt transitions of atmospheric CO_2 during the last glacial termination, however the changes in the North Atlantic THC during mwp-1A probably also played a key role during that time. In Chapter 4 the role of the carbon cycle during these abrupt transitions is examined.

1.4 Glacial-interglacial cycles and CO_2

Advances and retreats of the major ice sheets are documented in ocean sediment records which show changes in the isotopic composition of oxygen in seawater as recorded in calcium carbonate manufactured by marine organisms (Archer et al., 2000). Formation of glacial ice selectively uses the lighter oxygen isotope, ^{16}O, as this isotope is preferentially evaporated from the oceans, leaving the oceans enriched in ^{18}O. Fractionation also occurs when microfossils take up calcium carbonate, with the heavier oxygen isotope selectively used under warmer temperatures (Broecker, 1993). Oxygen isotopes are thus important paleoclimate indicators of both ice volume and past temperatures. During cooler glacial periods, increased ice volume and colder temperatures both raise the ratio of ^{18}O to ^{16}O and is recorded in the marine shells.

These cycles of glacial changes correlate with variations in the Earth's orbit which cause differences in the geographical receipt of solar insolation (Berger, 1978). Orbital cycles show spectral peaks at periods of 23 kyr, 41 kyr and 100 kyr corresponding to changes in precession, obliquity and orbital eccentricity (Crowley and North, 1991). $\delta^{18}O$ records of glacial cycles are in rough proportion to the Northern Hemisphere solar heating flux calculated from orbital theory before 800 kyr BP. After this time however, the 100 kyr glacial cycles appear stronger than what orbital theory predicts (Imbrie et al., 1992), and the global ice volume record can not be explained by orbital variations alone.

Proxy records related to atmospheric CO_2 concentration and deep ocean circulation in the Atlantic ocean lead changes in ice volume as investigated by Imbrie et al. (1992, 1993). This suggests that ocean circulation and atmospheric CO_2 may have played an important role in amplifying the glacial cycles. Indeed close correlation between Antarctic temperature and CO_2 concentration (Barnola et al., 1987; Petit et al., 1999; Monnin et al., 2001) suggests that CO_2 is an important amplifier of the initial changes in orbital forcing and indicates that the Southern Ocean played an important role in the CO_2 increase seen during the last glacial termination (Monnin et al., 2001). Atmospheric CO_2 concentrations were about 80 ppmv lower during glacial periods than during interglacial periods, as indicated by ice core measurements (Petit et al., 1999). Vostok ice core records from Antarctica reveal that atmospheric CO_2 has oscillated in 100,000 year cycles between the relatively constrained bounds of 180 to 280 ppmv over the last four deglaciations during the past 420 kyr BP (Petit et al., 1999).

The mechanisms that have led to changes in atmospheric CO_2 are still unex-

plained. $\delta^{13}C$ sediment records and modelling studies reveal that the terrestrial biosphere actually stores 300 to 700 PgC more during interglacial periods (Farquhar et al., 2001) and thus cannot be responsible for the difference in atmospheric CO_2 concentrations. A combination of mechanisms resulting from changes in the ocean carbon cycle may hold the key and many hypotheses have been investigated. It is believed that past changes in sea surface temperatures and salinities or carbonate budget cannot be responsible. Other possible explanations involve changes in the size of the nutrient pool and an increase in biological activity at high latitudes (Sarmiento and Toggweiler, 1984; Sigman and Boyle, 2000). Increased iron supply to the Southern Ocean, where iron is thought to limit production, is also implicated in the changes. An increase in Patagonian Deserts led to an increase in atmospheric dust and iron supply to the Southern Ocean. This in turn stimulated marine biota and drawdown of atmospheric CO_2 (Petit et al., 1999). Export production of organic carbon is also thought to increase, causing surface alkalinity to increase, further driving down atmospheric CO_2. Together, these effects may account for 15-40 ppmv decrease in atmospheric CO_2 (Bopp et al., 2003). None of these hypotheses, explaining glacial-interglacial atmospheric CO_2 changes however, are sufficient on their own to account for the 80 ppmv difference in CO_2 concentrations.

Recently, several studies have focused on implicating physical processes in the ocean for the 80 ppmv change in atmospheric CO_2 during the last deglaciation. In particular, changes in Southern Ocean sea ice extent, ventilations rate and stratification have all been used to explain the difference in several box model studies (Toggweiler, 1999; Stephens and Keeling, 2000; Gildor and Tziperman, 2002). In order to improve our understanding of how these processes affect CO_2 uptake in GCMs, an examination of the changes in the ocean carbon cycle and resulting atmospheric CO_2 concentrations under glacial-interglacial climate forcing is carried out in Chapter 5.

1.5 Outline

In the following chapter an overview of the coupled model used throughout this thesis is described including ocean-atmosphere and sea ice components. The inorganic carbon cycle which has been coupled to this model is then described in the final section of Chapter 2. In Chapter 3, an analysis of the sensitivity of the inorganic carbon cycle to future climate warming is carried out. The effect of climate change on future uptake of carbon by the ocean is examined as well as the role of model sea ice

and sub-grid-scale mixing parameterizations. Paleoclimate studies are then carried out in Chapters 4 and 5. Abrupt climate change in the past is studied in Chapter 4 through an analysis of the response of atmospheric CO_2 and oceanic carbon uptake to meltwater pulse perturbations in both hemispheres. In Chapter 5 the sensitivity of CO_2 uptake to glacial-interglacial forcing is examined. From an equilibrium 21 kyr BP, boundary conditions for 8 kyr BP are imposed and changes in the carbon cycle are analyzed. Finally, conclusions are given in Chapter 6.

2 Model description and set up

The coupled model used throughout this thesis is version 2.3 of the UVic ESCM described in Weaver et al. (2001). The model consists of a 3-D ocean GCM coupled to a thermodynamic/dynamic sea ice model (Bitz et al., 2001) and a dynamic energy-moisture balance atmosphere model. The ocean component of the coupled model is a fully nonlinear 3-D ocean GCM (Pacanowski, 1995) with a global resolution of a 3.6° (zonal) by 1.8° (meridional) and 19 vertical levels. A reduced complexity atmosphere model is used for computational efficiency. Atmospheric heat and moisture transport is parameterized through Fickian diffusion, with precipitation occurring when the relative humidity exceeds 85%.

2.1 Atmosphere model

The energy moisture balance model of Fanning and Weaver (1996) is used for the atmospheric component of the coupled model. It is based on earlier thermodynamic models of Sellers (1969) and North (1975) and is coupled to the oceanic component by allowing sensible, latent and radiative heat transfers between the ocean and atmosphere.

The vertically-integrated energy balance is given by

$$\rho_a h_t c_{pa} \frac{\partial T_a}{\partial t} = Q_T + Q_{SSW} + Q_{LW} + Q_{SH} + Q_{LH} - Q_{OLW} \tag{2.1}$$

where $\rho_a = 1.25\text{kg m}^{-3}$ is the constant surface density, h_t a constant scale height for temperature chosen to be 8.4 km (Gill, 1982), $c_{pa} = 1004$ J kg^{-1} K^{-1} is the specific heat of air at constant pressure and T_a is the surface air temperature. The source-sink terms on the right hand side of (2.1) are Q_T, the eddy diffusion horizontal heat transport, Q_{SSW} is the absorbed atmospheric short wave radiation, Q_{LW} is the longwave radiation at the surface, Q_{SH} and Q_{LH} are the sensible and latent heat fluxes respectively and Q_{OLW} is the outgoing longwave radiation.

The parameterization for the eddy-diffusive horizontal heat transport Q_T, is given by:

$$Q_T = \rho_a h_t c_{pa} \nabla \cdot (\nu \nabla T_a) \tag{2.2}$$

where the horizontal diffusion operator is $\nabla \cdot (\nu \nabla T_a)$ and ν is the latitude dependent

horizontal eddy diffusivity coefficient. The latitudinal profile for this coefficient can be found in Weaver et al. (2001). The shortwave radiation is given by:

$$Q_{SSW} = C_A Q_{TSW} \tag{2.3}$$

where $C_A = 0.3$. This coefficient parameterizes additional absorption by the atmosphere of incoming shortwave radiation on water vapor, dust, ozone and clouds (Ramanathan et al., 1987). Q_{TSW} is the total incoming shortwave radiation at the top of the atmosphere and is given by:

$$Q_{TSW} = \frac{S_\odot}{4} S(1 - \alpha) \tag{2.4}$$

where $S_\odot = 1368$ W m^{-2} is the solar constant, S is the annual distribution of shortwave radiation at the top of the atmosphere (based on Berger, 1978) and α is the latitudinally and monthly dependant albedo where

$$\alpha = \begin{cases} \alpha_o & \text{if ice free} \\ \alpha_o + \Delta\alpha & \text{otherwise.} \end{cases} \tag{2.5}$$

The effects of sea ice on the albedo are thus included in the model by locally changing the planetary albedo where α_o is the latitudinally dependent monthly mean planetary albedo (Graves et al., 1993), accounting for average cloudiness, and $\Delta\alpha$ is the increase in planetary albedo due to the presence of sea ice:

$$\Delta\alpha = \begin{cases} max(0, \Delta\alpha_o + 0.1 \ln h_i) & \text{if } h_i < 1m \\ \Delta\alpha_o & \text{otherwise} \end{cases} \tag{2.6}$$

where h_i is the ice thickness and $\Delta\alpha_o = 0.18$ is the ice albedo jump, which is applied to ice which is one meter or more in thickness. Over land this expression is simply:

$$\Delta\alpha = \Delta\alpha_o. \tag{2.7}$$

The net upward radiative flux at the surface is a sum of both the upward longwave flux emitted by the surface and the downward longwave flux which has been re-

emitted by the atmosphere:

$$Q_{LW} = \begin{cases} \varepsilon_s \sigma T_s^4 - \varepsilon_a \sigma T_a^4 & \text{over open ocean} \\ \varepsilon_s \sigma T_i^4 - \varepsilon_a \sigma T_a^4 & \text{over sea ice} \\ Q_{SW} & \text{over land} \end{cases} \tag{2.8}$$

where ε_s and ε_a are the emissivities of the surface (with a distinction between ocean and sea ice) and atmosphere and the Stefan-Boltzmann constant is $\sigma = 5.67 \times 10^{-8}$ W m^{-2} K^{-4}. All shortwave radiation intercepted over the land surface is assumed to return to the atmosphere via black body radiation such that:

$$Q_{SW} = (1 - C_a) Q_{TSW}. \tag{2.9}$$

The sensible heat flux over open ocean and ice covered ocean is given by the bulk formula:

$$Q_{SH} = \begin{cases} \rho_a c_H C_{pa} u (T_s - T_a) & \text{over open ocean} \\ \rho_a c_H C_{pa} u (T_i - T_a) & \text{over sea ice} \\ 0 & \text{otherwise} \end{cases} \tag{2.10}$$

where u is the surface wind speed, $c_H = 0.94 c_E$ is a dimensionless coefficient, often referred to as the Stanton number (Isemer et al., 1989), obtained through dimensional analysis. The Dalton number, c_E is also dimensionless and depends on the wind speed and air-sea temperature difference (see Fanning and Weaver, 1996). The winds are prescribed and seasonally-varying from NCEP Reanalysis wind data and are used with the dynamical feedback option (Weaver et al., 2001) turned off.

The latent heat into the atmosphere is given by

$$Q_{LH} = \rho_o (L_s P_s + L_v P_r - L_f S_m), \tag{2.11}$$

where ρ_o is a reference density of water, L_s, L_v and L_f are the latent heats of sublimation, vaporization and fusion respectively. P_s is the snowfall, P_r is the rainfall and S_m is the water equivalent surface melting of snow over land.

The planetary outgoing longwave radiation is based on Thompson and Warren (1982) and is given by:

$$Q_{OLW} = a_0 + a_1 T_a + a_2 T_a^2 + a_3 T_a^3 - \Delta F \tag{2.12}$$

where

$$a_m = c_{m0} + c_{m1}r + c_{m2}r^2 \quad \text{for m} = 0,1,2,3 \tag{2.13}$$

and the empirically derived constants are given by Thompson and Warren (1982). T_a is the sea level air temperature, r is the relative humidity and ΔF is the parameterization for radiative forcing associated with changes in atmospheric CO_2 concentrations and is given by:

$$\Delta F = \frac{\Delta F_{2\times}}{\ln 2} \ln \frac{C(t)}{C_0} \tag{2.14}$$

where $C(t)$ is the atmospheric CO_2 concentration, $C_0 = 350$ ppmv is a reference concentration, and $\Delta F_{2\times} = 4.0$ W m^{-2} is the radiative forcing at a doubling of atmospheric CO_2 (Ramanathan et al., 1987).

The hydrological cycle is parameterized using the balance equation for water vapor in the atmosphere, replacing the horizontal advection by an eddy diffusive term. The vertically integrated moisture balance equation is given by:

$$\rho_a h_q \left\{ \frac{\partial q_a}{\partial t} - \nabla \cdot (k_a \nabla q_a) \right\} = \rho_o (E + S - P) \tag{2.15}$$

where $h_q = 1.8$ km is a constant scale height for specific humidity given by Peixoto and Oort (1992), q_a is the surface specific humidity, k_a is the eddy diffusivity term, P is the precipitation, E is the evaporation and S is the sublimation (where E, P, S are calculated in m s^{-1}). Over open ocean, evaporation is calculated from the bulk formula:

$$E = \frac{\rho_a c_E u}{\rho_o} (q_s(T_s) - q_a) \tag{2.16}$$

where c_E is the time-dependent Dalton number from Fanning and Weaver (1996), $q_s(T_s)$ is the saturation specific humidity at temperature T_s calculated from the Clausius-Clapeyron equation from Bolton (1980), which distinguishes between ice and open ocean.

Sublimation is calculated similarly where T_s is taken as the surface temperature of the ice, and whenever $q_s(T_s) > q_a$ there is resulting evaporation or sublimation depending on whether over sea ice or open ocean.

Precipitation occurs whenever the relative humidity exceeds 85% and is parameterized by:

$$P = \begin{cases} \frac{\rho_a h_q}{\rho_o \Delta t} (q_a - r_{max} q_s(T_s)) & \text{if r} > \text{r}_{max} \\ 0 & \text{otherwise} \end{cases} \tag{2.17}$$

where $q_s(T_a)$ is the saturation specific humidity at T_a and Δt is the model time step.

Over land, Eq. 2.1 is reduced to:

$$\rho_a h_t C_{pa} \frac{\partial T_a}{\partial t} = Q_T + Q_{SW} + Q_{LH} - Q_{OLW}. \tag{2.18}$$

Note that $Q_{SH} > 0$ over open ocean and sea ice only so that over land is zero. From Eq. 2.1, $Q_{LW} = Q_{SW}$ which assumes that all shortwave radiation hitting land is returned to the atmosphere via blackbody radiation as given in Eq. 2.9. There is no moisture stored on land and $E = 0$. Precipitation instantaneously returns to the ocean via one of 33 river basins unless it falls as snow, in which case it is locally retained until such time as it melts. More realistic river basins are possible with the inclusion of orography in the model (see Weaver et al., 2001).

An annual cycle of solar insolation for both past and present orbital configurations is used (Berger, 1978) and has been successfully employed for both present day and paleoclimate simulations (Weaver et al., 1998, 2000). Insolation that reaches the Earth is determined by the solar constant S_0, the semi-major axis of the orbit, the eccentricity or the orbit, the obliquity of the ecliptic and the longitude of perihelion relative to the moving vernal equinox (Berger, 1978). Changes in insolation are calculated using a simple algorithm given by Berger (1978).

2.2 Ocean model

The ocean component of the coupled model is the Geophysical Fluid Dynamics Laboratory (GFDL) Modular Ocean Model (MOM) version 2 (Pacanowski, 1995). This model is a finite difference version of the primitive ocean equations. These equations consist of the Navier-Stokes equations subject to the Boussinesq and hydrostatic approximations. Potential temperature and salinity are the two prognostic tracers that actively affect the dynamics. The main passive tracer that is included is dissolved inorganic carbon (DIC).

The Boussinesq approximation consists of replacing $\rho_o(z)$ by its vertically averaged value ρ_o, a representative density for sea water, except in the buoyancy term. This is reasonable since the mean ocean density profile, $\rho_o(z)$, typically varies no more than 2% from its depth averaged value $\rho_o = 1.035$ g cm^{-3} (Gill, 1982). The hydrostatic approximation is imposed which implies that vertical pressure gradients are due only to density. This is justified in the ocean where the horizontal scales are much larger than vertical scales (Gill, 1982) and kinetic energy is largely dominated by horizontal motions. Sub-grid scale processes are parameterized with the assump-

tion that eddy mixing coefficients which account for sub-grid scale motion are many orders of magnitude larger than molecular values (Bryan, 1984). For computational efficiency, external gravity waves are filtered out and the rigid lid approximation is made.

The horizontal equations of motion are given by:

$$\frac{\partial u}{\partial t} = -\left(\frac{1}{\rho_o}\nabla p - fu + L(u)\right) + \nabla \cdot (A_h \nabla u) + \frac{\partial}{\partial z}\left(A_v \frac{\partial u}{\partial z}\right) \tag{2.19}$$

$$\frac{\partial v}{\partial t} = -\left(\frac{1}{\rho_o}\nabla p + fv + L(v)\right) + \nabla \cdot (A_h \nabla v) + \frac{\partial}{\partial z}\left(A_v \frac{\partial v}{\partial z}\right) \tag{2.20}$$

where

$$L(\zeta) = w\frac{\partial}{\partial z}\zeta + (\mathbf{u}_h \nabla \zeta) \tag{2.21}$$

is the advective operator for the nonlinear terms in the total derivative, f is the Coriolis parameter and $\mathbf{u}_h = u, v$ is the horizontal velocity. Terms involving the eddy viscosity coefficients, $A_h = (A_x, A_y)$ and A_v, arise from parameterizing the Reynolds stresses which result from considering the time average of the equations of motion. The vertical friction term, $\frac{\partial}{\partial z}\left(A_v \frac{\partial u}{\partial z}\right)$ is the parameterization for the vertical exchange of momentum due to sub-grid scale mixing processes. Similarly, $\nabla \cdot (A_h \nabla v)$ parameterizes the horizontal exchange of momentum, where ∇ is the horizontal gradient operator. We use $A_v = 1 \times 10^{-3}$ m^2 s^{-1} and $A_h = 2 \times 10^5$ m^2 s^{-1} for the vertical and horizontal eddy viscosities respectively.

In the vertical direction the equation of motion is reduced to:

$$\frac{\partial p}{\partial z} = -g\rho \tag{2.22}$$

due to the hydrostatic approximation which implies that pressure in a static fluid decreases with height and these gradients are due only to density. The vertical coordinate, z, is positive upwards and the gravitational acceleration is $g = 9.81$ m s^{-2}.

The ocean model is initially at rest as the initial velocity field is assumed to vanish (i.e., $u = v = w = 0$). An idealized temperature and salinity distribution is constructed based on zonal averages of annual means from the Levitus (1982) data and an idealized density distribution is constructed. The distribution is only a function of latitude and depth and is contained within the MOM ocean model so no

data sets are used. The surface and bottom boundary conditions are

$$w = 0 \quad \text{at} \quad z = 0, -H \tag{2.23}$$

where:

$$\rho_o A_v \frac{\partial \mathbf{u}_h}{\partial z} = \boldsymbol{\tau}_z \tag{2.24}$$

and the horizontal stress vector at the surface and bottom ($z = 0, -H$) is given by:

$$\boldsymbol{\tau}_z = (\tau_z^\lambda, \tau_z^\phi) \tag{2.25}$$

where λ and ϕ represent longitude and latitude respectively. The surface stress is taken from reanalysis data (Kalnay et al., 1996) and the bottom stress ($z = -H$) is calculated from the bulk formula:

$$\boldsymbol{\tau}_{-H} = \rho_o c_{DB} \mid \mathbf{u}_h^{-H} \mid \mathbf{u}_h^{-H} \tag{2.26}$$

where the dimensionless bottom drag coefficient is given by $c_{DB} = 1.3 \times 10^{-3}$ and $\mathbf{u}_h^{-H}$ is the velocity at the first depth level from the bottom. Dirichlet conditions are assumed at the lateral boundaries where the velocity vector goes to zero (no-slip). Cyclic boundary conditions are applied in the longitude giving a semi-infinite domain. Flow out of the eastern end of the basin enters the western and vice versa.

The conservation equations for the two active tracers, potential temperature and salinity, are given by:

$$\frac{\partial T}{\partial t} + L(T) = \nabla_h \cdot (k_h \nabla T) + \frac{\partial}{\partial z}\left(k_v \frac{\partial T}{\partial z}\right), \tag{2.27}$$

$$\frac{\partial S}{\partial t} + L(S) = \nabla_h \cdot (k_h \nabla S) + \frac{\partial}{\partial z}\left(k_v \frac{\partial S}{\partial z}\right) \tag{2.28}$$

where the horizontal eddy diffusivity is given by $k_h = 2{\times}10^3$ m^2 s^{-1} and the vertical eddy diffusivity varies with depth from $k_v = 0.6{\times}\ 10^{-4}$ m^2 s^{-1} in the thermocline to $k_v = 1.6{\times}10^{-4}$ m^2 s^{-1} in the deep ocean. These eddy diffusivities result from the parameterization of sub-grid scale mixing of tracers. The vertical eddy diffusivity is modified from Bryan and Lewis (1979) and given by:

$$k_v = 1 \times 10^{-4}\left(0.8 + \frac{1.05}{\pi}\arctan[4.5 \times 10^{-5}(z - 2.5 \times 10^5)]\right). \tag{2.29}$$

This diffusivity profile is weak in the thermocline and increases with depth. It is physically motivated by recent observations which show enhanced mixing in the deep ocean and, more importantly, for its ability to improve water mass distributions in this ocean model (Simmons et al., 2004).

The equation of state for seawater is a nonlinear function of potential temperature, salinity and pressure and is given by:

$$\rho = \rho(T_\theta, S, p). \tag{2.30}$$

The boundary conditions for potential temperature and salinity at the surface ($z = 0$) are:

$$Q_T = \rho_o c_{po} k_v \frac{\partial T}{\partial z} \tag{2.31}$$

and

$$F_S = \rho_o k_v \frac{\partial S}{\partial z}. \tag{2.32}$$

The heat flux is given by:

$$Q_T = \begin{cases} Q_{SW} - Q_{SH} - Q_{LW} - Q_{LH}^E & \text{if ice free} \\ Q_b & \text{otherwise} \end{cases} \tag{2.33}$$

where latent heat flux due to evaporation is given by:

$$Q_{LH}^E = \rho_o L_v E \tag{2.34}$$

and Q_b is the heat flux from ocean to sea ice. The freshwater flux is given by:

$$F_S = \begin{cases} S_o(E - P - R) & \text{if ice free} \\ (S_o - S_i)F - S_o(P + R) & \text{otherwise} \end{cases} \tag{2.35}$$

where the specific heat of seawater at constant pressure is given by $c_{po} = 4044$ J kg^{-1} K^{-1}, S_o and S_i are representative salinities for the ocean and ice respectively, R is the freshwater input from the rivers and F is the freshwater flux due to sea ice formation and melting where:

$$F = \frac{\rho_i}{\rho_o} \frac{\partial H_i}{\partial t} \tag{2.36}$$

and the density of the sea ice is given by ρ_i and the thickness by H_i.

Neumann conditions are assumed for heat and salt on the bottom and lateral

boundaries (no-flux across boundaries) where:

$$\frac{\partial T}{\partial n} = \frac{\partial S}{\partial n} = 0 \tag{2.37}$$

and n is the unit vector normal to the boundary surface.

2.2.1 Mixing parameterizations

Gent McWilliams sub-grid scale parameterization for ocean mixing and isopycnal mixing are used together in all experiments where we have stated that GM is used. When GM is not used, we have used standard horizonal/vertical mixing. Mixing in the real ocean is predominantly along isopycnal surfaces so the standard horizontal/vertical mixing scheme is somewhat unrealistic, especially in regions where there are steeply sloping isopycnals as the diapycnal diffusion becomes unrealistically large. Isopycnal mixing, which was introduced by Redi (1982) and implemented in the GFDL model by Cox (1987), is not entirely along isopycnals as some lateral mixing is required in order to maintain computational stability. In addition to the isopycnal mixing, Gent and McWilliams (1990) introduced a parameterization to represent the effects of mesoscale eddies which are too small to be resolved in general circulation models. It attempts to account for the effects of baroclinic instability by removing potential energy from large scale features. The transport of these effects are adiabatic (no mixing across density surfaces) and the volume of water between density surfaces is unchanged. This parameterization has been shown to improve certain aspects of GCM climatology, in particular to improve temperatures at intermediate depths through a sharper thermocline and the deep oceans have more realistic colder and saltier waters (Danabasoglu et al., 1994; Duffy et al., 1995). The inclusion of the GM mixing scheme has also been shown to improve CFC tracer distributions in an earlier version of our model Robitaille and Weaver (1995) and reduce unrealistic convective plumes in the Southern Ocean.

The GM parameterization for mesoscale eddy mixing uses a down gradient isopycnal thickness diffusion - which determines the strength of the eddy-induced transport - while tracer diffusion occurs along isopycnals. This results in an additional transport velocity in the tracer equations where:

$$\frac{\partial T}{\partial t} + L'(T) = R(k_i, T) + \frac{\partial}{\partial z}\left(k_v \frac{\partial T}{\partial z}\right), \tag{2.38}$$

and

$$\frac{\partial S}{\partial t} + L'(S) = R(k_i, S) + \frac{\partial}{\partial z}\left(k_v \frac{\partial S}{\partial z}\right), \tag{2.39}$$

where the modified advection operator is given by:

$$L'(\zeta) = (w + w^*)\frac{\partial}{\partial z}\zeta + (\mathbf{u}_h + \mathbf{u}^*)_h \nabla\zeta. \tag{2.40}$$

In Eqns. 2.38 and 2.39, R is the diffusion along isopycnals with an isopycnal diffusion coefficient of k_i. The advection is a sum of the effective transport velocity $(\mathbf{u}, w)$ and the eddy-induced transport velocity $(\mathbf{u}^*, w^*)$. This eddy induced transport velocity is given by:

$$\mathbf{u}^* = (k_i \nabla\rho/\rho_z)_z, \quad w^* = -\nabla \cdot (k_i \nabla\rho/\rho_z) \tag{2.41}$$

where ρ is the potential density.

2.3 Sea ice model

The basic sea ice equations are described in this section. Firstly a simple "0-layer" thermodynamic scheme (sea ice or open water) based on Semtner (1976) is described along with a two-level sea ice thickness distribution (Hibler, 1979). This is followed by a description of the elastic viscous plastic model for dynamics based on Hunke and Dukowicz (1997). More detailed thermodynamic components have also been developed including a multi-layer thermodynamic model (Bitz and Lipscomb, 1999) and thickness distribution (Holland et al., 2001; Bitz et al., 2001); see Weaver et al. (2001) for a discussion of these.

2.3.1 Sea ice thermodynamics

The thermodynamic model predicts the ice thickness (H_i), the areal fraction of ice (A_i - often referred to as compactness) and the surface temperature of the ice (T_i). Two idealized thicknesses within the grid cell are used: thick and thin. This model assumes that the surface temperature is instantaneously in equilibrium with external forcing so the ice does not have any heat capacity.

The change in ice thickness over a grid cell is given by:

$$\frac{\partial H_i}{\partial t} + L(H_i) = S_h \tag{2.42}$$

where S_h, the total ice growth, is given by:

$$S_h = f_i \left(\frac{H_i}{A} \right) A + f_i(0)(1 - A) \tag{2.43}$$

and $f_i(H_i)$ is the thermodynamically determined growth rate of ice with thickness H_i. The growth rate of ice is calculated from:

$$f_i(0) = \left\{ \begin{array}{ll} \frac{(Q_b - Q_t)}{\rho_i L_f} & \text{if } Q_b > Q_t \\ 0 & \text{otherwise} \end{array} \right\}, \tag{2.44}$$

where Q_b is the ocean heat flux and Q_t is the total heat flux from the atmosphere (with heat flux positive downward). The representative density of ice is given by $\rho_i = 913$ kg m^{-3} and the latent heat of fusion of ice is given by $L_f = 3.34\times\ 10^5$ J kg^{-1}.

The total heat flux from the atmosphere is calculated based on the fractional cover of sea ice within each grid cell where:

$$Q_t = (1 - A_i)Q_{to} + A_i Q_{ti} \tag{2.45}$$

where A_i is the areal fraction of ice. The heat flux over the ocean is given by:

$$Q_{to} = Q_{SW} - Q_{LW} - Q_{SH} - Q_{LH}^E. \tag{2.46}$$

Similarly the heat flux over sea ice is given by:

$$Q_{ti} = Q_{SW} - Q_{LW} - Q_{SH} - Q_{LH}^S, \tag{2.47}$$

where each term depends on whether there is open water or ice cover as described in Section 2.1. The latent heat flux associated with sublimation is given by:

$$Q_{LH}^S = \rho_o L_f S_m. \tag{2.48}$$

The heat flux from the ocean under freezing conditions is based on McPhee (1992) and given by:

$$Q_b = c_h u_\tau \rho_o C_{po}(T_f - T_s), \tag{2.49}$$

where $c_h = 0.0058$ is an empirical constant, the skin friction velocity is given by $u_\tau = 0.02$ m s^{-1}, T_f is the freezing temperature of water, the specific heat of water

under ice at constant pressure is given by $C_{po} = 4044$ J kg^{-1} K^{-1}.

The ice surface temperature T_i used for evaluating the individual heat fluxes in Eq. 2.45 is calculated by equating the conductive heat flux through the ice with the energy flux at the surface such that $Q_i = Q_t$ where the conductive heat flux through the ice layer is given by:

$$Q_i = \left(\frac{k_i k_s}{H_i k_s + H_s k_i} \right) (T_o - T_i) \tag{2.50}$$

This also accounts for any snow layer that may be covering the ice. In Eq. 2.50, $k_i = 2.166$ W m^{-2} K^{-1} is the thermal conductivity of ice, $k_s = 0.3$ W m^{-2} K^{-1} is the thermal conductivity of snow, and H_i and H_s are the thickness of ice and snow respectively. Whenever $T_i > T_f$ the surface temperature is reduced to the freezing point. Once Q_t is reevaluated with the new surface temperature T_i the growth rate of the ice is calculated from:

$$f_i(H_i) = \max \left[\frac{(Q_b - Q_t)}{\rho_i L_f} - S, -H_i / A \Delta t \right]. \tag{2.51}$$

The changes in compactness (or fractional area covered by ice) is given by:

$$\frac{\partial A_i}{\partial t} + L(A_i) = S_A^{in} + S_A^{out} \tag{2.52}$$

where the source term is given by:

$$S_A^{in} = \begin{cases} (f_i(0)/H_0)(1 - A_i) & \text{if } f_i(0) > 0 \\ 0 & \text{otherwise} \end{cases} \tag{2.53}$$

such that under freezing conditions, the fraction of open water $(1 - A_i)$ decays exponentially with an e-folding time of $(H_0/f_i(0))$. $H_0 = 0.01$ m represents a demarcation thickness between thick ice and thin ice such that the thickness of thin ice is set to zero under the assumption that open water and thin ice up to the thickness H_0 approximately represent thin ice cover in a grid cell.

The sink term which represents melting is given by:

$$S_A^{out} = \begin{cases} (A/2H_i)S_h & \text{if } S_h < 0 \\ 0 & \text{otherwise.} \end{cases} \tag{2.54}$$

2.3.2 Sea ice dynamics

The vertically integrated momentum balance for sea ice is given by:

$$m\frac{\partial \mathbf{u}}{\partial t} = \nabla \cdot \boldsymbol{\sigma} - mf\mathbf{k} \times \mathbf{u} + \boldsymbol{\tau}_a + \boldsymbol{\tau}_w - mg\nabla h \tag{2.55}$$

where m is the ice mass per unit area, $\mathbf{u} = (u, v)$ is the horizontal ice velocity, $\mathbf{k}$ is the vertical unit normal vector, $\boldsymbol{\sigma}$ is the internal stress tensor,$\boldsymbol{\tau}_a$ and $\boldsymbol{\tau}_w$ are the atmospheric and oceanic stresses and h is the sea surface height.

The strain rate tensor is given by:

$$\dot{\epsilon} = \frac{1}{2}\left(\frac{\partial v_i}{\partial x_j} + \frac{\partial v_j}{\partial x_i}\right) \tag{2.56}$$

The strain rate tensor and internal stress tensor are related through the following equation:

$$\frac{1}{E}\frac{\partial \sigma_{ij}}{\partial t} + \frac{1}{2\eta}\sigma_{ij} + \frac{\eta - \zeta}{4\eta\zeta}\sigma_{kk}\delta_{ij} + \frac{P}{4\zeta}\delta_{ij} = \dot{\epsilon} \tag{2.57}$$

The water stress exerted by the ocean is given by:

$$\boldsymbol{\tau}_w = c'_w[(\mathbf{U}_w - \mathbf{u})\ cos\ \varphi_w + \mathbf{k} \times (\mathbf{U}_w - \mathbf{u})\ sin\ \varphi_w] \tag{2.58}$$

and the stress imposed by the atmosphere is:

$$\boldsymbol{\tau}_a = c'_a[\mathbf{U}_g\ cos\ \varphi_a + \mathbf{k} \times \mathbf{U}_g\ sin\ \varphi_a] \tag{2.59}$$

where $\mathbf{U}_w$ and $\mathbf{U}_g$ are the geostrophic ocean current and geostrophic wind, c'_w and c'_g are the air and water drag coefficients and φ_a and φ_w are the turning angles for air and water which is set to 25°. The currents are estimated by $\mathbf{U}_w = \frac{g}{f}\mathbf{k} \times \nabla h$ with h set to the dynamic height. The drag coefficients are expressed by:

$$c'_w = \rho_o c_w |\mathbf{U_w} - \mathbf{u}| \tag{2.60}$$

and

$$c'_a = \rho_a c_a |\mathbf{U_g}| \tag{2.61}$$

where the dimensionless drag coefficients for air and water are $c_a = 0.0012$ and $c_w = 0.0055$ respectively. This term is assumed to include frictional drag due to the relative movement between the ice and ocean surface layer.

2.4 The Inorganic Carbon Model

The inorganic carbon component is based on the Ocean Carbon Model Intercomparison Project (OCMIP) implementation (Orr et al., 1999). The inorganic ocean carbon cycle interacts with the atmosphere through the air-sea fluxes. The total flux from the ocean to atmosphere is calculated at each time step and integrated to give a new atmospheric CO_2 concentration. We assume that the atmosphere is well mixed. The new atmospheric CO_2 concentration is also used in the parametrization for the radiative forcing, so that climate change feedbacks are included. In our carbon model, dissolved inorganic carbon (DIC) is modeled as a passive tracer and is carried in the model with the following conservation equation:

$$\frac{\partial DIC}{\partial t} + L(DIC) = \nabla_h \cdot (k_h \nabla_h DIC) + \frac{\partial}{\partial z}\left(k_v \frac{\partial DIC}{\partial z}\right) + J + J_v \tag{2.62}$$

where the source-sink term J represents that due to air-sea exchange of CO_2 and the virtual source-sink term J_v represents the changes in DIC due to evaporation, precipitation and runoff. Both source-sink terms are divided by the model surface layer thickness to get equivalent fluxes.

In order to calculate the flux of CO_2 across the air-sea interface we determine the CO_2 gas content in surface waters where:

$$CO^*_{2(aq)} = CO_{2(aq)} + H_2CO_{3(aq)}. \tag{2.63}$$

A hypothetical species $CO^*_{2(aq)}$ is used as $CO_{2(aq)}$ and $H_2CO_{3(aq)}$ are difficult to determine analytically.

The total dissolved inorganic carbon (DIC) concentration in a sample of sea water is given by:

$$[DIC] = [CO^*_2] + [HCO^-_3] + [CO^{2-}_3], \tag{2.64}$$

where less than 1% is in the form of CO_2 gas.

Throughout the ocean, the following reaction takes place:

$$H_2O + CO_2 + CO^{2-}_3 \rightleftharpoons 2HCO^-_3. \tag{2.65}$$

This reaction proceeds rapidly and chemical equilibrium is maintained. In the solubility model, CO^{2-}_3 and HCO^-_3 concentrations are fixed by the alkalinity and DIC content, although these concentrations would change due to biological and carbonate

pumps if included.

The gas exchange flux across the air to sea interface is given by

$$F = k_w(CO_{2(atm)} - CO^{\star}_{2(surf)}) \tag{2.66}$$

where

$$CO_{2(surf)} = \alpha \cdot pCO_{2_{atm}} \cdot P. \tag{2.67}$$

Here α is the CO_2 solubility for water-vapor saturated air given through Henry's Law which depends on the model sea surface temperature (SST). The partial pressure of CO_2 in dry air at one atmosphere total pressure is given by $pCO_{2_{atm}}$ and P is the total air pressure at sea level.

The surface concentration $CO^{\star}_{2(surf)}$ depends upon four model prognostic variables; SST denoted as T, sea surface salinity (SSS) denoted as S, the model surface alkalinity (Alk) and DIC concentrations such that:

$$CO^{\star}_{2(surf)} = f(T, S, Alk, DIC) \tag{2.68}$$

Eq. 2.68 also requires the determination of several dissociation constants which depend on T and S for the equilibrium reactions (see Dickson and Goyet, 1994, for the analysis of CO_2 parameters in sea water).

The CO_2 transfer velocity k_w is given by

$$k_w = (1 - \gamma_{ice})\ 0.337 u^2_{av} \left(\frac{Sc}{660}\right)^{0.5} \tag{2.69}$$

which is modified from Wanninkhof (1992) and depends on γ_{ice}, the fractional sea ice cover which varies between 0.0 to 1.0, and u_{av}, the wind speed. The constant 0.337 is adjusted to give the correct global mean gas transfer velocity as deduced from the distribution of natural and bomb radiocarbon and an idealized wind speed distribution (Broecker et al., 1986). The Schmidt number, Sc, is computed using model SST and constants based on Wanninkhof (1992):

$$Sc = a - bT + cT^2 - dT^3. \tag{2.70}$$

3 Sensitivity of the inorganic ocean carbon cycle to future climate warming in a coupled climate model

3.1 Introduction

Since preindustrial times, the atmospheric concentration of CO_2 has increased from about 280 ppmv to today's concentrations of about 370 ppmv. It is now well known that the oceans can act as an important sink for excess anthropogenic CO_2 and that the amount of dissolved inorganic carbon (DIC) in the oceans is about 50 times greater than that of the atmosphere. Most of the net absorption of CO_2 occurs in polar regions (Jones et al., 1990) and, in particular, the Southern Ocean (Sarmiento and Le Quéré, 1996; Orr et al., 2001). In fact, Archer et al. (1997) have suggested that on the timescale of several hundred years, the oceans will sequester 70-80% of the CO_2 released into the atmosphere through the solubility pump alone, with further reductions of less than 10% through millennial time scale reactions with $CaCO_3$.

Although the oceans can potentially absorb most of the excess anthropogenic CO_2 over hundreds of years, transport of carbon between the surface and deep ocean is slow compared to the rate of increase in the atmosphere. In addition, the interaction of climatic feedbacks with the carbon cycle are still a source of uncertainty. Although uptake of CO_2 generally increases with increasing atmospheric CO_2 concentrations, it is thought to be reduced through a series of climate feedback mechanisms stemming from increased radiative forcing. These feedbacks include: increasing sea surface temperatures (SSTs), that induce modifications to CO_2 solubility; changes to the hydrological cycle that may lead to changes in stratification and deep water formation and changes in ocean circulation. As atmospheric CO_2 increases and is dissolved into ocean surface waters, the ability for the ocean to take up more carbon is reduced. When CO_2 dissolves in sea water, carbonate is used to produce bicarbonate by the forward reaction in Eq.2.64. This reduces the total amount of carbonate that is available to further react with dissolved CO_2, pushing the partial pressure higher and reducing uptake. Possible reductions in sea ice extent in the high latitude regions resulting from increased radiative forcing may also effect ocean carbon uptake. Increased air-sea interaction due to loss of sea ice in these regions will potentially allow

more CO_2 to be taken up and could help to counteract reduced uptake of carbon by other mechanism including changes in SSTs and ocean circulation.

Using a low-order physical-biogeochemical model, Joos et al. (1999) found that the most dominant feedback in the reduction of oceanic carbon uptake was sea surface warming, except in cases where North Atlantic Deep Water (NADW) formation ceased. The formation of deep water transports carbon to depth, allowing surface waters to take up more atmospheric CO_2. If NADW formation is reduced or ceases, this mechanisms of carbon transport is also reduced. Changes to the marine carbon cycle were also found to have a small effect on atmospheric CO_2 concentrations. A weakening of the THC was found to be the dominant effect contributing to the reduction in CO_2 uptake in Sarmiento and Le Quéré (1996), followed by changes in solubility associated with increases in SSTs. Comparing a control run - in which there was no increase in atmospheric CO_2 - to global warming scenarios, they found a reduction in ocean carbon uptake of 38-49% could be attributed to SST and circulation feedbacks. Sarmiento et al. (1998) found that increased SSTs in low latitudes and surface freshening at high latitudes lead to increased stratification. This is particularly important in the Southern Ocean where increased stratification leads to reduced uptake through a decrease in convective overturning and mixing along isopycnals. Carbon is taken up in the Southern Ocean where isopycnals outcrop at the surface. Increased stratification leads to reduces carbon uptake as isopycnal surfaces will no longer outcrop at the surface. Comparing simulations with and without global warming feedbacks - in which atmospheric CO_2 increases in both - Plattner et al. (2001) found that global warming feedbacks reduce uptake by nearly 8%, between 41 and 48 Pg C depending on the stabilization scenario, when forcing is carried out to year 2100. Other studies, including Friedlingstein et al. (2001); Cox et al. (2000), find a decrease in uptake of 10-20% due to global warming feedbacks.

Through the addition of an inorganic ocean carbon cycle model into the UVic Earth System Climate Model (ESCM, Weaver et al., 2001) we systematically examine the role of climate feedbacks on the ability of the ocean to uptake excess anthropogenic CO2. In particular, we examine the effect of the representation of sub-grid-scale ocean mixing and sea ice processes, as well as the equilibrium uptake response with and without the effects of climate feedbacks acting on the system. While Matear and Hirst (1999) have examined the role of sub-grid-scale ocean mixing on carbon uptake using the CSIRO coupled model, and others have examined the uptake question in general, using a variety of other models under different scenarios of future atmospheric CO_2 emissions, our examination of sea ice processes

and our systematic transient and equilibrium response sensitivity analysis represent a novel contribution to the field. As noted in Farquhar et al. (2001) "current thinking maintains that the oceanic uptake of anthropogenic CO_2 is primarily a physically and chemically controlled process superimposed on a biologically driven carbon cycle that is close to steady state". Although changes in biological activity have been shown to induce regional changes in uptake under global warming scenarios (Sarmiento and Le Quéré, 1996; Sarmiento et al., 1998; Plattner et al., 2001), the role of biological feedbacks is still poorly understood. We thus focus exclusively on the carbon solubility pump in our analysis.

The outline of the rest of this chapter is as follows: in the next section we provide a brief overview of the UVic ESCM. In section 3.3.1 we present results from our preindustrial equilibrium. This equilibrium is then used as the initial state for a number of transient anthropogenic greenhouse gas perturbation experiments. First atmospheric CO_2 concentrations are increased from preindustrial to present-day levels and then compare our present-day climatology with that obtained from other models. In order to assess how much carbon the ocean can potentially take up after atmospheric CO_2 forcing is stopped, four separate transient experiments are carried out wherein atmospheric CO_2 is increased to four separate projected concentrations and then the forcing is removed (section 3.3.2). The sensitivity of the carbon system to climate feedbacks is then addressed. Following the experiments in section 3.3.2, a comparison is made in which atmospheric CO_2 concentration is similarly forced but the climate is held constant - the response of the ocean to uptake carbon is then examined. In section 3.3.2 the dependence of our results on the representation of sea ice and ocean mixing processes is analyzes. The results are summarized in section 3.4.

3.2 Model description and initialization

All experiments were conducted with version 2.3 of the UVic ESCM detailed in Weaver et al. (2001) and outlined in Chapter 2. The model consists of a 3-D ocean GCM coupled to a thermodynamic/dynamic sea ice model (Bitz et al., 2001) and a dynamic energy-moisture balance atmosphere model. The ocean component of the coupled model is a fully nonlinear 3-D ocean GCM (Pacanowski, 1995) with a global resolution of a 3.6° (zonal) by 1.8° (meridional) and 17 vertical levels. It includes a parameterization for brine rejection associated with sea ice growth (Duffy et al., 2001; Weaver et al., 2001). A reduced complexity atmosphere model is used for computational efficiency. Atmospheric heat and moisture transport is parameterized

through Fickian diffusion, with precipitation occurring when the relative humidity exceeds 85%. Precipitation instantaneously returns to the ocean via one of 33 river basins unless it falls as snow, in which case it is locally retained until such time as it melts. The atmospheric model includes a parameterization of water vapor/planetary longwave feedbacks, although the radiative forcing associated with changes in atmospheric CO_2 is externally imposed as a reduction of the planetary long wave radiative flux. In this application of the model, prescribed, seasonally-varying, NCEP Reanalysis winds are used with the dynamical feedback option (Weaver et al., 2001) turned off.

The coupled model has been extensively and successfully evaluated against both contemporary climate observations (Weaver et al., 2001) as well as paleo proxy records (Weaver et al., 1998; Schmittner et al., 2002; Schmittner, 2003). One of the virtues of the coupled model is that we do not need to employ explicit flux adjustments of heat and freshwater to keep the simulation of the present climate stable. It also allows us to conduct many long timescale integrations, in order to investigate climate processes through a wide range of parameter space.

The inorganic carbon component is based on OCMIP implementation (Orr et al., 1999) and is described in detail elsewhere (Ewen et al. (2004a), or Chapter 2). Changes in atmospheric CO_2 are carried out through the parameterization for longwave radiation. The radiative forcing in the atmosphere associated with changes in CO_2 is externally imposed as a reduction of the planetary longwave radiative flux, and is adapted from Ramanathan et al. (1987):

$$\Delta F(t) = \Delta F_{2x} ln(\frac{C(t)}{C_0}) \tag{3.1}$$

where $C_0 = 350$ ppmv, $C(t)$ is the atmospheric CO_2 concentration as a function of time and $\Delta F_{2x} = 5.77$ W m^{-2}, which gives a radiative forcing of 4 W m^{-2} for a doubling of CO_2.

3.3 Model results

3.3.1 Preindustrial carbon fluxes

To obtain the preindustrial equilibrium, the UVic model was initially spun up with a fixed level of atmospheric CO_2 set at 280 ppmv. Once equilibrium was reached, the atmospheric CO_2 concentration was allowed to freely evolve through local air-sea CO_2 gas exchange. The model was then integrated for a further 2800 years by which

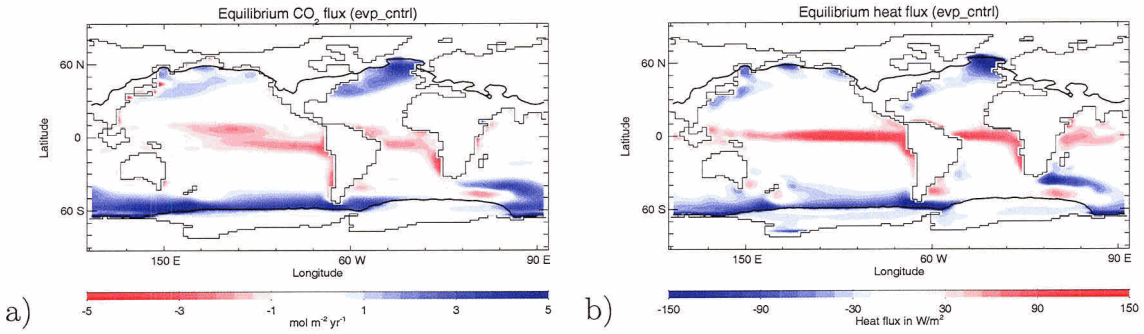

Figure 3.1: Equilibrium CO_2 flux (a) and heat flux (b) in 1850. The general patterns are the same; large negative heat fluxes correspond to high carbon uptake and vice versa.

time the globally-integrated air-sea carbon flux was less than 10^{-5} Pg C yr^{-1}, and the atmospheric CO_2 concentration varied less than 10^{-1} ppmv per 1000 yrs from its equilibrium value of 280, which indicates the equilibrium is stable.

High preindustrial carbon uptake occurs predominantly in surface waters with high solubilities. In particular, the largest CO_2 fluxes ($>$ 4 mol m^{-2} yr^{-1}) occur where there are large fluxes of heat out of the ocean or where convection occurs (Fig. 3.1a). The strongest uptake is in the Antarctic Circumpolar Current and in the ice-free region of the North Atlantic where surface waters high in CO_2 are transported to the deep ocean. About 14 Sv of NADW formation occurs in the preindustrial equilibrium, which is $\sim$4 Sv less than in Weaver et al. (2001), due to our use of the Gent and McWilliams (1990) (hereafter GM) parameterization of mixing associated with mesoscale eddies.

The association of CO_2 uptake with heat flux can be seen in Figure 3.1a,b. Large negative heat fluxes correspond to high CO_2 uptake by the ocean and large positive heat fluxes (into the ocean) correspond to CO_2 outgassing. The equatorial region however is an exception to this. Although there is a strong positive heat flux, strong Ekman transport moves equatorial waters before they have time to equilibrate with the atmosphere and CO_2 outgassing is somewhat weaker than otherwise (also see Fig3.2b).

Sarmiento et al. (2000) discussed the results obtained from ocean models used by three groups involved in the OCMIP-1 project: Max-Planck Institut Für Meteorologie (MPI) Maier-Reimer (1993); Institut Pierre Simon Laplace (IPSL) (Madec and Imbard, 1996; Aumont et al., 1998); Princeton University (Sarmiento et al., 1995; Murnane and Le Quéré, 1999). None of the models were coupled to an atmo-

experiment	sea ice and mixing parameterization	boundary conditions
PI_evp_gm	ice dynamics GM	CO_2 = 280 orb = 1850
PI_noevp_gm	thermo ice GM	CO_2 = 280 orb = 1850
PI_noevp_nogm	thermo ice horizontal/vertical	CO_2 = 280 orb = 1850

Table 3.1: Preindustrial equilibrium experiments. Mixing parameterization used are either Gent McWilliam (GM) or standard horizontal/vertical diffusion. Sea ice is either wind driven (ice dynamics) or thermodynamic only (thermo ice). Boundary conditions for each experiment are for a preindustrial climate and are run to equilibrium with an atmospheric CO_2 concentration of 280 ppmv and orbital parameters for 1850.

sphere and none incorporated the GM parameterization for mixing associated with mesoscale eddies or a prognostic sea ice component. The OCMIP-1 models revealed similar global features, including a broad region of out-gassing in the equatorial Pacific, Atlantic and to a lesser extent Indian Oceans. In the IPSL model, the Southern Ocean was dominated by high uptake around 60°S, whereas in the MPI model it occurred closer to the coast of Antarctica, and in the Princeton model the uptake was widely distributed over the Southern Ocean.

Air-sea preindustrial CO_2 flux maps for three different model formulations of the UVic ESCM are shown in Figure 3.2. The model runs are referred to as: PI_evp_gm (as in Fig 3.1), which includes sea ice dynamics and the GM mixing parameterization; PI_noevp_gm, which includes thermodynamic only sea ice and the GM parameterization for ocean mixing; PI_noevp_nogm, which includes thermodynamic only sea ice and standard horizontal-vertical diffusion (see Table 3.1). All three flux maps (and difference between them) are shown as they are each used as equilibria from which we conduct our perturbation experiments throughout the remainder of the chapter.

PI_noevp_nogm can be compared to other models which include similar parameterizations for sea ice and mixing. Our global pattern of out-gassing and uptake (Fig. 3.2e) is similar to that found in the OCMIP-1 models. The uptake in the Atlantic, however, extends further northward in the MPI, IPSL and Princeton models, which have more realistic representations of sea ice extent in this region, compared to that in Fig. 3.2e. There is some out-gassing north of this latitude in both the North Pacific and Atlantic due to near shore upwelling. Out-gassing also occurs in other regions of near shore upwelling, predominantly off the western coast lines of the

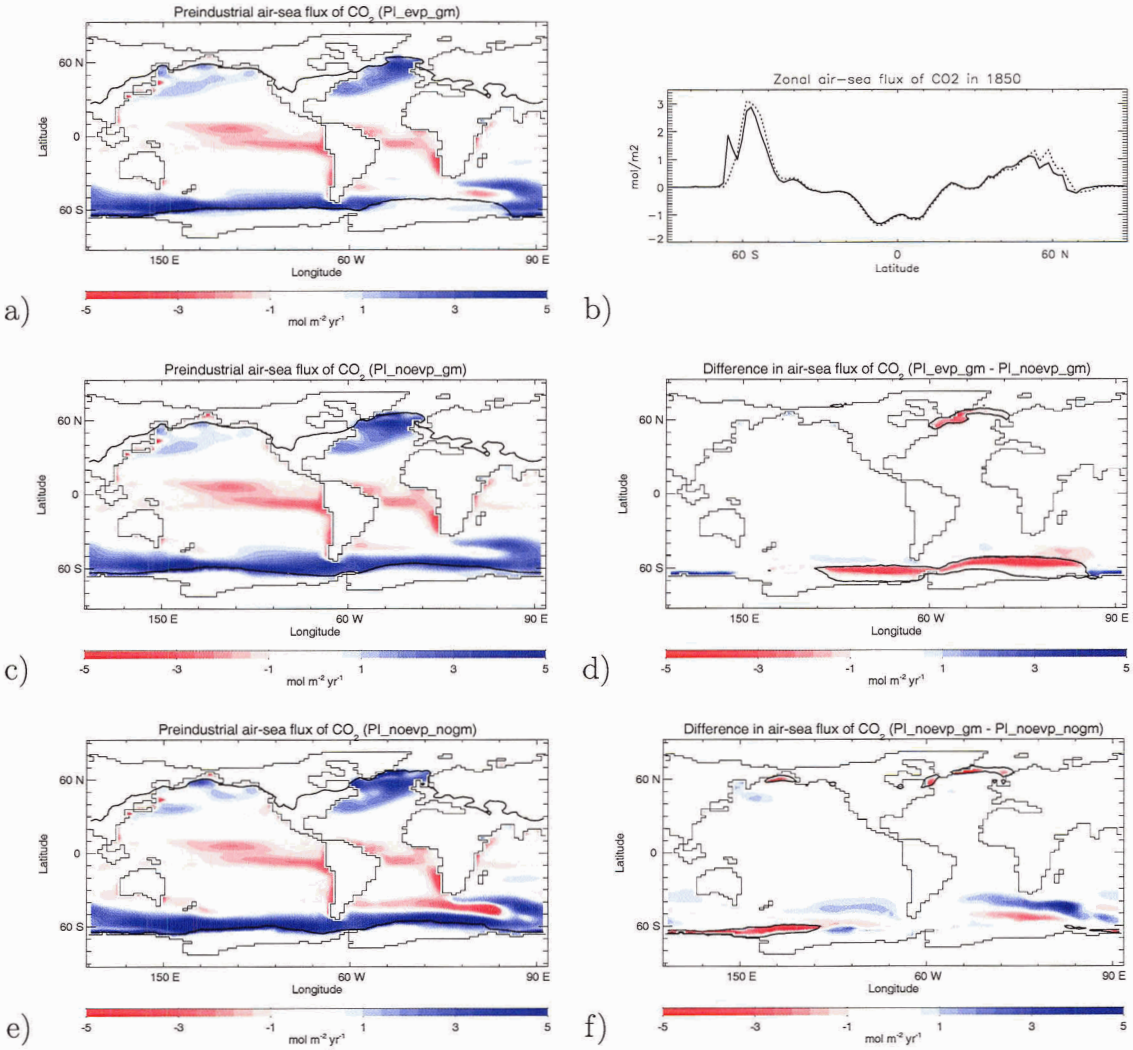

Figure 3.2: a,c,e) Annual-mean air-sea preindustrial CO_2 flux (mol m^{-2} yr^{-1}) for three different models, representing the effects of sea ice and mixing parameterizations. Blue regions indicate oceanic uptake of CO_2 and red indicates out-gassing to the atmosphere. Sea ice and snow (on land) extent is outlined in black. a) fluxes for the model which includes sea ice dynamics and GM (PI_evp_gm), c) includes thermodynamic sea ice and GM (PI_noevp_gm) and e) includes thermodynamic sea ice and standard horizontal/vertical diffusion (PI_noevp_nogm). b) Annual-mean, zonally-averaged air-sea CO_2 flux (mol m^{-2} yr^{-1}) for PI_evp_gm (solid) and PI_noevp_gm (dotted). d) Difference in air-sea flux of CO_2 due to the inclusion of sea ice dynamics and f) difference in flux when GM is included.

Americas and Africa. Since deep waters tend to have high concentrations of carbon, upwelling along western boundaries leads to an excess of dissolved carbon in surface waters.

In our model, the overestimate of sea ice cover limits the northward extent of carbon uptake to about 60°N. The total area covered by present day sea ice in the northern hemisphere in our model has been shown to be in good agreement with observations (Weaver et al., 2001). This indicates that the area of sea surface which is exposed to the atmosphere should not limit CO_2 uptake due to over estimates in the northern hemisphere. In the North Atlantic however, because the extent of sea ice is too far equatorwards, this will lead to a reduction in air-sea interaction and CO_2 flux. Another factor which will further influence uptake in this region is the production of NADW which forms too far south due to the southern extent of the sea ice edge.

Figures 3.2 a and c show similar general uptake and outgassing patterns although there are several notable differences due to the changes in sea ice and mixing parameterizations. Using the same model version, Saenko et al. (2002) found that wind driven sea-ice dynamics affects CFC-11 uptake. Not surprisingly, this is also the case with CO_2 (Fig. 3.2b and d). When sea ice dynamics is included in the model (Figs. 3.2a and b; solid line), more realistic formation of Antarctic Intermediate and Bottom water occurs, compared to the case which includes a thermodynamic representation of sea ice. As such there is greater CO_2 uptake at higher southern latitudes. There is also slightly less uptake north of about 45°N with the inclusion of sea ice dynamics, although the equatorial and subtropical regions show almost no change. When GM and standard horizontal-vertical diffusion are compared however (Figs. 3.2c, e and f), there are larger differences in CO_2 flux due to the mixing scheme (over sea ice parameterization shown in Fig 3.2d) in equatorial and subtropical regions, and very little change in carbon uptake due to differences in the sea ice edge. Figure 3.2f shows the largest differences in CO_2 flux where either convection or downwelling occurs in the model, with the most notable differences in the Southern Ocean, south of 45°S. The inclusion of GM in our ocean model tends to reduce convection and communication between the top and bottom of the ocean and has been shown to improve simulated distributions of CFC-11 and temperatures (Robitaille and Weaver, 1995). It should be noted however that uptake of CO_2 and CFCs differ in that CO_2 is chemically reactive in sea water and leads to longer equilibration time with surface waters ($\sim$1 year for CO_2 and days for CFCs). This may cause deep tracer inventories to be considerably different and carbon inventories cannot be directly inferred from

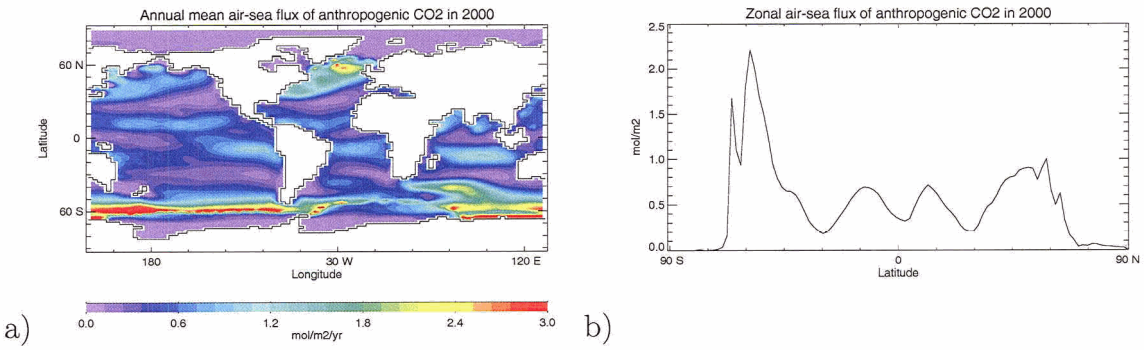

Figure 3.3: a) Map of annual mean air-sea CO_2 flux (mol m^{-2} yr^{-1}) of anthropogenic CO_2 in 2000 taken as the difference between the global flux map at year 2000 and the 1850 map shown in Fig. 3.2a. b) Annual mean zonal air-sea CO_2 flux (mol m^{-2} yr^{-1}) both figures show results with the pi_evp_gm experiment (sea-ice dynamics included) and PI_evp_gm is used as the initial condition.

CFC distributions (Sabine et al., 1999; McNeil et al., 2003).

3.3.2 Anthropogenic carbon comparison

Only recently have coupled ocean-atmosphere general circulation models accounted for ocean carbon cycle feedbacks in simulations of the climate response associated with increasing anthropogenic CO_2 (Cox et al., 2000; Friedlingstein et al., 2001). Previously, ocean carbon-cycle models have assumed that the ocean circulation remains unchanged (Houghton et al., 1996). However, climate feedbacks due to increasing atmospheric CO_2 levels significantly alter the response of the carbon system by reducing ocean carbon uptake further (Sarmiento and Le Quéré, 1996; Joos et al., 1999). Changes to ocean stratification also affect uptake and storage in the Southern Ocean (Sarmiento et al., 1998; Caldeira and Duffy, 2000). Orr et al. (2001) concluded that the OCMIP-1 models overestimated Southern Ocean storage when compared to recent observational estimates. This is at least partly a result of these models not including the more realistic GM parameterization for mixing associated with mesoscale eddies and hence their models were likely subject to excessive deep convection in the Southern Ocean.

Present-day carbon fluxes

In order to examine the uptake of carbon under anthropogenic forcing, we carry out a transient simulation from the preindustrial (year 1850) equilibrium to the present (year 2000). To accomplish this task we increase the atmospheric concentration of CO_2 following the exponential profile of Weaver et al. (2000):

$$C(t) = C_{PI} e^{k(t-1850)^a} \tag{3.2}$$

where $C_{PI} = 280 ppmv$, $k = 7.944 \times 10^{-8}$, $a = 3.0058$ and t is the year. This expression was obtained from a two parameter exponential fit (k and a) of the observed 1850-1990 increase in atmospheric CO_2 and other greenhouse gases used by Mitchell et al. (1995). Inherent in our approach is the assumption that prior to 1850, the ocean carbon cycle was in steady-state. We further assume, as a first approximation, that the subsequent anthropogenic perturbation to the natural carbon cycle, caused by fossil fuel emissions and land use changes, did not influence biological activity in the ocean, i.e., there was no biological transport of anthropogenic carbon (Maier-Reimer and Hasselmann, 1987; Farquhar et al., 2001). Nevertheless, we should caveat our assumption with the fact that biology might still have an effect on the solubility pump through its influence on the vertical distribution of DIC, even if the biology itself did not change.

The anthropogenic uptake of CO_2 in 2000 (Fig. 3.3a) reveals a net positive flux into the ocean in all regions. The 2-D uptake field shows patterns similar to those at 1850 (Fig. 3.3b), with the largest fluxes still in the high latitude regions, especially the Southern Ocean (up to 3.2 mol m^{-2} yr^{-1}), where deep mixing occurs. Data based estimates indicate that the Southern Ocean fluxes found in previous modelling studies may be overestimated (Orr et al., 2001). In our experiment we use PI_evp_gm as an equilibrium, which includes sea ice dynamics and the more realistic GM representation of ocean mixing. We once more find that there is slightly less anthropogenic uptake in the high latitude regions than found in these earlier modelling studies. In the experiment PI_noevp_gm, with a thermodynamic-only representation of sea ice, the total carbon inventory was 178 Pg C more than PI_evp_gm, which includes sea ice dynamics, due exclusively to an increase in air-sea CO_2 flux. After we force each model to present day with Eqn.3.2, the experiment with thermodynamic-only sea ice increases from its initial state by 107 Pg C, whereas that with sea ice dynamics increases by only 96 Pg C after 150 years of CO_2 forcing. This demonstrates the relatively large effect that model parameterizations have on ocean storage of anthro-

pogenic CO_2.

The zonally averaged flux map in Fig. 3.3b shows minima around the equatorial and subtropical gyre regions. Equatorial upwelling brings waters that are normally high in DIC from depth to the surface. Nevertheless, these same waters are low in anthropogenic carbon as the 20th century uptake hasn't had enough time to penetrate to depth. Since these waters have little anthropogenic CO_2 in them, the partial pressure in the atmosphere is still higher than that of the underlying water and there is a net reduction in CO_2 outgassing in this region.

Ekman transport moves equatorial waters towards the subtropics where they are exposed to the atmosphere before sinking in the subtropical gyres. Here there is little uptake of anthropogenic carbon due to equilibration with the atmosphere during transport. The high uptake on either side of the equator is associated with the equatorial winds which increase uptake through an increased CO_2 transfer velocity as given by Equation 2.66.

Although there is an initial net uptake of CO_2 across the atmosphere-ocean interface under anthropogenic forcing, the ocean can not take up all of the excess CO_2 over the relatively short time scale associated with the perturbation. It is well known from both box model and general circulation model studies that the time period over which the anthropogenic perturbation is carried out largely determines the CO_2 storage capacity of the ocean (Maier-Reimer and Hasselmann, 1987). The buffering capacity of surface waters decreases with increasing atmospheric CO_2 concentration as carbonate is reduced in surface waters (through a forward reaction of Eq. 2.64), which in turn increases the partial pressure of CO_2 (pCO_2) in the surface waters and reduces uptake. Deep water formation also plays a key role as surface waters that are saturated in CO_2 require transport to the deep ocean before further atmospheric CO_2 can be drawn down. As deeper waters ventilate over long time scales, there is an excess of CO_2 that accumulates in the atmosphere.

We also note that our model air-sea fluxes are difficult to compare with observationally based estimates, for e.g. Takahashi et al. (1997), as biological processes are an inherent part of the measurement of surface ocean pCO_2 since phytoplankton take up CO_2 during photosynthesis. Although this is the case, our estimates still show good general agreement with these estimates, with high uptake in the high latitudes and outgassing in the equatorial regions. A better comparison can be made between our model present day DIC inventories and observational based estimates of anthropogenic carbon storage which remove affects of biological activity (inherent is the assumption that biological activity does not change under increased atmospheric

experiment	initial condition	forcing
pd_evp_gm	PI_evp_gm	280-367
pd_noevp_gm	PI_noevp_gm	280-367
pd_noevp_nogm	PI_noevp_nogm	280-367

Table 3.2: Present day perturbation experiments. Atmospheric CO_2 concentration is forced in each experiment to 367 ppmv according to Eqn.3.2. The initial condition is also shown and mixing and sea ice parameterizations for these experiments are shown in Table 3.1.

CO_2 concentrations), and is discussed in the next section.

Anthropogenic DIC

We have seen that the largest magnitude fluxes of anthropogenic CO_2 occur in the high latitude regions. The increase in the ocean carbon inventory since the preindustrial era is predominantly driven by the air-sea gas exchange due to the increased partial pressure in the atmosphere (Wallace, 2001). In regions where air-sea gas exchange is efficient and where deep, poorly ventilated ocean waters low in anthropogenic CO_2 and DIC come in contact with the surface, high uptake will occur. Modelling the uptake of anthropogenic CO_2 is a critical step in understanding future uptake under potentially altered circulation and understanding where this carbon is stored is equally important. Our understanding of where anthropogenic carbon is stored has improved due to a technique developed by Gruber et al. (1996), which allows the oceanic component of anthropogenic CO_2 to be estimated from observations. Although high uptake occurs in the Southern Ocean, Caldeira and Duffy (2000) have shown, in a modelling study, that the storage of anthropogenic carbon is low due to the transport of carbon along isopycnals into the Subtropical Convergence in a modelling study. This result confirmed the finding of observationally based estimates carried out by Gruber et al. (1996) and Sabine et al. (1999), using the technique of Gruber et al. (1996) for the Indian Ocean, that found little storage of carbon in the Southern Ocean and the highest column inventories of anthropogenic CO_2 in the Subtropical Convergence. Comparisons between model and observationally based estimates have found that three-dimensional GCM estimates are more consistent with these observationally based estimates than two-dimensional zonally averaged models (Stocker et al., 1994; Sarmiento et al., 1995; Wallace, 2001; Gruber et al., 1996; Gruber, 1998; Sabine et al., 1999).

Figure 3.4 shows the anthropogenic carbon in both north and south Atlantic sections at 24°W for three versions of the model and are used to make a qualitative

comparison with observational based estimates of Gruber et al. (1996). The model versions differ in their parameterizations for both sea ice and sub-grid-scale tracer mixing. Each experiment is outlined in Table 3.2. Results shown in the top panel (Figs. 3.4a,b) include dynamic sea ice and GM mixing, the middle panel (c,d) ignore dynamics (thermodynamic-only) sea ice and GM mixing and the bottom panel (e,f) include thermodynamic-only sea ice and standard horizontal/vertical mixing. In the Southern Ocean movement of wind driven sea ice away from the Antarctic continent provides increased uptake and the carbon inventory in Fig. 3.4a is higher south of 60°S than in the other models. Carbon uptake however, is found to occur slightly south of the maximum column inventories in this region since uptake occurs where isopycnal surfaces outcrop and is then transported northwards (Gruber et al., 1996; Sabine et al., 1999). This is consistent with results of Caldeira and Duffy (2000) using a similar ocean model. Fig. 3.4e shows the model which includes standard horizontal/vertical mixing, where tracer mixing does not occur along isopycnals, and there is no horizontal gradient of DIC south of about 50°S where DIC concentrations are uniform through the column to 1000 m depth.

A comparison of observationally based estimates (Gruber et al., 1996) gives the best agreement the our model verstion (pd_evp_gm) which includes sea ice dynamics and GM mixing (Fig. 3.4a). Several discrepancies exist between our model and the observationally based analysis of Gruber et al. (1996) however. Tracer surfaces outcrop less steeply in the Southern Ocean compared to the estimates and do not penetrate as deeply between 35°-50°S. In the equatorial region tracer penetration is also too shallow, which may indicate that upwelling is too strong in the model. The high surface DIC concentrations between 10°-30°S however are in good agreement with the observationally based estimates of $\sim 45 \mu$mol kg^{-1}.

In the northern Atlantic the main differences between the model versions occur north of 45°N where unrealistic penetration to 1000 m of the tracer occurs in the model versions where thermodynamic-only sea ice and standard horizontal/vertical mixing are used (Figs. 3.4d,f). Again Fig. 3.4b, which includes both sea ice dynamics and GM mixing, agrees the best with observationally based estimates in this region (Gruber et al., 1996). The most notable disagreements are in the north Atlantic where the concentration of the tracer is slightly too low at 1000 m depth and ~15°N where upwelling in our model is probably too strong causing tracer concentrations to be slightly lower than the observationally based estimates.

Although most models show good agreement of globally averaged anthropogenic CO_2 fluxes (Sarmiento et al., 2000; Orr et al., 2001), there are large regional difference

in uptake and storage between models. The largest differences between global carbon uptake in three-dimensional GCMs exist due to differences in mixing parameterizations and sea ice. Whether models include sea ice components, and how these are represented, can lead to large differences in carbon uptake in high latitudes (Wallace, 2001). Since these regions play a pivotal role in the uptake of anthropogenic CO_2, it is important that new observationally based estimates are made in order to improve our modelling efforts and our understanding of how uptake and storage of carbon in the ocean may change under increased atmospheric CO_2 concentrations.

Future carbon uptake

To determine how much anthropogenic CO_2 can be potentially sequestered through dissolution into ocean waters, we force the atmospheric CO_2 concentration in the model according to Eq. 3.2 and stop the forcing at 367, 539, 712 and 1008 ppmv, corresponding to years 2000, 2050, 2075 and 2100, respectively. Through changes in the buffering capacity (discussed earlier in this chapter), it is thought that the oceans can potentially take up 85% of the atmospheric CO_2 increase from a preindustrial concentration of 280 ppmv (Houghton et al., 1996). However climate feedbacks such as reduced sea ice extent, circulation changes which include NADW production, and increased SSTs, which reduces CO_2 solubility in surface water, are not accounted for in this projected estimate of carbon uptake. In order to better understand the effects of climate feedbacks on carbon uptake (and subsequently what percentage of the atmospheric CO_2 increase the oceans can potentially take up), the following suite of experiments is carried out.

Each experiment is outlined in Table 3.3. The initial condition for these experiments is PI_noevp_gm which does not include sea ice dynamics. Due to the large number of experiments which have been carried out, we have not included sea ice dyanamics as it is computationally more expensive when included. As we will show later, the difference in ocean carbon uptake with the inclusion of dynamic sea ice, is shown to be at most 2%, although we find there are large regional differences in uptake associated with the inclusion of wind driven sea ice. Throughout the remainder of this chapter, the term 'anthropogenic' carbon will refer to the increase in either atmosphere or ocean carbon inventories due to an increase in atmospheric CO_2 concentration above 280 ppmv (representing a preindustrial concentration). Upon turning off the forcing, the atmospheric CO_2 concentration is allowed to freely evolve through the air-sea exchange of CO_2, and the model is integrated to equilibrium. Our approach examines a hypothetical and highly idealized policy option that allows a

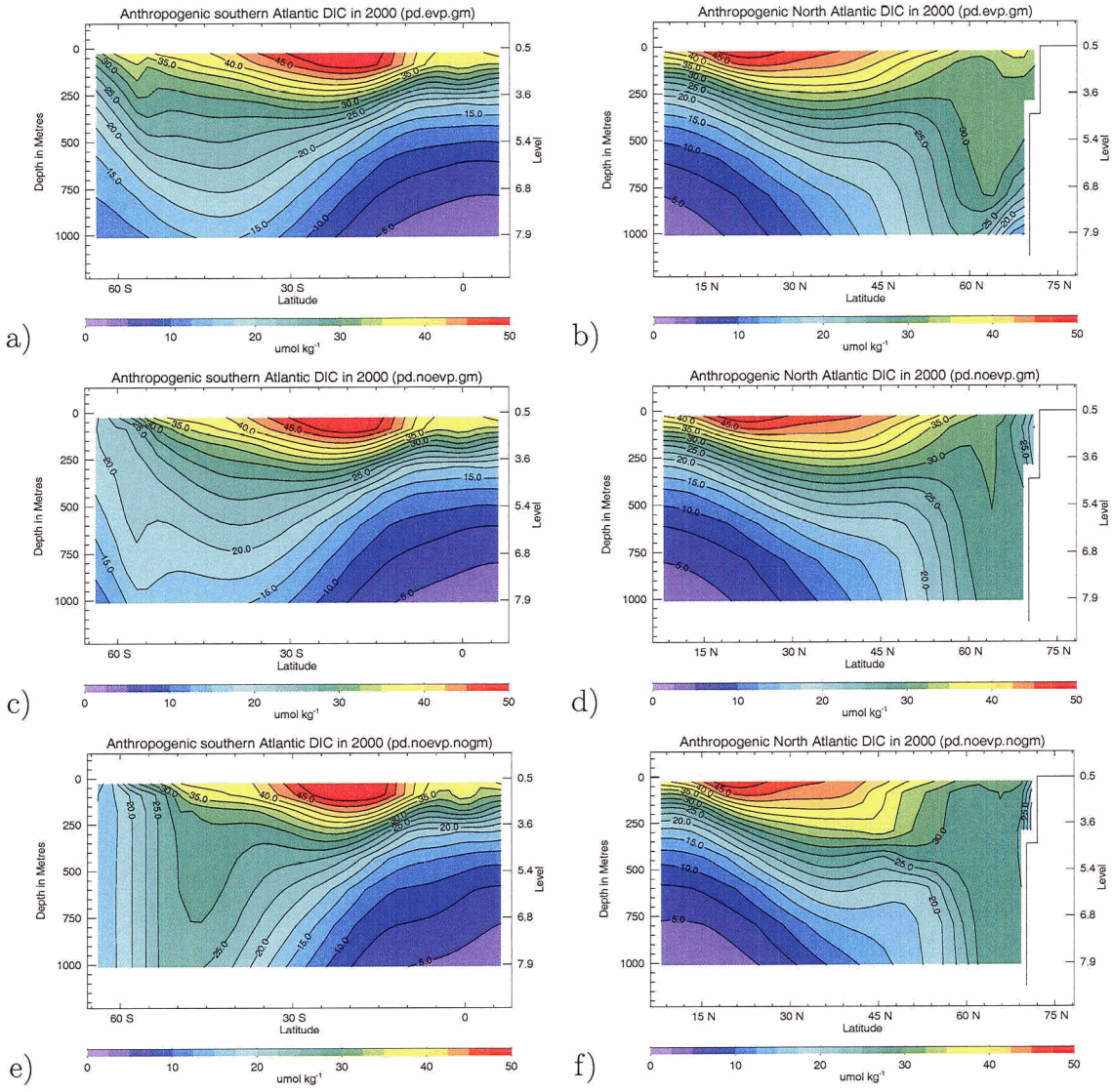

Figure 3.4: Zonally averaged anthropogenic DIC in the Atlantic in both hemispheres. (a,b) show maps for model runs which include dynamic sea ice and GM mixing. (c,d) include thermodynamic sea ice and GM mixing. (e,f) include thermodynamic sea ice and standard horizontal/vertical mixing. These maps show high storage of carbon in the subtropical regions, where high uptake in the high latitudes is transported along isopycnals.

experiment	initial condition	forcing (ppmv)
pert.367	PI_noevp_gm	280-367
pert.539	PI_noevp_gm	280-539
pert.712	PI_noevp_gm	280-712
pert.1008	PI_noevp_gm	280-1008
pert.367.fix	PI_noevp_gm	280-367 50 yrs const at 367
pert.539.fix	PI_noevp_gm	280-539 50 yrs const at 539
pert.712.fix	PI_noevp_gm	280-712 50 yrs const at 712
pert.1008.fix	PI_noevp_gm	280-1008 50 yrs const at 1008
pert.539.fix.100	PI_noevp_gm	280-539 100 yrs const at 539
pert.539.fix.150	PI_noevp_gm	280-539 150 yrs const at 539
pert.539.fix.200	PI_noevp_gm	280-539 200 yrs const at 539

Table 3.3: Anthropogenic perturbation experiments. PI_noevp_gm, which includes thermodynamic sea ice and GM mixing, is used as an initial equilibrium experiment for each. This initial condition is used as it is computationally less expensive and many experiments were carried out. The forcing is also shown which follows Eqn. 3.2 and then is either removed and allowed to equilibriate or held constant for a certain number of years before being removed (as indicated in the .fix experiments).

continuation along the 'business-as-usual' emission path until some time in the future when all anthropogenic emissions are suddenly turned off. In particular, it allows us to perform various perturbation experiments in order to determine the stability of the climate system in response to an increase in anthropogenic CO_2. For example, it might be possible to surpass the point of no return, whereby climatic feedbacks acting on the ocean carbon cycle inhibit further uptake of CO_2 into the ocean, and the atmosphere responds with a positive feedback whereby atmospheric CO_2 continues to increase even after the forcing is removed.

The results from our experiments (Fig. 3.5a) show that in all cases the ocean takes up 65-75% of the excess CO_2 over the equilibration time scale of about 1400 years (also see Table 3.4) . Table 3.5 lists the total atmosphere and ocean carbon inventories for each experiment outlined in Table 3.3. These are calculated when the forcing is removed (columns 2,3) and once the system comes to equilibrium (columns

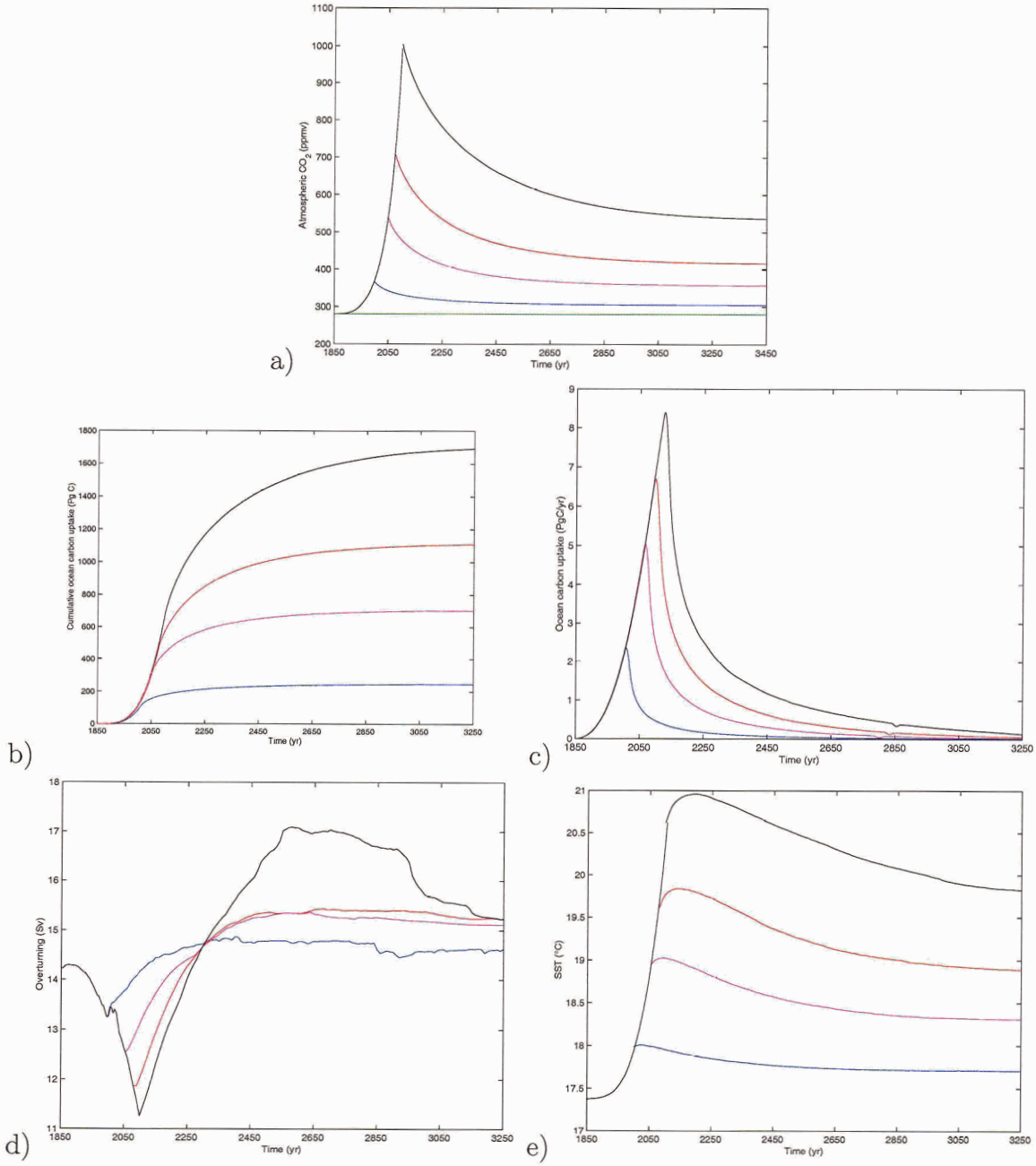

Figure 3.5: a) Atmospheric CO_2 (ppmv); b) total cumulative ocean carbon (Pg C); c) annual carbon uptake by the ocean (Pg C yr^{-1}); d) maximum North Atlantic overturning streamfunction (Sv); e) global-mean SSTs (°C). The model is forced with atmospheric CO_2 concentration according to Eq. 3.2 and released at 367 ppmv (blue - pert.367), 539 ppmv (purple - pert.539), 712 ppmv (red - pert.712) and 1008 ppmv (black - pert.1008), corresponding to years 2000, 2050, 2075 and 2100, respectively. Table 3.3 shows all perturbation experiments.

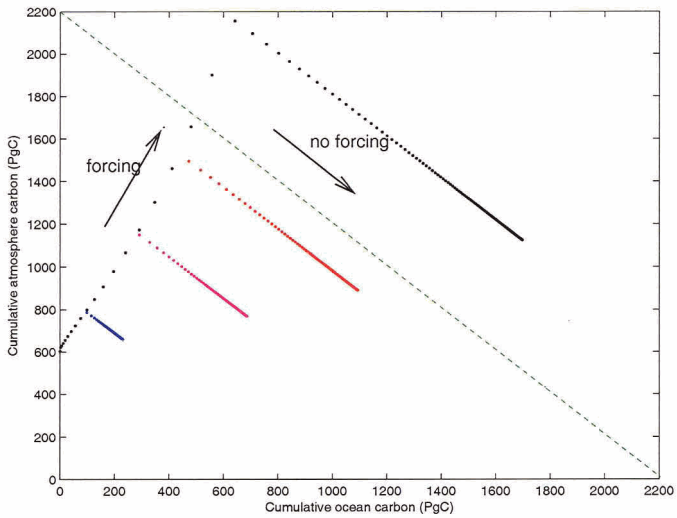

Figure 3.6: Total cumulative atmospheric carbon against ocean carbon (Pg C). The green horizontal line indicates an example line of constant total carbon. Arrows indicate the direction the system is being forced over time and when forcing is removed (no forcing). Each experiment shows atmospheric carbon increasing at a much quicker rate than oceanic carbon, while the atmospheric CO_2 is being prescribed over time. After the atmospheric forcing is removed, each experiment maintains a level of constant total carbon (parallel lines) and the ocean continues to take up atmospheric carbon until equilibrium is reached. Smaller spaces between data points represent the systems is near equilibrium. Experiments correspond to those in Fig. 3.5 and represent pert.367 (blue), pert.539 (purple), pert.712 (red) and pert.1008 (black) experiments.

4,5). The total increase in atmosphere and ocean carbon, which can be thought of as total emissions, is also listed in column 6. One can also see that the total carbon in the atmosphere-ocean system when the forcing is turned off is equivalent to the amount of carbon once a new equilibrium is established (i.e. (column 2 + column 3) = (column 4 + column 5)). [1] While the atmospheric CO_2 is forced, the ocean is taking up a significant amount of the carbon that is released over this time, as shown in Figure 3.5b. After the forcing is removed however, the atmosphere-ocean system has a fixed amount of carbon in it and the ocean continues to take up a significant percentage of the atmospheric amount over the equilibration time scale (Table 3.4). In no case does a positive feedback occur in which there is no further uptake. In addition, the control run, whereby the atmospheric concentration of CO_2 is allowed to freely evolve from year 1850 onward and no anthropogenic perturbation is added (Fig. 3.5a - green curve), shows no variation in oceanic uptake. This shows that there is no drift inherent in the carbon system and that the total carbon is conserved.

Fig. 3.6 shows the cumulative ocean carbon against cumulative atmospheric carbon (PgC). The direction of atmospheric CO_2 forcing is indicated by the arrows. As the atmospheric CO_2 increases, cumulative atmospheric carbon increases and cumulative ocean carbon also increases, although the uptake by the ocean is much slower to respond during this initial increase. Once the atmospheric forcing is stopped, the ocean continues to take up carbon from the atmosphere. The green line indicates constant total carbon and it is clear that once the atmospheric forcing is turned off, the total carbon remains constant in each experiment. The spaces between data points also indicate the rate at which the carbon is being taken up where closer data points indicate the system is near equilibrium. This rate will be discussed in more detail later. Total emissions can also be inferred from this figure. Since our model does not include a terrestrial biosphere, there is no sink on land for anthropogenic carbon and the carbon either goes into the atmosphere or ocean. Anywhere along the curves, one can add the total carbon in both the ocean and atmosphere (minus the initial preindustrial amount) to determine the total emissions (calculated in Table 3.5). Once the atmospheric forcing is removed, this is equilivalent to stopping the emissions, and while the total amount of carbon in the system remains constant, carbon continues to be removed from the atmosphere and taken up by the ocean.

Corresponding to results from numerous studies using coupled models of varying

[1]The percent uptake by the ocean can be calculated from Table 3.5 using the total decrease in atmospheric CO_2 after forcing is removed (column 2 - column 4) divided by the total atmospheric perturbation (column 2).

Experiment	uptake (%)	uptake (%) (50 yrs fixed)	difference (%)
pert.367	72	64	8
pert.539	70	64	6
pert.712	69	62	7
pert.1008	65	59	6

Table 3.4: Equilibrium uptake of anthropogenic CO_2 by the ocean (%) for four experiments where the atmospheric CO_2 concentration is allowed to freely evolve after it reaches 367, 539, 712 and 1008 ppmv. Also included is the equilibrium uptake (%) for the four experiments where the atmospheric CO_2 concentration is held fixed for 50 years at its elevated levels before being allowed to freely evolve. The difference between column 2 and column 3 is shown in column 4.

complexity (e.g. Manabe and Stouffer, 1994; Sarmiento and Le Quéré, 1996; Stocker and Schmittner, 1997), our experiments show a slight reduction in the strength of NADW formation during the transient phase of atmospheric CO_2 increase (Fig. 3.5d). The largest decrease occurs in the pert.1008 experiment where the overturning strength at 2100 is reduced by about 3 Sv. Once the forcing is removed, the overturning reestablishes itself and in all cases arrives at an equilibrium value slightly (< 1 Sv) above the initial preindustrial level of 14.2 Sv. In all cases some formation of NADW occurs. Of course, whether or not the THC collapses is highly dependent on both the rate of CO_2 increase (Stocker and Schmittner, 1997), as well as the parameterization of sub-grid-scale mixing (Manabe and Stouffer, 1999; Schmittner and Weaver, 2001). Different anthropogenic CO_2 uptake patterns would likely have arisen if a collapse of the THC were to have occurred.

In addition to changes in the strength of the THC, increased SSTs lead to a reduced solubility in the ocean surface waters. Sarmiento and Le Quéré (1996) found a warming of 2.4°C in SST for a $2\times$ CO_2 climate (600 ppmv), representing a slightly higher climate sensitivity of their model compared to ours. In our case, the maximum global mean SST increase is about 1.5°C, 2.1°C and 3.5°C for the pert.539, pert.712 and pert.1008 experiments, respectively (Fig. 3.5e). Nevertheless, it is difficult to compare our results directly with other studies as typically these other studies maintained a constant level of atmospheric CO_2 in their models after the initial transient increase, and few integrated the coupled system to equilibrium under a variety of scenarios.

Four additional runs were carried where atmospheric forcing is held constant at the maximum level for an additional 50 yrs before releasing it (shown in Fig. 3.7a). The

experiments correspond to pert.367.fix, pert.539.fix, pert.712.fix and pert.1008.fix and are shown in Table 3.3. Unlike the first suite of experiments (pert.367, pert.539, pert.712 and pert.1008) these experiments are slightly more realistic as emissions aren't stopped entirely after the forcing reaches its maximum atmsopheric CO_2 concentration. These experiments, together with the following suite of experiments, will enable us to carry out additional analyses to determine if the carbon uptake by the oceans is determined by the total increase in carbon inventory in the system.

In each experiment, the ocean is taking up a significant amount of carbon, while the maximum atmospheric CO_2 is held constant for 50 years. Although the atmospheric CO_2 concentration remains fixed, the increase in total emissions can be found by calculating the increase in the ocean carbon storage from the inital equilibrium carbon inventory (shown in Table 3.5, column 2). In this suite of experiments, the ocean has more time to equilibrate with the elevated atmospheric levels while the atmospheric CO_2 concentration is held fixed. In all cases, the additional amount of carbon in the ocean under elevated atmospheric CO_2, reduced the potential for total CO_2 uptake by 6-8%. Total atmospheric and ocean carbon amounts (and implied emissions) for all perturbation experiments are shown in Table 3.5, and the percent reduction can be calculated using these values. In the next suite of experiments, we examine the change in carbon uptake when atmospheric CO_2 concentration is held fixed for 50, 100, 150 and 200 years. This sensitivity analysis is performed for the 539 ppmv stabilization scenario (Fig. 3.7b).

As the atmospheric CO_2 concentrations is fixed at 539 ppmv for 50, 100, 150 and 200 years, the total amount of carbon in the system is increasing as the ocean is able to take up an additional amount of the total carbon which the climate system is forced with. This can be thought of in terms of emissions. As discussed previously, our model does not include a terrestrial biosphere so additional carbon added to the system goes into either the ocean or atmosphere. Fig. 3.8 shows total atmospheric and oceanic carbon for experiments corresponding to Fig. 3.7b after the forcing is removed. Once the atmospheric forcing is removed, the total atmospheric carbon is the same for each experiment (1160 PgC) while the total oceanic carbon is different for each. The increase in oceanic carbon is the additional amount taken up by the ocean while atmospheric CO_2 was held fixed over different periods at 539 ppmv. Once the forcing is removed, ocean carbon continues to increase while atmospheric carbon decreases (and the total carbon remains constant) until an equilibrium is reached.

Table 3.5 shows the total uptake by the ocean (Pg C) over the stabilization period for each of these experiments. Although the ocean is taking up additional carbon

Experiment	atm C forcing off	ocn C forcing off	atm C final	ocn C final	total C increase
pert.360	187	111	52	246	298
pert.539	558	312	164	706	870
pert.712	930	471	293	1108	1401
pert.1008	1568	674	545	1697	2242
pert.360.fix	187	190	67	310	377
pert.539.fix	558	485	204	839	1043
pert.712.fix	930	699	353	1276	1629
pert.1008.fix	1568	954	640	1882	2522
pert.539.fix.100	558	606	232	933	1165
pert.539.fix.200	558	825	278	1106	1384

Table 3.5: Uptake of anthropogenic CO_2 by the atmosphere and ocean for perturbation experiments shown in Table 3.3. All carbon (C) amounts are in PgC. Column 2 and 3 show the increase in atmosphere and ocean carbon, from the inital condition, after the forcing is removed. The equilibrium concentrations for both atmosphere and ocean have been subtracted out to show the total 'pertubation' or anthropogenic carbon. Column 4 and 5 show the atmosphere and ocean carbon amounts at the end of the experiment, when a quasi-equilibrium has been reached. These amounts also have the equilibrium atmosphere and ocean carbon subtracted. After the forcing is removed, the total atmosphere and ocean carbon is conserved and does not change. The total increase in carbon can be thought of as an increase due to emissions.

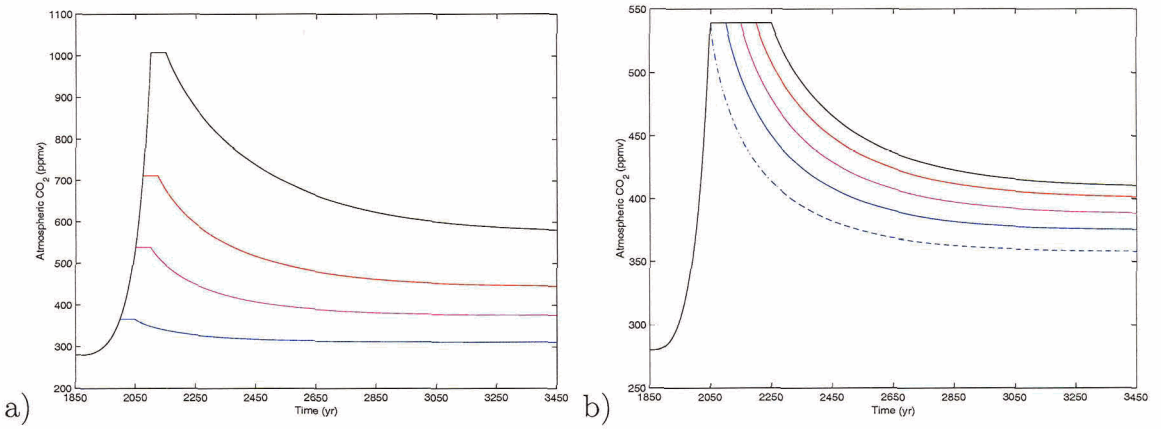

Figure 3.7: Atmospheric CO_2 (ppmv) as a function of time. a) As in Fig. 3.5a but with the atmospheric forcing fixed at the maximum level for an additional 50 yrs before releasing it. The curves correspond to: pert.1008.fix (black), pert.712.fix (red), pert.539.fix (purple) and pert.367.fix (blue). b) The fixed atmospheric CO_2 level of 539 ppmv is held for 0 (pert.539 - dotted blue), 50 (pert.539.fix - solid blue), 100 (pert.539.fix.100 - purple), 150 (pert.539.fix.150 - red) and 200 (pert.539.fix.200 - black) years.

under the forcing, the uptake of carbon over each 50 year period decreases over time and there is an increase in the total ocean carbon inventory at the end of the forcing. As the concentration of atmospheric CO_2 remains at 539 ppmv over this time, there are only small changes in SST and overturning circulation. Once the forcing is removed there is a decrease in uptake ~5% (calculated from Table 3.5) due primarily to the increase in the ocean carbon inventory. In total, there is a 20% reduction in uptake under the 200 year stabilization scenario compared to the instantaneous emission reduction scenario. Since the forcing for each experiment is removed at a fixed concentration of 539 ppmv, there is little change in uptake due to climate feedbacks (through changes in SST and overturning circulation) and the changes in uptake are primarily due to a reduction in the buffering capacity. After the forcing is removed, the experiments with a higher total carbon inventory will take up less carbon, due to a reduction in surface carbonate concentration which in turn increases the pCO_2, and thus more is left in the atmosphere. It is only at this point that climatic feedbacks affect ocean carbon uptake, although as the difference in atmospheric CO_2 between these experiments is ~50 ppmv, the effects of climate change are minor compared to the effects on uptake due to an increase in the buffering capacity.

Figure 3.9b shows the linear relationship between total carbon in the system after

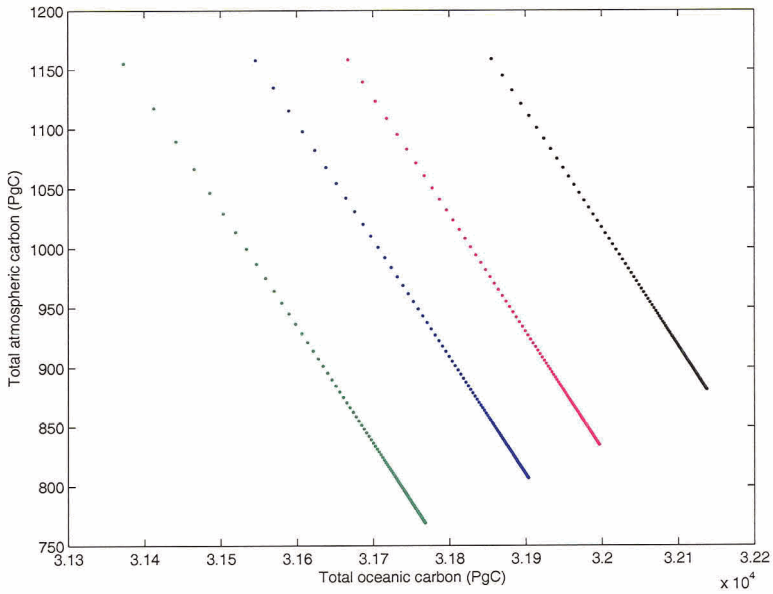

Figure 3.8: Total atmospheric and oceanic carbon for experiments corresponding to Fig. 3.7b after the constant forcing is removed. The experiments correspond to the following curves: pert.539 - green (no fixed forcing), pert.539.fix - blue, pert.539.fix.100 - pink and pert.539.fix.200 - black. Once the total atmospheric forcing is removed, the total atmospheric carbon is the same for each experiment while the total oceanic carbon is different for each. The increase in oceanic carbon is the additional amount taken up by the ocean while atmospheric CO_2 was held fixed over different periods at 539 ppmv. The additional oceanic uptake for each experiment can thus be thought of as emissions. Oceanic carbon continues to increase while atmospheric carbon decreases, while the total carbon remains constant, until an equilibrium is reached. The rate of change in carbon can be implied by the spacing of the data points, where closer points indicate the system is closer to equilibrium.

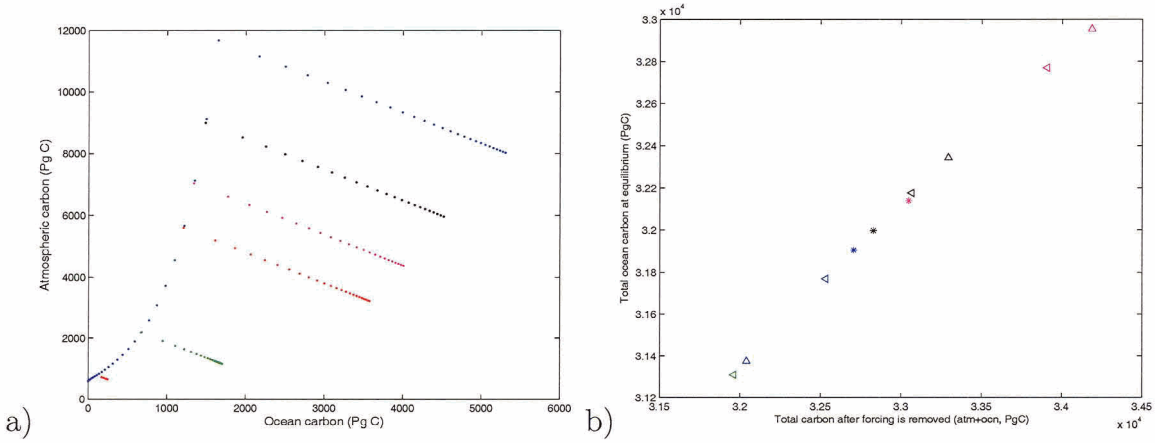

Figure 3.9: a) Atmosphere and ocean carbon (Pg C) shown from 1850 to 3450 for experiments pert.360 and pert.1008, corresponding to Fig. 3.5a, as well as additional experiments for 2570, 3233, 4131 and 5363 ppmv (starting from the same equilibrium experiment). This is similar to Fig. 3.6 however we extend this to add additional data from runs with increased atmospheric CO_2 forcing. b) shows the total carbon in the ocean and atmosphere after the forcing is removed versus the total final carbon in the ocean after a quasi- equilibrium is reached for all perturbation experiments in Table 3.3. It is clear that the total final amount of carbon the ocean takes up is dependent on the total input of carbon into the system introduced by the perturbation (equivalent to the amount of emissions). Also note that the amount of carbon after forcing is removed is conserved and is equilivalent to the total carbon in the atmosphere and ocean once a quasi-equilibrium is reached.

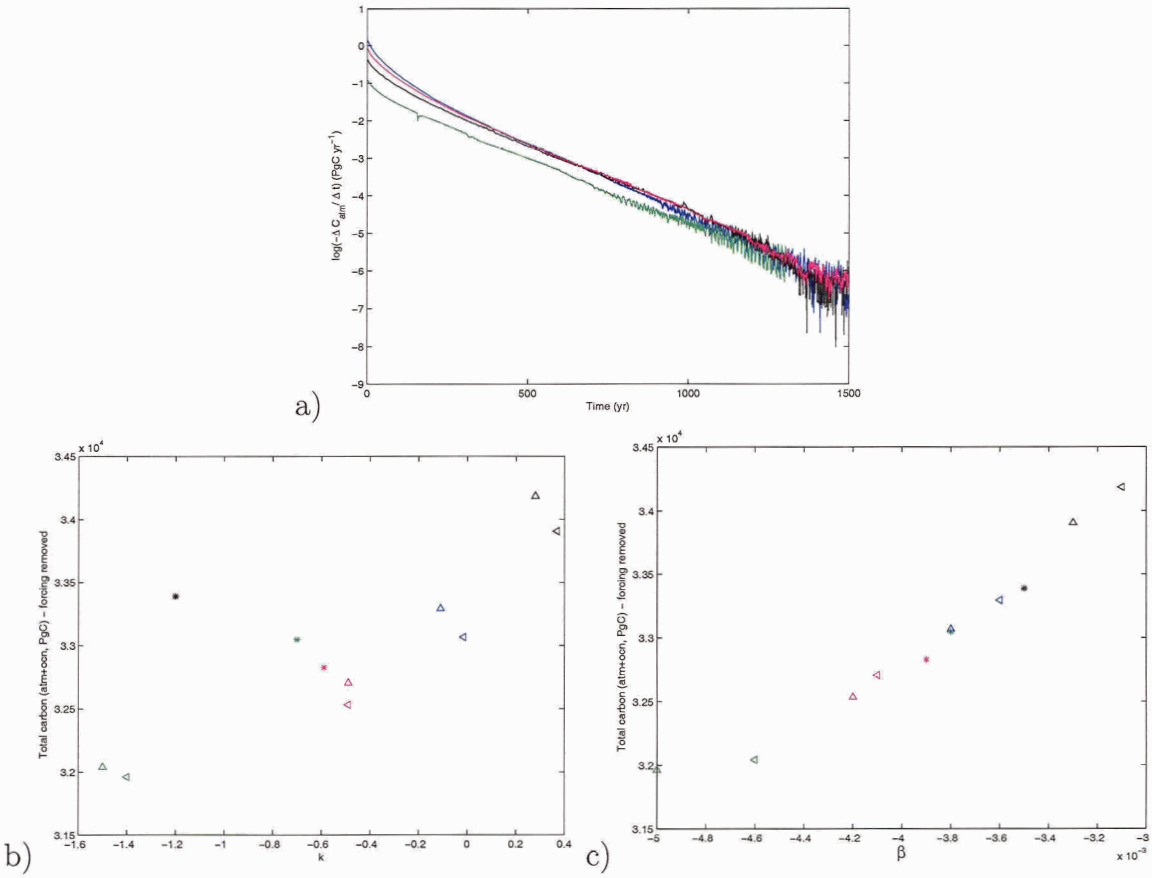

Figure 3.10: a) The rate of decrease in atmospheric carbon (log) over time for pert.539 (blue), pert.539.fix (pink), pert.539.fix.100 (black) and pert.539.fix.200 (green) experiments. This plot shows the linear relationship between the rate of decrease in atmospheric CO_2 (log) over time. From this relationship, we can also plot the slope (β) and intercept (k) for each experiment with the final amount of total carbon in the system. b) Total carbon (atmosphere and ocean) after the forcing is removed versus the intercept (k). Triangles (upright) are used for pert.1008, pert.712, pert.539 and pert.367 experiments, triangles (sideways) for pert.1008.fix, pert.712.fix, pert.539.fix and pert.367.fix experiments and stars for pert.539.fix.100, pert.539.fix.200 and pert.539.fix.500 experiments. There is a relationship between k within the separate suites of experiments, although no overall relationship for all experiments. c) shows the relationship between total carbon (atmosphere and ocean) after forcing is removed and the slope β from a), Eqn.3.3. There is clearly a linear relationship between β and the total amount of carbon.

forcing is stopped and total carbon in the ocean, for all experiments listed in Table 3.3. It is clear that the total final carbon depends on the total amount of carbon added to the system. This relationship, although simple, shows us that the total increase in carbon in the atmosphere-ocean system for the experiments in which atmospheric CO_2 concentration was held fixed over time, are still dependent on the total carbon that is put into the ocean. Although atmospheric CO_2 levels were held fixed over varying lengths of time, the total final carbon depends on the total increase in the ocean over this time as well. From this relationship, we can thus determine what the final ocean carbon concentration will be given the total carbon increase in the system.

Figure 3.9a shows the total increase in atmospheric carbon versus the total increase in ocean carbon. Evident is the change in the rate of uptake by the ocean (or rate of decrease in atmospheric CO_2) as the spacing between the data points changes over time (with smaller spaces indicating the system is closer to equilibrium). In order to determine whether there is a relationship between the total increase in carbon and the rate of decrease in atmospheric carbon (or uptake by the oceans), Fig. 3.10a shows the log-linear relationship between the rate of atmospheric carbon decrease over time. This relationship has been plotted and determined for each experiment, although is shown only for the pert.539 suite of experiments. This relationship can be written as;

$$\frac{dC_{atm}}{dt} = -ke^{-\beta t} \tag{3.3}$$

where C_{atm} is the concentration of atmospheric CO_2. In order to determine a further relationship, β and k have been determined for each experiment and plotted with total carbon (atmosphere and ocean) in Fig. 3.10b,c. β and k have also been plotted with total ocean carbon, however total carbon (atmosphere and ocean) yields a better linear relationship in the case of β. Although the relationship between k and total carbon is not apparent, there is a relationship between the suites of experiments, denoted with either triangles or stars. β however shows a clear linear relationship between total carbon in the system. From this relationship one can determine the rate of decrease in atmospheric carbon through the β parameter for any given total carbon added to the system.

Sensitivity to climate feedbacks

In this subsection, the effects of climate change on carbon uptake are examined. In particular, we are interested in determining whether there is any difference in the final atmospheric CO_2 concentration (equivalent to the total ocean carbon uptake) when the effects of climate change are included. All experiments in this section have been carried out with the inclusion of sea ice dynamics and the GM parameterization for mixing, using PI_evp_gm as an initial condition. The same set of experiments have also been run with thermodynamic sea ice (using PI_noevp_gm as the initial condition), and standard horizontal/vertical diffusion however the total reduction in atmospheric CO_2 concentration when climate feedbacks are considered are not significantly different from the results with sea ice dynamics and GM, so are not included. We note however that there are large regional differences in CO_2 uptake in the high latitude regions and with the inclusion of GM in our model and there is less overall uptake in the Southern Ocean, where GCMs generally overestimate CO_2 fluxes (Sarmiento et al., 2000). We also note, that Matear and Hirst (1999) found that the inclusion of GM reduced the positive feedback between climate change and carbon uptake such that the overall reduction in the total carbon inventory with the inclusion of GM was $\sim$ 80 Pg C. Since our aim is to determine whether climate feedbacks significantly affect the overall carbon uptake (and not total carbon inventory) we include only the experiments with GM and sea ice dynamics and leave the examination of the differences in ocean carbon inventory between the model versions, for future study. We further analyze the Atlantic DIC concentrations under climate change. We have shown that the inclusion of both sea ice dynamics and GM mixing lead to improved distribution in the north and southern Atlantic ocean, as compared to estimates of Gruber et al. (1996), so include this analysis here. In the following subsection, differences in carbon uptake due to the representation of sea ice are examined for select perturbation experiments in Table 3.5.

Two sets of experiments are run and follow those carried out in Section 3.3.2 for 539 and 1008 ppmv and are listed in Table 3.6. The first set is identical in all respects except for the inclusion of sea ice dynamics (using PI_evp_gm as the initial condition) and are referred to as pert.539 and pert.1008. In the second set of experiments, atmospheric CO_2 concentrations are similarly forced however, the effects of climate change are removed. Since the radiative forcing, associated with changes in atmospheric CO_2, is parameterized in the planetary long wave radiation flux in the UVic EMBM, we are able to easily remove the effects of climate feedbacks

experiment	initial condition	atm forcing (ppmv)	CO_2 radiative forcing
pert.539	PI_evp_gm	280-539	varies
pert.539.olw	PI_evp_gm	280-539	280 ppmv
pert.1008	PI_evp_gm	280-1008	varies
pert.1008.olw	PI_evp_gm	280-1008	280 ppmv

Table 3.6: Experiments carried out to asses the impacts of climate change on carbon uptake. All experiments use PI_evp_gm as an initial condition. Atmospheric forcing is either from 280-539 ppmv or from 280-1008 ppmv. The extension .olw denotes experiments which do not account for climate change and have CO_2 radiative forcing fixed at a preindustrial atmospheric CO_2 concentration of 280 ppmv. The pert.539 and pert.1008 allow CO_2 radiative forcing to vary according to the atmospheric forcing listed in column 3.

on carbon uptake by holding this value fixed at a preindustrial level of 280 ppmv. These experiments are referred to as pert.539.olw and pert.1008_olw. CO_2 in the atmosphere however is still allowed to evolve freely after the forcing is removed at years 2050 (pert.539.olw) and 2100 (pert.1008_olw) and continues to govern the air-sea interaction of CO_2.

Figure 3.11 shows atmospheric CO_2 concentrations, cumulative ocean carbon, overturning and SST for all four experiments. pert.539.olw and pert.1008.olw are plotted with dashed lines. Comparing pert.1008 and pert.1008.olw, atmospheric CO_2 is forced at the same rate for each experiment from 1850 to 2100. After the forcing is removed at 2100, the total amount of CO_2 does not vary by more than 2 ppmv throughout the runs. Cumulative ocean carbon, on the other hand, differs between the runs from 1850 even while the atmospheric CO_2 concentration is forced. In Table 3.7, atmosphere and ocean carbon inventories (in Pg C) are shown at year 2100 and at year 3450 for both pert.1008 and pert.1008.olw. Although both experiments have identical atmospheric carbon inventories after 2100, pert.1008.olw has 44 Pg C more stored in the ocean. After year 2100, pert.1008.olw initially has an atmospheric CO_2 concentration slightly less than pert.1008 until around year 2650 and then increases after this point to the end of the run at year 3450. In the ocean the excess remains positive throughout the run although more of the 44 Pg carbon excess is initially stored in the ocean in pert.1008.olw, by the end of the run the excess is almost evenly split between atmosphere and ocean where 23 Pg C of the excess are in the atmosphere and 21 Pg C in the ocean. Here we should also note that the total ocean carbon inventories are low due to the exclusion of biology in our model.

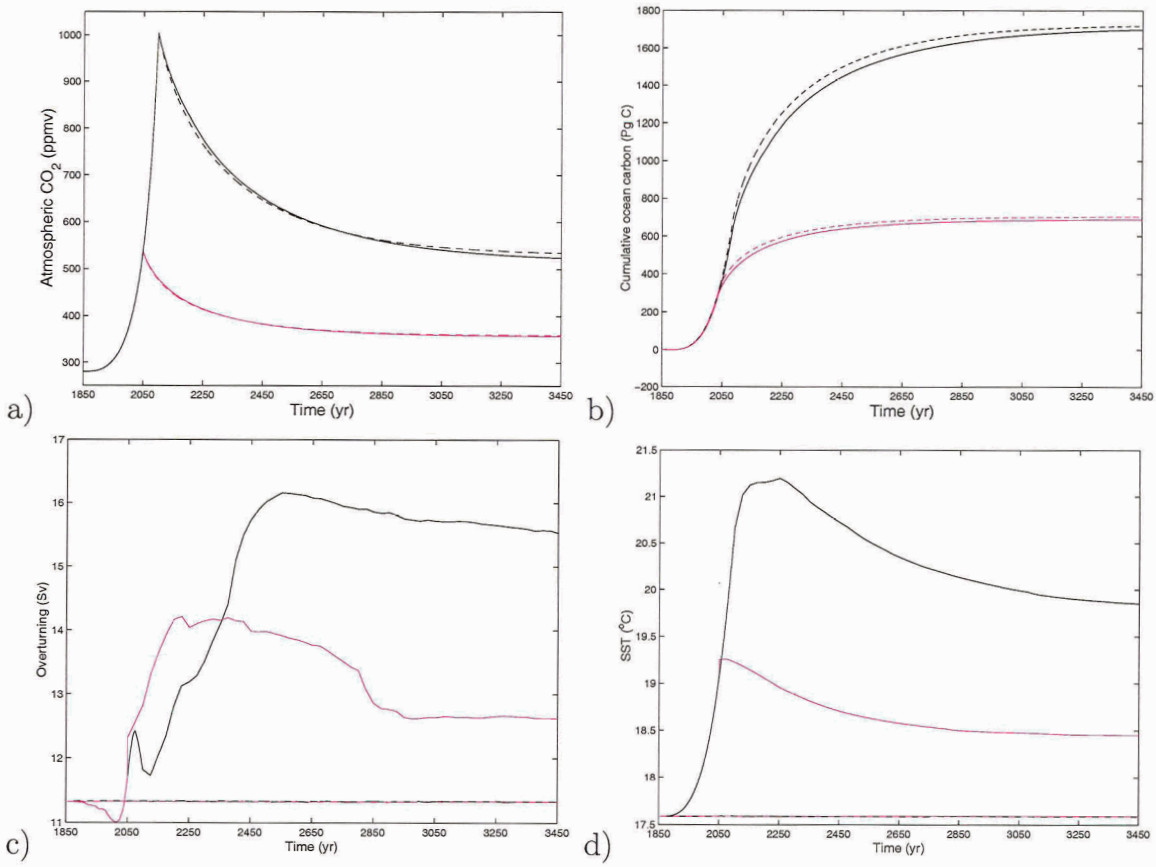

Figure 3.11: Atmospheric CO_2 (a), cumulative ocean carbon (b), overturning strength in the North Atlantic (d) and SST (e) plots for pert.539 (solid purple), pert.539.olw (dashed purple), pert.1008 (solid black) and pert.1008.olw (dashed black) experiments. Atmospheric CO_2 changes little between experiments with and without climate feedbacks, although the total ocean-atmosphere carbon inventory is greater by 44 Pg C in pert.1008.olw over pert.1008 (inventories shown in Table 3.7). Overturning and SST remain constant for pert.539.olw and pert.1008.olw experiments.

Experiment	atmospheric carbon	ocean carbon	total	difference
Experiment	year 2100	year 2100		
pert.1008.olw	2168	31567	33735	
pert.1008	2168	31523	33691	44
	year 3450	year 3450		
pert.1008.olw	1148	32602	33750	
pert.1008	1125	32581	33706	44

Table 3.7: Carbon inventories for pert.1008.olw and pert.1008. All carbon amounts are in Pg C. At year 2100 the forcing is removed and both experiments have the same amount of carbon in the atmosphere. pert.1008.olw has an excess of 44 Pg C over pert.1008 which is stored in the ocean. This excess is distributed fairly evenly between atmosphere and ocean at year 3450.

Although this affects the vertical gradient of DIC in our model, it does not influence the physical changes associated with the perturbation carbon uptake between these two experiments.

The overturning strength in the experiments which include climate change feedbacks (pert.539 and pert.1008) change little under a forced atmospheric CO_2 concentration. After the forcing is removed, the overturning increases by 3 Sv (pert.539) and 5 Sv (pert.1008). Changes in SST for these experiments are similar to the experiments without sea ice dynamics, shown in the previous section. The experiments which do not include the effects of climate change show no change in overturning or SST throughout the runs, which is expected.

Figure 3.12 shows difference maps for CO_2 flux, SST, zonally averaged temperature for the Atlantic and ice concentrations for 539 and 1008 ppmv runs, corresponding to Fig. 3.11. The differences show the effects of climate change feedbacks on uptake and are taken at year 2100. Although the differences in total carbon inventory between pert.1008.olw and pert.1008 is 44 Pg C (shown in Figure 3.11 and Table 3.7), the flux maps show that there are large differences in the magnitude of the uptake due to the climatic feedbacks acting on the carbon system. The general pattern is the same for both 539 and 1008 ppmv maps.

The difference flux maps show that including climate change in the 539 ppmv runs result in a small reduction in anthropogenic CO_2 uptake in the equatorial region ranging to a larger reduction of 4 mol m^{-2} yr^{-1}. When climate feedbacks are included, reduced sea ice cover leads to high CO_2 fluxes into the ocean in the high latitudes. Increased SSTs however, lead to reduced uptake over most of the ocean with the largest reductions occurring polewards of 45°N and 45°S. The bottom maps show

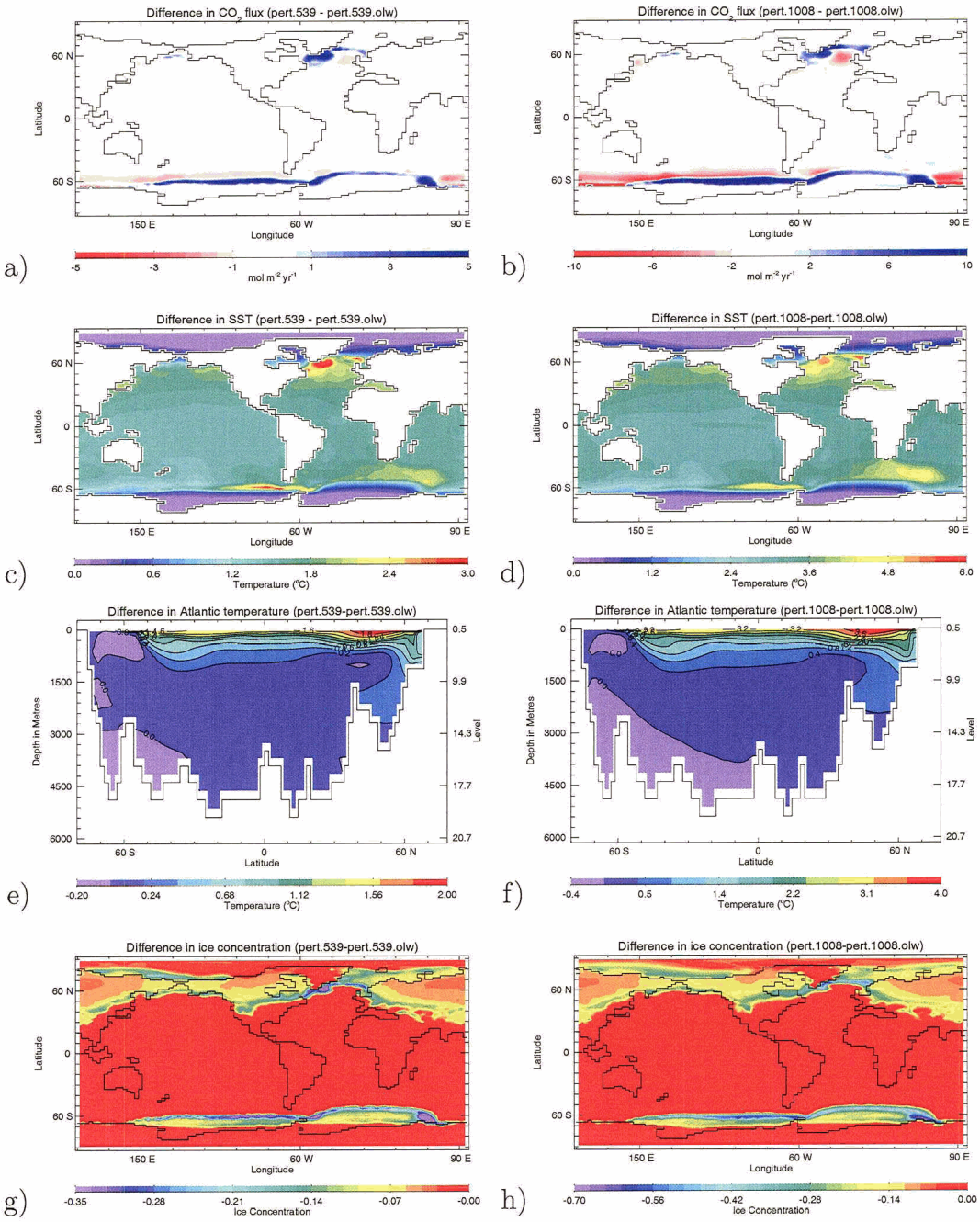

Figure 3.12: Difference plots for CO_2 flux (a,b), SST (c,d), zonally averaged temperature in the Atlantic (e,f) and ice concentration (g,h) for 539 and 1008 ppmv runs. Differences show effects of climate change feedbacks on uptake, temperature and ice concentration (includes snow on land which changes significantly in the northern hemisphere). All differences are shown at year 2100, at the end of the forcing.

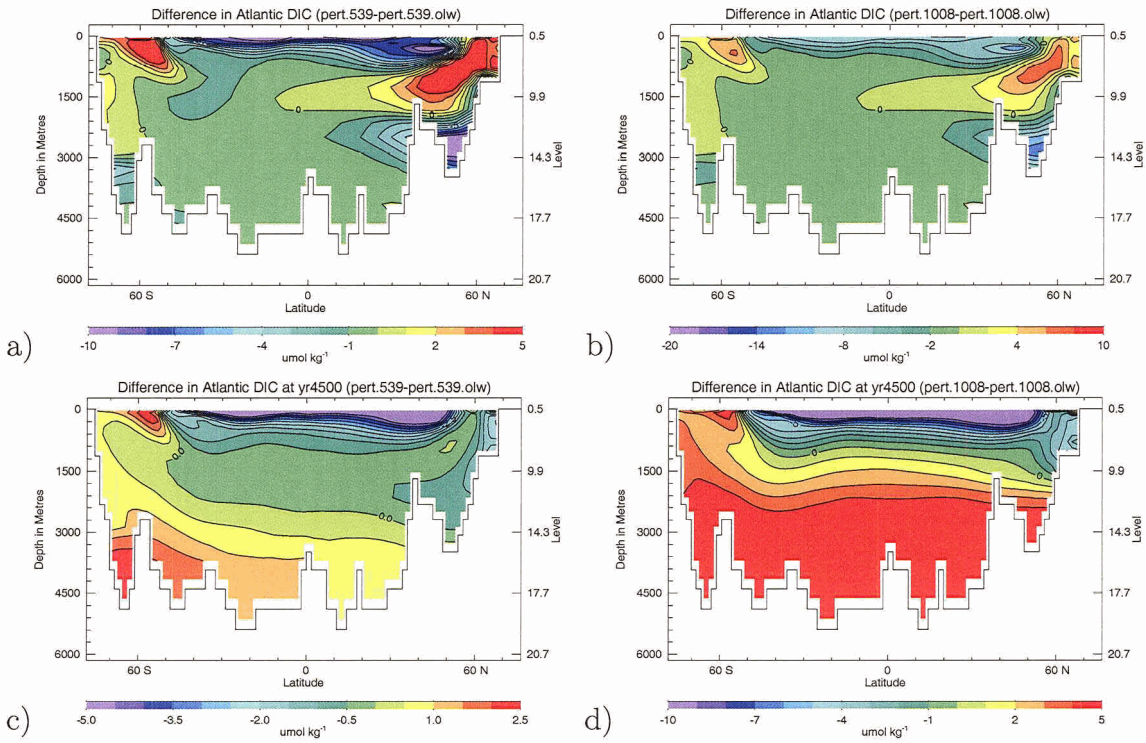

Figure 3.13: Difference plots for 539 and 1008 ppmv runs showing the effects of climate change feedbacks on Atlantic DIC at year 2100 (a,c) and year 3450 (b,d). At year 3450 the atmosphere-ocean system is in a quasi-equilibrium state.

differences in sea ice cover which also include differences in snow concentration on land. There are large differences in ice concentrations between the runs with climate change and without. The difference plots show that the inclusion of climate change leads to much lower ice concentrations in the high latitudes where climate feedbacks lead to a significant melt back in the concentration and ice edge. Since the high latitude oceans are the most important regions for carbon uptake, these differences in sea ice cover have a significant counteracting effect on the carbon uptake. Taken together, the experiments which include climate change have increased SSTs which lead to reduced carbon storage in the deep ocean, as shown in Table 3.7.

The CO_2 flux plot shows differences of 5 mol m^{-2} yr^{-1} between the 539 ppmv runs and a difference of about 10 mol m^{-2} yr^{-1} for the 1008 ppmv runs. If the effects of the overturning circulation on CO_2 uptake are considered, Figure 3.11 shows that the overturning in the climate change runs (pert.539 and pert.1008) reduces slightly over the first 2010 years and then increases abruptly. At the end of each run, it continues to increase until it reaches a maximum of 14.2 Sv for pert.539 and 16 Sv for pert.1008. Since the formation of deep water in the North Atlantic transports

carbon to the deep ocean, allowing more carbon to be taken up across the air-sea interface, a strengthening of the overturning is expected to increase carbon uptake in the North Atlantic.

Figure 3.13 shows the difference maps for DIC in the Atlantic basin at year 2100 and year 3450. Although the differences in DIC are not very large (at most 2% of the background) the negative difference in the region where North Atlantic Deep Water (NADW) is formed can be clearly seen in the North Atlantic (at year 2100) from the surface to a depth of about 2000 m. The transport of this water mass, which is reduced in DIC, leads to a negative difference in the overall deep ocean carbon inventory at the end of the runs at year 3450. Although reduction in solubility due to climate change leads to an overall positive difference in uptake seen in the difference maps, changes in sea ice cover and to a lesser extent changes in the production of NADW, lead to opposing effects and overall a small difference in the final atmospheric CO_2 concentration.

Sensitivity to representation of sea ice

The purpose of this subsection is to examine the sensitivity of the oceanic uptake of anthropogenic CO_2 to the representation of sea ice processes. As discussed in section 3.3.2, the largest uptake occurs in the high latitudes and in particular the Southern Ocean. These are the regions where sea ice is present and hence its proper treatment is potentially important in quantifying the role of the ocean in sequestering anthropogenic CO_2. In the following subsection, we expand our analysis to examine the parameterization of sub-grid-scale ocean mixing which is also important when considering high latitude processes. These are important sensitivity experiments as ocean models (Sarmiento et al., 2000) show the most significant inter-model differences in uptake in the high latitude regions.

The results of our sensitivity analysis, in which a dynamic sea ice component is incorporated (using PI_evp_gm for the initial condition), reveal different signs of the response in carbon uptake depending on the level of atmospheric CO_2 (Fig. 3.14). In general, as the climate system warms, the sea ice areal extent decreases. The 367 ppmv experiment shows greater uptake by the ocean when sea ice dynamics is excluded whereas the 1008 ppmv experiment shows greater uptake when it is included. Between these extremes are the 539 ppmv and 712 ppmv experiments. The 539 ppmv case shows less that 1% difference in uptake initially and converges to $\sim$0% after 1500 years; the 712 ppmv case, on the other hand, crosses the zero line near year 900, although the maximum variation is about $\pm$0.5%. Taken together, these differences

are not large given other uncertainties within the model, suggesting that when globally averaged, the inclusion of sea ice dynamics is not a controlling factor on the net uptake of anthropogenic CO_2. However, this is not the case locally (see Fig. 3.2b and section 3.3.1), where significant variations occur between the experiments with and without sea ice dynamics.

To illustrate the local effects associated with the inclusion of sea ice dynamics, we examine the results from the 1008 ppmv (Fig. 3.14a). In the Southern Ocean when sea ice dynamics are included, the northward areal extent expands through offshore transport relative to the thermodynamic-only case. At the same time, ice thickness nearer the Antarctic coast diminishes. Differences in Southern Ocean uptake in Fig. 3.14a, largely reflect differences in the sea ice extent. In the North Atlantic where the wind-driven sea ice transport is southward, similar results are found. There are two regions where greater fluxes of CO_2 across the air-sea interface are found. These occur in the Southern Ocean near the Antarctic continent where sea ice is transported northward. There is also a small region of uptake in the North Atlantic near the Labrador coast which is offset by the reduced uptake from the wind driven sea ice moving southward off the east coast of Greenland.

A question remains as to why the 367 ppmv experiment shows greater uptake by the ocean when sea ice dynamics is excluded whereas the 1008 ppmv experiment shows greater uptake when it is included (Fig. 3.14b). In the 1008 ppmv case, the sea ice has retreated significantly compared to the 367 ppmv case, as expected due to the larger radiative forcing and resulting warmer climate. In particular, sea ice has in some areas retreated back to the Antarctic continent whereas in the 367 ppmv experiment, sea ice growth still occurs away from the continent, as well as further south in the North Atlantic. In the 367 ppmv experiments, the sea ice extends further north from the Antarctic coast in the case including sea ice dynamics. This situation reverses when the atmospheric CO_2 concentration is increased to 1008 ppmv.

Sensitivity to ocean mixing

The GM parameterization for mixing associated with mesoscale eddies, ensures mixing of tracers along isopycnal surfaces, as in Redi (1982), and adds isopycnal thickness diffusion to account for the removal of potential energy from the stratification due to baroclinic instability. The new parameterization has been successful in improving the climatology of ocean models (Danabasoglu et al., 1994; Boning et al., 1995; Danabasoglu and McWilliams, 1995; Robitaille and Weaver, 1995; England, 1995). Since many previous studies did not include this representation of sub-grid-scale mixing,

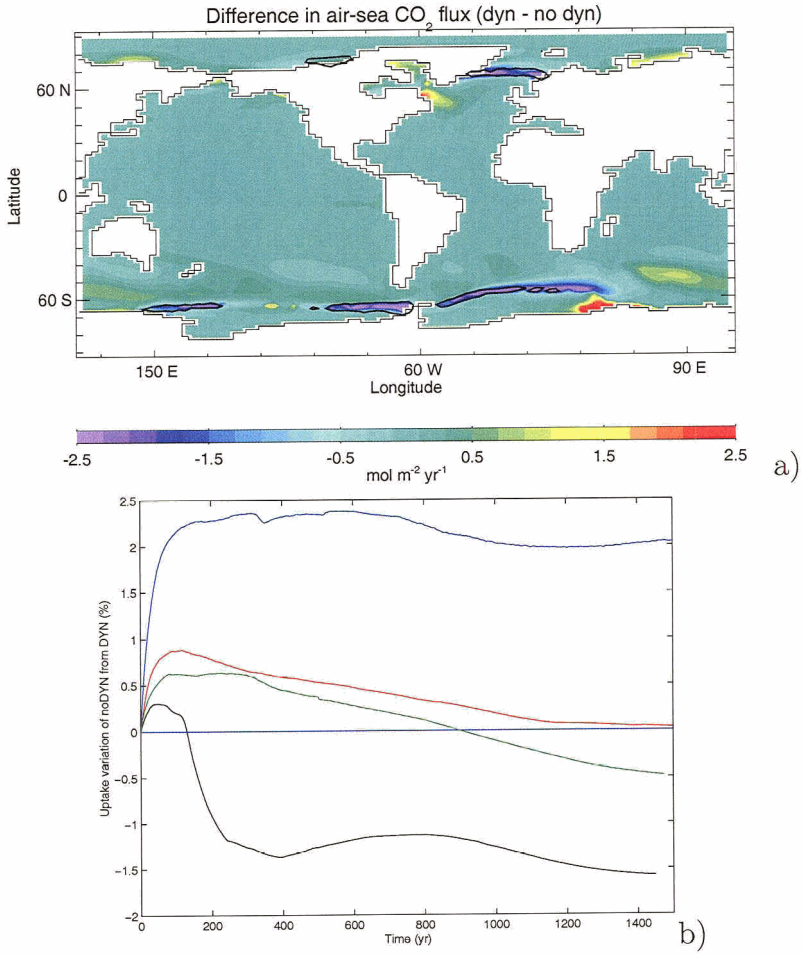

Figure 3.14: a) Air-sea flux difference (mol m^{-2} yr^{-1}) for 1008 ppmv for runs with and without sea ice dynamics (dyn minus no-dyn), both experiments include the GM parameterization for ocean mixing. The difference in the sea ice edge is outlined in black for both maps. b) Difference in the percentage of anthropogenic CO_2 uptake for the same runs. The model is prescribed with an atmospheric CO_2 concentration (Eq. 3.2) that is released at 367 ppmv (blue), 539 ppmv (red), 712 ppmv (green) and 1008 ppmv (black), corresponding to years 2000, 2050, 2075 and 2100, respectively, as in Fig. 3.5

the experiments in section 3.3.2 were repeated using the more traditional horizontal/vertical mixing scheme.

In all GM experiments, the ocean initially takes up less anthropogenic CO_2 than the corresponding cases without GM until around year 300 (Fig. 3.15c), at which point the atmospheric CO_2 concentration begins to decrease more rapidly (Fig 3.15b). By the end of the experiments (year 3450) the GM experiments all produce a lower atmospheric CO_2 concentration, as the total integrated oceanic uptake is greater. Differences with and without GM are greater than corresponding differences with and without sea ice dynamics. For example, a 6% difference in net uptake (533 ppmv for GM; 572 ppmv for no-GM) occurs in the 1008 ppmv case, whereas only a 1.5% difference occurs when sea ice dynamics are excluded (Fig. 3.15b and c). As in the sensitivity experiments of the previous subsection, however, the most significant differences occur in high latitude regions, although the magnitudes are now much higher (Fig. 3.15a). These differences are greatest in the Southern Ocean, where isopycnals tend to outcrop, with only minor differences in the high northern latitudes.

The inclusion of the GM parameterization reduces the initial 1850 overturning strength by about 6-7 Sv, and the inclusion of sea ice dynamics reduces it by a further 3 Sv (Fig. 3.16a). With the inclusion of sea ice dynamics (black curve) the overturning does not decrease over the period of specified and increasing atmospheric CO_2, although the final overturning strength is similar to the run which doesn't include sea ice dynamics (cyan curve). The global mean SST (Fig. 3.16b) shows the experiments starting with similar values at 1850 (17.5°C), increasing to maximum values within 1°C of each other and then leveling off. The change in global-mean SST does not contribute much to the variation in carbon uptake between the three experiments. Rather, circulation changes and changes in the sea ice extent, resulting both from changes in sea ice dynamics and the representation of sub-grid-scale ocean mixing, have a more significant impact. The inclusion of the GM parameterization, in particular, results in less vigorous deep mixing and ultimately increases the timescales for anthropogenic CO_2 sequestered at depth to be returned to the sea surface.

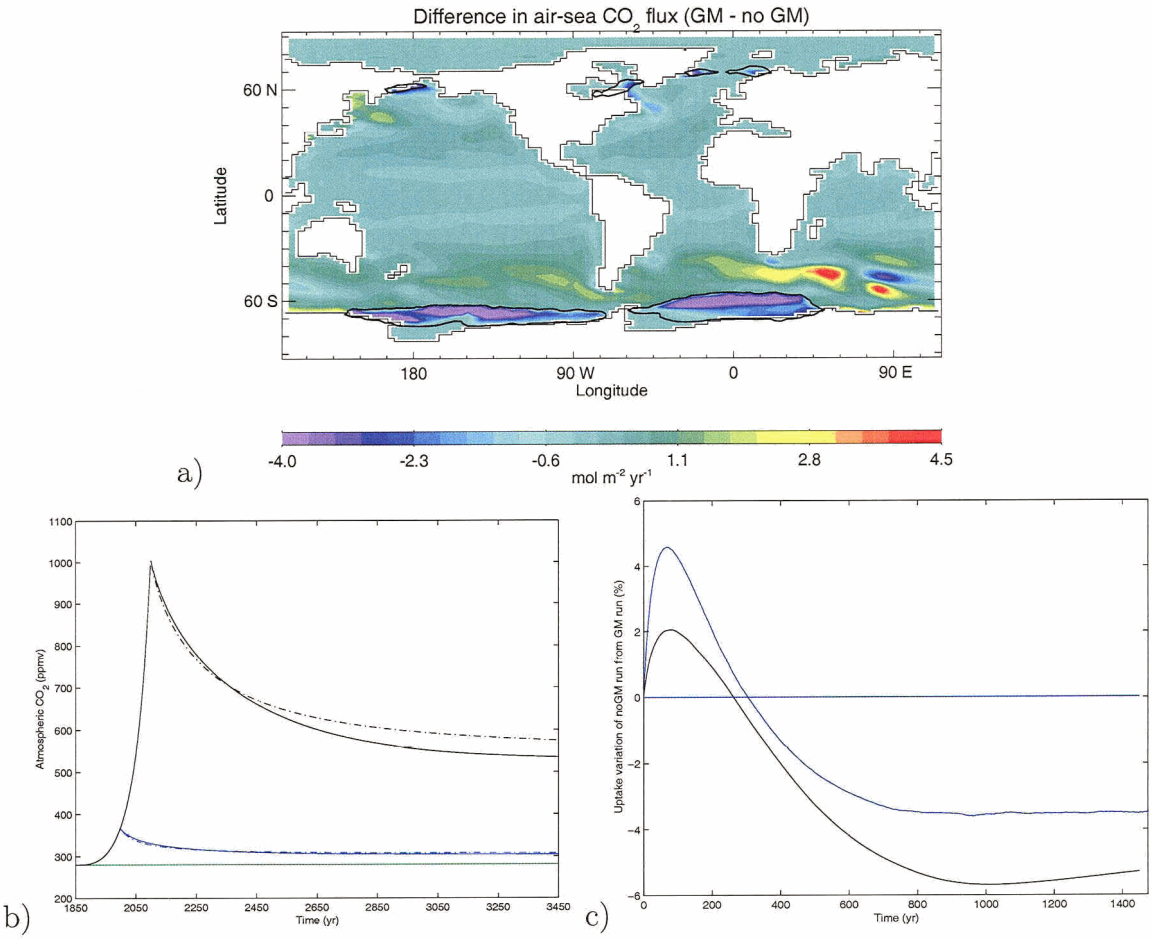

Figure 3.15: a) Air-sea flux difference (mol m^{-2} yr^{-1}) for 1008 ppmv for runs with and without the inclusion of the GM parameterization (GM minus no-GM). The difference in the sea ice edge is outlined in black for both maps. b) Atmospheric CO_2 as a function of time for the 1008 (black) and 367 (blue) ppmv experiments (as in Fig. 3.5a). The experiments do not include sea ice dynamics: with GM (solid lines, using PI_noevp_gm as initial condition); without GM (dashed lines, using PI_noevp_nogm as initial condition). The green curve is a control run with constant atmospheric CO2 = 280 ppmv, without sea ice dynamics and without the inclusion of the GM parameterization. c) Difference in the percentage of anthropogenic CO_2 uptake between the runs with and without the inclusion of the GM parameterization (no-GM minus GM), corresponding to the experiments shown in b).

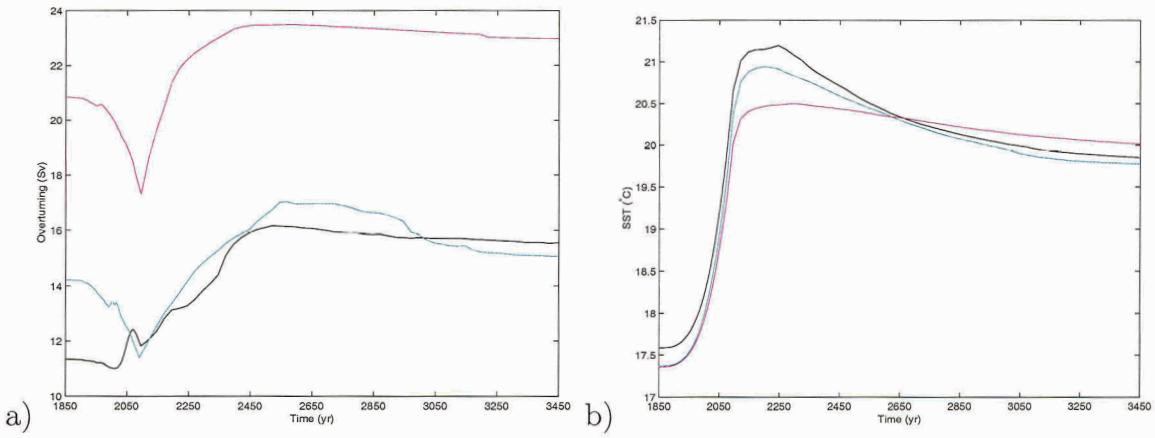

Figure 3.16: a) Maximum Atlantic overturning (Sv) and b) global- and annual-mean SSTs for 1008 ppmv runs. The curves correspond to: no-GM parameterization and no sea ice dynamics (purple); no sea ice dynamics and GM parameterization (cyan); both sea ice dynamics and GM parameterization (black).

3.4 Summary and Discussion

The dominant patterns of air-sea carbon exchange in our preindustrial equilibrium compare well with OCMIP model estimates (Sarmiento et al., 2000). Uptake occurs in regions of deep convection and downwelling, predominantly in the Southern Ocean and North Atlantic and off the south eastern coast of Africa. Net uptake also occurs, but to a lesser extent, in the North Pacific. The importance of the high latitude regions for carbon sequestration is obvious, and so is the representation of ocean mixing and sea ice processes there.

Although the inclusion of sea ice dynamics in our model makes little difference to the overall global carbon uptake in the preindustrial equilibrium experiment, there is a shift in the pattern of carbon uptake, with more uptake near the coast of Antarctica and less to the north (up to about 50°S) due to the transport of ice away from the continent. Antarctic Intermediate Water (AAIW) and Antarctic Bottom Water (AABW) formation are better represented when sea ice dynamics is included (Saenko et al., 2002). This is important since on long time scales carbon sequestration, occurring via the transport of surface waters high in CO_2 to the deeper ocean, counteracts some of the reduction in solubility arising from increasing SSTs. Saenko et al. (2002) also found that wind-driven sea ice export from the Arctic weakens and shallows the North Atlantic meridional overturning leading to a decrease in CFC uptake around 65°N. This reduction in NADW formation also explains the slight decrease in CO_2

flux we see in the North Atlantic when sea ice dynamics are included.

Our findings reaffirm the well known result that the ocean has a large buffering capacity for the projected build up of CO_2 in the atmosphere over the next several hundred years. As atmospheric CO_2 concentrations increase, the buffering capacity decreases. When the effects of climate feedbacks acting on the system are included, we find that the ocean has the ability to take up 65-75% of the anthropogenic excess remaining in the atmosphere. When we compare the effects of climate feedbacks on carbon uptake, we find that the overall effect on atmospheric CO_2 is not very large, however the ocean stores an additional 44 Pg C. Although increased SSTs reduce uptake under climate change, an increase in overturning and decrease in sea ice extent, once the forcing is removed, offset most of the solubility changes.

The inclusion of sea ice dynamics made only a small (<2%) difference in the global carbon uptake. This was not the case locally, however, as compensating changes in uptake occurred (predominantly in the Southern Ocean) through a shift in the sea ice areal extent. The sign of the difference in global uptake is opposite in the 367 and 1008 ppmv experiments, thereby suggesting that the level of future climate warming affects carbon uptake through sea ice feedbacks related to climate change. The inclusion of the Gent-McWilliams parameterization for mixing associated with mesoscale eddies had a significant impact on the oceanic uptake of carbon. Its use reduced the amount of anthropogenic CO_2 in the atmosphere after quasi-equilibrium was reached, and part of this reduction is associated with changes in the sea ice extent. This is even more significant when sea ice dynamics are included in the model. Parameterizations for both sea ice and sub-grid-scale ocean mixing thus lead to significant regional differences in model estimates of ocean carbon fluxes, especially in the high latitudes where models may overestimate CO_2 uptake (Sarmiento et al., 2000). The choice of parameterization (both sea ice and mixing) should be considered when modelling projected changes to the ocean-atmosphere carbon cycle in the future. Our analysis reaffirms the encouraging result with respect to future fossil fuel emissions that if we are able to reduce emissions in the near future, the ocean can buffer much of the anthropogenic CO_2 increase.

4 Modelling carbon cycle feedbacks during abrupt climate change

4.1 Introduction

Present-day atmospheric CO_2 concentrations continue to increase and climate model projections suggest a possibility, albeit remote, of this increase triggering an abrupt climate change event (Manabe and Stouffer, 1994; Stocker and Schmittner, 1997). Climatic variations in the past provide the opportunity to test these climate models and to improve our understanding of abrupt climate change.

Although the mechanisms which have led to abrupt climate change in the past are still not fully understood, evidence exists that variability in the thermohaline circulation (THC) was involved in the rapid transitions between cold and warm states recorded in paleoclimate archives from the last glacial period (Stocker, 2000; Clark et al., 2002b). These so-called Dansgaard-Oeschger (D-O) oscillations (Dansgaard et al., 1984; Oeschger et al., 1984) have been recorded, for example, in the stable oxygen isotope ratio ($\delta^{18}O$; a proxy for air temperature) of polar ice. In Greenland ice cores, abrupt warming events of several degrees were recorded, which took place in only a few decades or less (Grootes et al., 1993). These warming events, initiating the warm phase (interstadial) of the D-O oscillation, were followed by periods of slow cooling which were sometimes terminated by an abrupt cooling event. The sequence of events often terminates with meltwater episodes (Bond and Lotti, 1995) during the coldest phase of the D-O cycle (stadials), as evident in layers of ice-rafted debris found in marine sediments (Heinrich, 1988).

Climate model simulations have shown that freshwater input resulting from meltwater discharges can reduce the overturning strength of the THC through changes in North Atlantic Deep Water (NADW) formation (Manabe and Stouffer, 1995; Clark et al., 2002b; Schmittner et al., 2002). At the centennial timescale, a reduction in the Atlantic overturning impacts the carbon balance through diminishing the transport of inorganic carbon from the surface to the deep ocean. Changes in sea ice cover, corresponding to changes in the poleward heat transport, also effect CO_2 uptake by changing air-sea interaction in the high latitude regions. Associated changes in sea surface temperatures (SSTs), salinities (SSSs) and alkalinity further affect CO_2 solubility and uptake in both hemispheres.

Atmospheric greenhouse gas concentrations can be reconstructed from measurements of air bubbles from polar ice cores. CO_2 concentrations have been reconstructed from southern hemisphere cores, e.g., Byrd Station (West Antarctic), Dome Concordia (Dome C) and a more recent high resolution record from Taylor Dome (Stauffer et al., 1998; Indermühle et al., 2000). It is believed that Antarctic ice core records provide more reliable information about past CO_2 concentrations than Greenland ice core records as they have been less affected by acid-carbonate reactions which affect, for example, the GRIP record (Stauffer et al., 1998). In order to investigate the link between abrupt climate change in the northern and southern hemispheres, GRIP CO_2 ice core records have been synchronized to the Byrd cores using methane synchronization techniques (Stauffer et al., 1998; Blunier and Brook, 2001). These records reveal that atmospheric CO_2 concentrations have changed by up to 20 ppmv during strong D-O oscillations (Stauffer et al., 1998; Indermühle et al., 2000). During the warm interstadial phases, CO_2 concentrations were relatively low ($\sim$200 ppmv); they increased by 10-20 ppmv during the stadials. Increases in atmospheric CO_2 between 20 kyr and 70 kyr BP parallel Antarctic warming events A1 through A4 (Indermühle et al., 2000) and seem to be connected with large iceberg discharges in the North Atlantic.

Less pronounced D-O events do not seem to correspond to significant variations in atmospheric CO_2, possibly because the associated freshwater events are too short or occur in a region which does not readily affect the THC. There is also no indication of warming in the southern hemisphere being recorded in ice cores during weaker D-O events (Stocker, 2000).

Abrupt transitions have also occurred between the LGM and the Holocene as recorded in, for example, the GISP2 (Greenland) oxygen isotope records (Grootes et al., 1993). The Oldest Dryas cold period was followed by the Bølling-Allerød warm interval, in which a warming of several degrees took place over a few hundred years, bringing an end to the last glacial period. The Bølling-Allerød interstadial event (14,600 kyr BP in the GISP2 oxygen isotope record) was a rapid warming event which corresponds to the Antarctic Cold Reversal (ACR) in the Southern Ocean and a rapid increase in atmospheric CO_2 concentrations as seen in the Dome C CO_2 data (Monnin et al., 2001). Although Vostok and Taylor Dome CO_2 data are thought to be the most accurate, the temporal resolution is too low to provide a detailed record of atmospheric CO_2 data over the last glacial termination (Monnin et al., 2001). Coincident with the onset of the Bølling-Allerød was an abrupt increase in atmospheric CO_2 of about 8 ppmv in $<$300 years (Monnin et al., 2001). This interval

is also thought to have coincided with a large meltwater pulse (mwp-1A) in the Southern Ocean (Clark et al., 2002a; Weaver et al., 2003). It is thought that the Southern Ocean played a key role in abrupt transitions of atmospheric CO_2 during the last glacial termination, however the changes in the North Atlantic THC during mwp-1A probably also played a key role during that time.

Through the addition of an inorganic ocean carbon cycle model into the UVic Earth System Climate Model (ESCM — Weaver et al., 2001) we examine changes to atmospheric CO_2 concentrations during abrupt climate change events both before and after the LGM. To accomplish this, we force the model with meltwater pulses in both the North Atlantic and Southern Oceans to replicate possible meltwater events which may have occurred. We use an inorganic ocean carbon cycle to study the feedbacks of the perturbations on atmospheric CO_2 concentrations through changes to the THC and carbon solubility and compare these to the variations from the paleo record.

The outline of the rest of this chapter is as follows: in the next section an overview of the UVic ESCM version is presented. In section 4.3, the stability of the THC with the introduction of linearly varying freshwater input into the North Atlantic is examined. We then investigate the changes in the ocean-atmosphere carbon system when we introduce freshwater at varying volumes and rates equivalent to estimates from Heinrich events (MacAyeal, 1993). With the introduction of freshwater into the North Atlantic, there is a decrease in NADW formation and a reduction of carbon transported to the deep ocean. This leads to an overall reduction in uptake in the North Atlantic, and an increase in atmospheric CO_2. In subsection 4.3.1 we examine the effect of the magnitude of the freshwater perturbations on atmospheric CO_2. In sections 4.4 we examine the sensitivity of atmospheric CO_2 to freshwater events introduced into the Southern Ocean. We find that the introduction of freshwater into a region off the South American continent causes a slight increase in NADW circulation. This leads to an increase in CO_2 uptake in the region of NADW formation. Nevertheless, this increase is smaller than the decrease in uptake associated with changes in solubility in the Southern Ocean, thereby leading to an overall increase in atmospheric CO_2. In subsection 4.4.1 we examine the role of the representation of sea ice on the uptake of atmospheric CO_2 when freshwater is added and extracted from both the North Atlantic and Southern Ocean. Carbon uptake in the high latitudes is significantly affected by changes in the sea ice edge so we examine whether the choice of sea ice parameterization has a significant influence on carbon uptake under freshwater forcings. The results from experiments which include either dynamic-

thermodynamic or thermodynamic-only sea ice models are compared. In section 4.5 we examine the sensitivity of atmospheric CO_2 to freshwater perturbations when starting from different equilibria obtained using a variety of prescribed atmospheric CO_2 levels. Finally, our results are discussed and summarized in section 4.6.

4.2 Model description and initialization

The ocean component of the ESCM is a 3-dimensional ocean general circulation model (Pacanowski, 1995) with a resolution of 3.6° zonally and 1.8° meridionally. There are 19 vertical levels in the ocean which vary from 50-m thickness at the surface to 518-m at the ocean bottom. Coupled to the ocean model is a vertically-integrated energy-moisture balance model of the atmosphere with no explicit dynamics and in which atmospheric transports of moisture and energy are parameterized using Fickian diffusion. A dynamic-thermodynamic sea ice component (Bitz et al., 2001) is also employed. The inorganic carbon component is based on the Ocean Carbon Model Intercomparison Project (OCMIP) implementation (Orr et al., 1999). Detailed descriptions of each model component as well as the glacial and present-day climatology are available elsewhere (Weaver et al., 2001).

The solubility component allows atmospheric CO_2 concentrations to vary based on the integrated air-sea carbon fluxes, and assumes that the atmosphere is instantly well mixed (see Ewen et al., 2004a, for more details). This interaction between the oceanic and atmospheric CO_2 allows us to perform transient experiments determining the evolution of atmospheric CO_2. The evolving atmospheric CO_2 changes the outgoing longwave radiation in our model which allows assessment of its climatic feedback.

In this study, we are interested in the response of the inorganic carbon cycle to freshwater perturbations and have not included biological processes involved in the carbon cycle. Although this neglects potential feedbacks associated with ocean biology in response to these perturbations, the biological response to resulting changes in ocean physics is poorly understood. During meltwater events, biological productivity in high latitude regions may be affected by changes to water column stratification and sea ice extent. Iron supply is thought to limit Southern Ocean productivity and CO_2 uptake (Martin, 1990). A reduction in iron through upwelling may result in changes to CO_2 uptake where freshwater input leads to stratification changes. François et al. (1997) suggest that surface water stratification may contribute to increased CO_2 uptake in the Southern Ocean through changes in nutrient availability. Changes to sea ice extent may also impact the productivity due to light availability

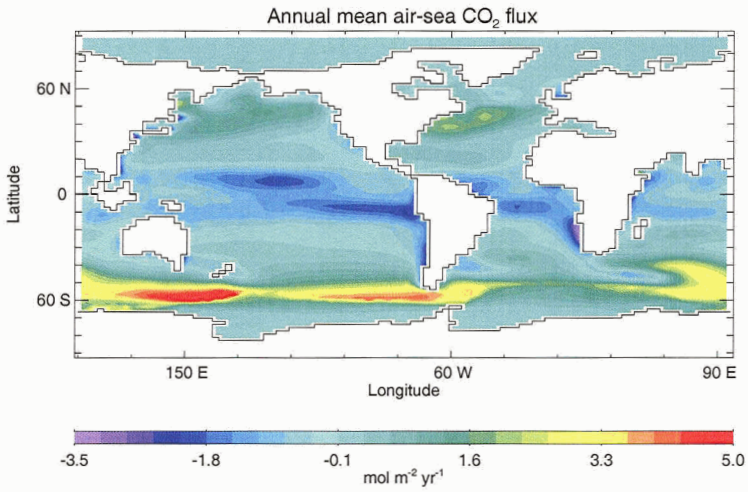

Figure 4.1: Map of annual mean air-sea CO_2 flux (mol m^{-2} yr^{-1}) for the glacial equilibrium climate. The initial condition for this experiment was an equilibrium state with a prescribed atmospheric CO_2 concentration of 200 ppmv and 21 kyr BP orbital forcing. Here a dynamic-thermodynamic representation of sea ice and the Gent and McWilliams (1990) parameterization for mixing associated with mesoscale eddies were used.

and further changes to stratification in this region. Although we will not address the biological response to meltwater episodes in our sensitivity studies, we show that significant changes to water column properties and deep water formation occur in the high latitude regions.

To begin, we start with a Last Glacial Maximum (LGM) equilibrium obtained using 21 kBP (thousand years before present) orbital parameters, an atmospheric CO_2 concentration of 200 ppmv and elevated topography based on the Peltier (1994) continental ice sheet reconstruction. The carbon flux map for this glacial equilibrium is shown in Fig. 4.1. The main features are similar in pattern to uptake in the preindustrial climate with an atmospheric CO_2 concentration of 280 ppmv (shown in Weaver et al., 2001). High fluxes of carbon out of the ocean occur in warm equatorial regions and the Southern Ocean has the highest fluxes of carbon into the ocean. Uptake in the northern hemisphere is weaker than in the preindustrial equilibrium, although there is still a significant amount of uptake in the North Atlantic.

The overturning strength in the North Atlantic has a maximum overturning of about 5 Sv, much less than present day and less than LGM overturning in Weaver

et al. (2001). The sea ice edge in the North Atlantic is further south and North Atlantic Deep Water (NADW) forms further south which, combined with a weaker overturning leads to less uptake in the North Atlantic in the LGM run. In this version of the UVic model, we incorporate an improved parameterization of mixing associated with mesoscale eddies (Gent and McWilliams, 1990) which leads to a somewhat weaker overturning (both for the LGM and the present-day) than in Weaver et al. (2001). The coefficients for both the isopycnal diffusion and isopycnal thickness diffusion coefficients are 2×10^7 cm^2 s^{-1} and the maximum slope of the isopycnals is 0.01. The fact that the LGM overturning might be weaker than inferred from LGM proxy records is inconsequential to our analysis as our LGM equilibrium simply serves as an initial starting point from which we conduct sensitivity studies. Although the response depends on the initial conditions, in the subsequent analysis, we undertake numerous perturbation experiments, including the tracing out of the hysteresis behavior of the THC. These experiments were designed to examine the response of the climate system to abrupt transitions in the THC within the context of a variety of mean climatic states (i.e., cold: atmospheric CO_2=200ppmv; warm: atmospheric CO_2=280ppmv).

4.3 Sensitivity of atmospheric CO_2 to freshwater events in the North Atlantic

D-O events 8 and 12 correspond to significant variations of atmospheric CO_2 concentrations of up to 20 ppmv as revealed in Byrd and Taylor Dome ice core records from the Antarctic (Stauffer et al., 1998; Indermühle et al., 2000). MacAyeal (1993) estimated the freshwater flux from a corresponding Heinrich event discharged into the North Atlantic to be on the order of 0.16 Sv over 250-500 years. Alternative reconstructions from ice sheet models (Marshall and Clarke, 1997) resulted in much smaller perturbations which have also been applied to modelling studies (Weaver, 1999).

Here we address the sensitivity of atmospheric CO_2 to freshwater perturbations applied to the North Atlantic. Meltwater input is introduced between between 55 and 65°N for each experiment. The volume, duration and rate of freshwater input are varied to cover potential observational based estimates of meltwater pulses (MacAyeal, 1993; Marshall and Clarke, 1997). Our initial condition, described in the previous section, has NADW formation of ~5 Sv, corresponding to a weak glacial state. The study by Marchal et al. (1998), using a zonally-averaged biogeochemical

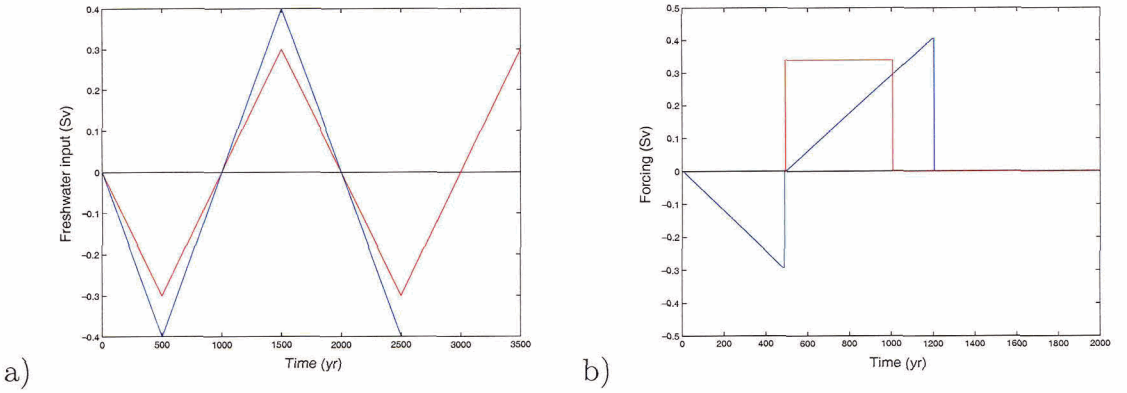

a) b)

Figure 4.2: (a) The linearly-varying freshwater forcing applied to experiments NA_hys1 (red) and NA_hys2 (blue). (b) The linearly-varying freshwater forcing applied to experiments NA1 (blue) and NA2 (red). Details of the experiments are given in Table 4.1. Positive freshwater forcing corresponds to freshwater input and negative forcing corresponds to freshwater extraction.

model, showed that when there is no active deep water formation this leads to Southern Ocean warming which affects the solubility of carbon and results in an increase in atmospheric CO_2. To our knowledge, no study to date has used a coupled ocean-atmosphere-sea ice model which includes an ocean GCM and an inorganic carbon component to assess the role of circulation on uptake as well as solubility changes.

Each North Atlantic freshwater perturbation experiment begins with an extraction of freshwater for the first 500 years that results in an increase in deep water formation. Since we begin with a non-equilibrium initial condition, the response of the atmospheric CO_2 to the meltwater pulse will likely be different than if the experiments were carried out from an equilibrium condition. Since our initial overturning is quite weak however, the response of the CO_2 likely wouldn't be very large, so we initially extract freshwater before introducing freshwater perturbations. From this state with active deep water formation, four separate experiments are then carried out. NA_hys1 and NA_hys2 (Table 4.1) have a linearly-varying rate of freshwater applied in order to assess the hysteresis behavior on the North Atlantic THC. Surface freshwater forcing increases at a linear rate of 0.6 Sv for 1000 years for NA_hys1, and 0.8 Sv for 1000 years for NA_hys2 (Fig. 4.2a).

The net freshwater forcing in NA1 and NA2 (Table 4.1) is larger than that of both NA_hys1 and NA_hys2 since NA1 and NA2 were designed to understand the response of the climate system to a hypothetical meltwater pulse event. In both NA1 and NA2, the same rate of negative freshwater forcing is applied as in NA_hys1 over

experiment	initial condition	fw forcing
NA_hys1	CO_2 = 200 ppmv	linear: ±0.6 Sv for 1000 yrs
NA_hys2	CO_2 = 200 ppmv	linear: ±0.8 Sv for 1000 yrs
NA1	CO_2 = 200 ppmv	linear: 0.42 Sv over 700 yrs
NA2	CO_2 = 200 ppmv	constant: 0.35 Sv for 500 yrs
NA.015	CO_2 = 200 ppmv	constant: 0.015 Sv for 500 yrs
NA.15	CO_2 = 200 ppmv	constant: 0.15 Sv for 500 yrs
NA.2	CO_2 = 200 ppmv	constant: 0.20 Sv for 500 yrs
NA.3	CO_2 = 200 ppmv	constant: 0.30 Sv for 500 yrs
NA.35	CO_2 = 200 ppmv	constant: 0.35 Sv for 500 yrs
NA160	CO_2 = 160 ppmv	constant: 0.35 for 500 yrs
NA200	CO_2 = 200 ppmv	constant: 0.35 for 500 yrs
NA220	CO_2 = 220 ppmv	constant: 0.35 for 500 yrs
NA260	CO_2 = 260 ppmv	constant: 0.35 for 500 yrs

Table 4.1: Summary of the North Atlantic perturbation experiments. The initial condition for each experiment was an equilibrium obtained under 21KBP orbital parameters and with the atmospheric CO_2 concentration fixed at the value given in column 2. The freshwater forcing is introduced at either a constant or linearly-varying rate (column 3).

the first 500 years. In the case of NA1, the negative freshwater forcing is then turned off (0 Sv) and a positive freshwater perturbation is added which increases at the same rate as in NA_hys1 (0.6 Sv per 1000 years) for 700 years (Fig. 4.2b). In the case of NA2, freshwater is added at a constant rate of 0.35 Sv for 500 years (Fig. 4.2b).

Figure 4.3 shows the hysteresis behavior of the THC for NA_hys1 and NA_hys2 from year 500 onward, with the corresponding timeseries of overturning strength shown in Fig. 4.4b. During the negative freshwater forcing in the first 500 years, the overturning increases to a maximum of 28 Sv in NA_hys2 and 26 Sv in NA_hys1. Between year 500 and year 1500 the overturning decreases until there is almost no deep water formation (<1 Sv). After the freshwater perturbation peaks at year 1500, the overturning remains very weak (~1 Sv) and a threshold level of freshwater extraction of about -0.1 Sv must be reached before deep water formation becomes active again (Fig. 4.3).

The corresponding overturning strength for the NA1 and NA2 experiments is shown in Fig. 4.4d. The forcing and resulting overturning for the first 500 years correspond to NA_hys1. After year 500 there is an abrupt transition between freshwater extraction and freshwater input. There is a sharp decrease in overturning when freshwater is introduced and the overturning remains weak (<1 Sv) until the freshwater perturbation is stopped after year 1000 for NA2 and year 1200 for NA1. After this

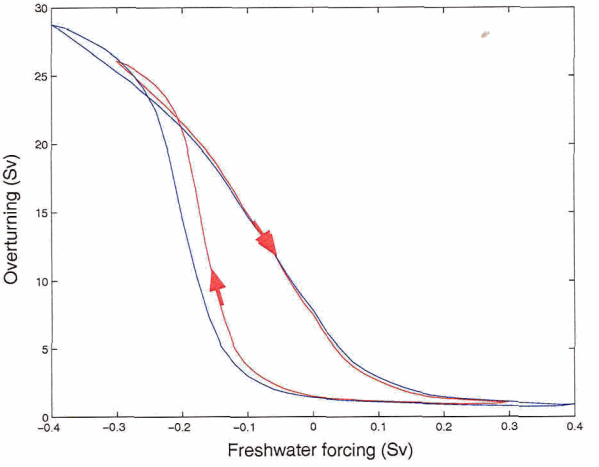

Figure 4.3: Hysteresis curves showing the change in overturning strength (Sv) corresponding to a linearly varying change in freshwater forcing (Sv) introduced into the North Atlantic. The curves correspond to experiments NA_hys1 (red) and NA_hys2 (blue), where freshwater input varies linearly at a rate of 0.6 Sv and 0.8 Sv per 1000 yrs, respectively.

point each experiment is run until year 1900 with the freshwater forcing removed. Once the forcing is removed, the overturning slowly begins to increase, although it remains less than <3 Sv and never reaches the initial overturning strength of about ~5 Sv.

In Figs. 4.4a and c the atmospheric CO_2 concentrations are shown for the NA_hys1/NA_hys2, and NA1/NA2 experiments, respectively. Starting from the state with weak (~5 Sv) NADW formation, the overturning increases as freshwater is extracted from the North Atlantic and atmospheric CO_2 oscillates about the initial value of 200 ppmv in all experiments. When freshwater is added into the North Atlantic and the overturning strength begins to decrease, CO_2 correspondingly begins to increase after year 1000 for NA_hys1 and NA_hys2, and year 500 for NA1 and NA2. For NA_hys1 and NA_hys2, the minimum in overturning strength and maximum concentration of atmospheric CO_2 occur after the maximum freshwater input (at year 1500). The subsequent linearly decreasing freshwater flux causes the overturning to initially increase slightly (Fig. 4.4b), until the critical threshold forcing (-0.1Sv — Fig. 4.3) is reached, whereupon the overturning quickly increases to 26 Sv in NA_hys1 and 28 Sv in NA_hys2, as before. A minimum in atmospheric CO_2 of about 197 ppmv is reached at about year 2300 before it increases along the same path as from 500 to 1000 years.

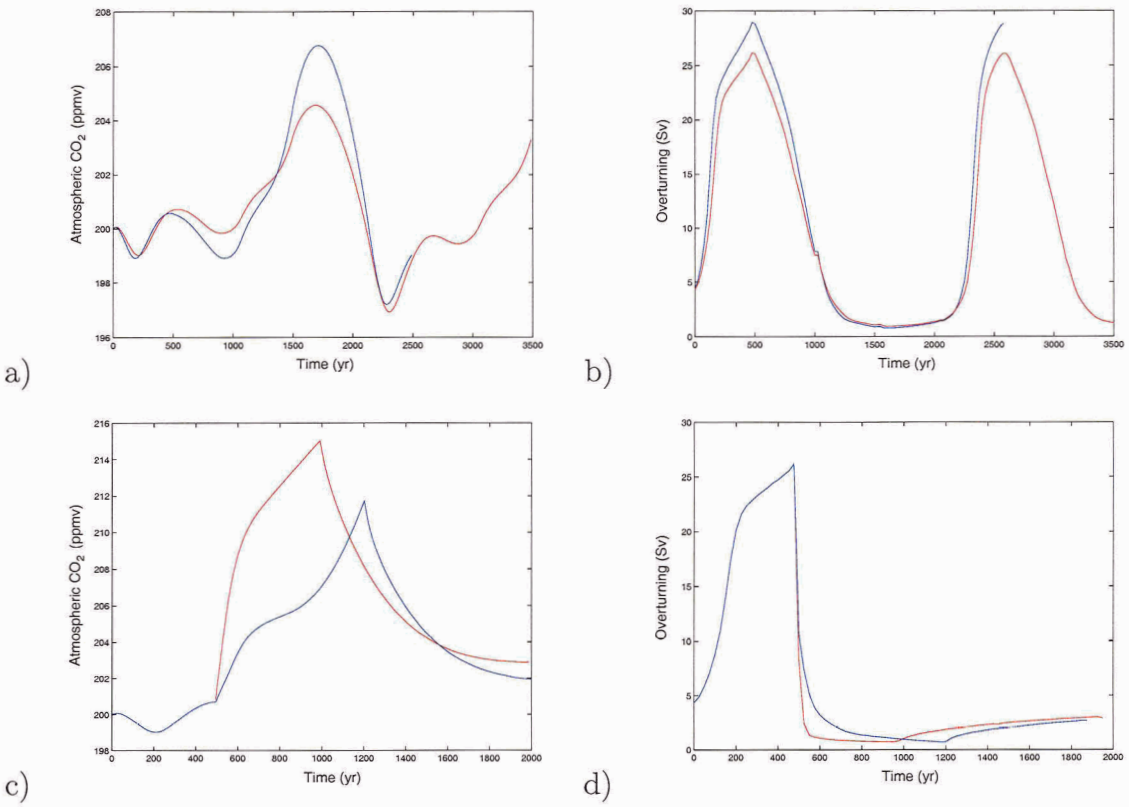

Figure 4.4: Change in atmospheric CO_2 concentration (ppmv) (a,c) and overturning strength (Sv) (b,d) for the (a,b) NA_hys1 (red) and NA_hys2 (blue) experiments and the (c,d) NA1 (blue) and NA2 (red) experiments. The linearly-varying forcing for these experiments is shown in Fig. 4.2 (a) for NA_hys1 (red) and NA_hys2 (blue) and Fig. 4.2 (b) for NA1 and NA2. The hysteresis behavior of the NA_hys1 (red) and NA_hys2 (blue) experiments is shown Fig. 4.3. Details of the experiments are given in Table 4.1.

For the NA1 and NA2 experiments, the atmospheric CO_2 begins to increase as the freshwater input causes the overturning to decrease rapidly. As one mechanism (NADW formation) which transports CO_2 from the surface to the deep ocean is turned off, CO_2 builds up in surface waters and consequently in the atmosphere. Although solubility effects will counteract these changes, there is still a significant increase in CO_2 from an equilibrium state of 200 ppmv to between 212 to 215 ppmv. Despite a similar evolution of the overturning in both experiments, there is a considerable difference in the response of atmospheric CO_2. NA2, which has a constant freshwater flux applied, shows a much steeper increase than NA1, where the freshwater flux increases linearly. This suggests that the rate of change of the freshwater forcing strongly determines the atmospheric CO_2 response through changes in solubility as the transient change in overturning strength between the experiments is similar (Fig. 4.4d). Eventually, both experiments attain similar equilibria after the forcing is removed with atmospheric CO_2 concentration differing by less than 1 ppmv.

A pronounced asymmetry is observed in all NA experiments as the increase of deep water formation during the first 500 years leads to only minor changes in atmospheric CO_2, while the reduction of the overturning after year 1000 leads to an increase of 4-8 ppmv. When freshwater is extracted again after 2000 years in experiments NA_hys1 and NA_hys2, atmospheric CO_2 begins to decrease by about 3 ppmv. The first 500 years and between years 2000 to 2500 differ in that the initial condition at year 0 is in equilibrium with an overturning circulation of about 5 Sv. The second freshwater extraction beginning at year 2000 continues from a state in which there is no deep water formation (<1 Sv). We would expect that both NA1 and NA2 would result in lower atmospheric CO_2 concentrations if there was another freshwater extraction applied after year 1200 and year 1000, respectively.

The physical mechanisms which determine the carbon flux across the air-sea interface involve both changes in circulation, in this case affecting the NADW, and solubility changes arising from changes in surface temperature, salinity and alkalinity. The rate of overturning affects the poleward heat transport, which in turn affects SSTs in the North Atlantic, and hence the uptake of CO_2 into the ocean. As the overturning strength weakens, less carbon is transported to the deep ocean and less CO_2 is taken up across the air-sea interface. On the other hand if the overturning weakens to the point where NADW stops, the southern hemisphere warms and the North Atlantic cools, which leads to large solubility changes. In the North Atlantic the reduction in uptake due to weak NADW formation is partially counteracted by increased solubility in cooler waters. In the Southern Ocean it is mostly changes

in solubility that affect CO_2 uptake, although changes in downwelling in this region affect uptake slightly as well. On the other hand, when the overturning increases we would expect atmospheric CO_2 to decrease as more of it will be transported to depths which is not yet saturated in carbon. Solubility changes can also be expected to change the uptake in the North Atlantic as the water is much more saline and SSTs increase.

Figures 4.5, 4.6 show difference maps of surface DIC and the corresponding atmosphere-ocean CO_2 flux after 500 and 1000 years for experiment NA2. After the first 500 years, zonal mean DIC shows increased concentrations in the North Atlantic corresponding to an increase in CO_2 uptake associated with an increase in NADW formation (Fig. 4.5a). There is a southward transport of this DIC at depths above 2148 m as shown by the depth-integrated DIC shown in Fig. 4.5a (and Table 4.2). The increased DIC signal reaches the surface waters around 50°S resulting in decreased uptake (Fig. 4.5b) as increased surface DIC increases the CO_2 surface partial pressure. DIC concentrations are also increased in the Southern Ocean at latitudes where Antarctic Intermediate Water (AAIW) forms. In the Southern Ocean, areas of both increased and decreased uptake occur but the deepest ocean, which is filled by Antarctic Bottom Water, is more depleted in DIC, with about 15 GtC less than the equilibrium run. Reduced ventilation of AABW is caused by the increase in sea ice cover in the Southern Ocean (Fig. 4.5c), as described in Schmittner (2003), and probably accounts for the depletion of DIC below 2148 m (Table 4.2) as less CO_2 is transported to depths. This offsets the high uptake in the North Atlantic leading to the small net atmospheric CO_2 change.

After 500 years, the North Atlantic warms by about 5.5°C. The large (compared to the equilibrium uptake shown in Fig. 4.1) increase in CO_2 uptake of about 5 mol m^{-2} yr^{-1} (Fig 4.5b) is due to a combination of changes in sea ice, heat flux and overturning in this region. Fig 4.5c shows a decrease in North Atlantic sea ice concentration, and retreat of the sea ice edge, which is very similar in pattern to the increase in CO_2 uptake. An increased CO_2 flux results from the increase in air-sea interaction in this region. Fig 4.5e shows the difference in heat flux where a negative difference in heat flux corresponds to an increase in CO_2 uptake. There is also a significant increase in the overturning (Fig 4.5b) which also contributes to an increase in uptake and is reflected in the increased DIC concentration which is transported to depth (Fig 4.5a). The Southern Ocean, on the other hand, experiences a cooling, predominantly off the western and eastern coasts of South America (Fig. 4.5d). There is an overall increase in heat flux off the eastern coast extending to the southern tip of Africa and into the

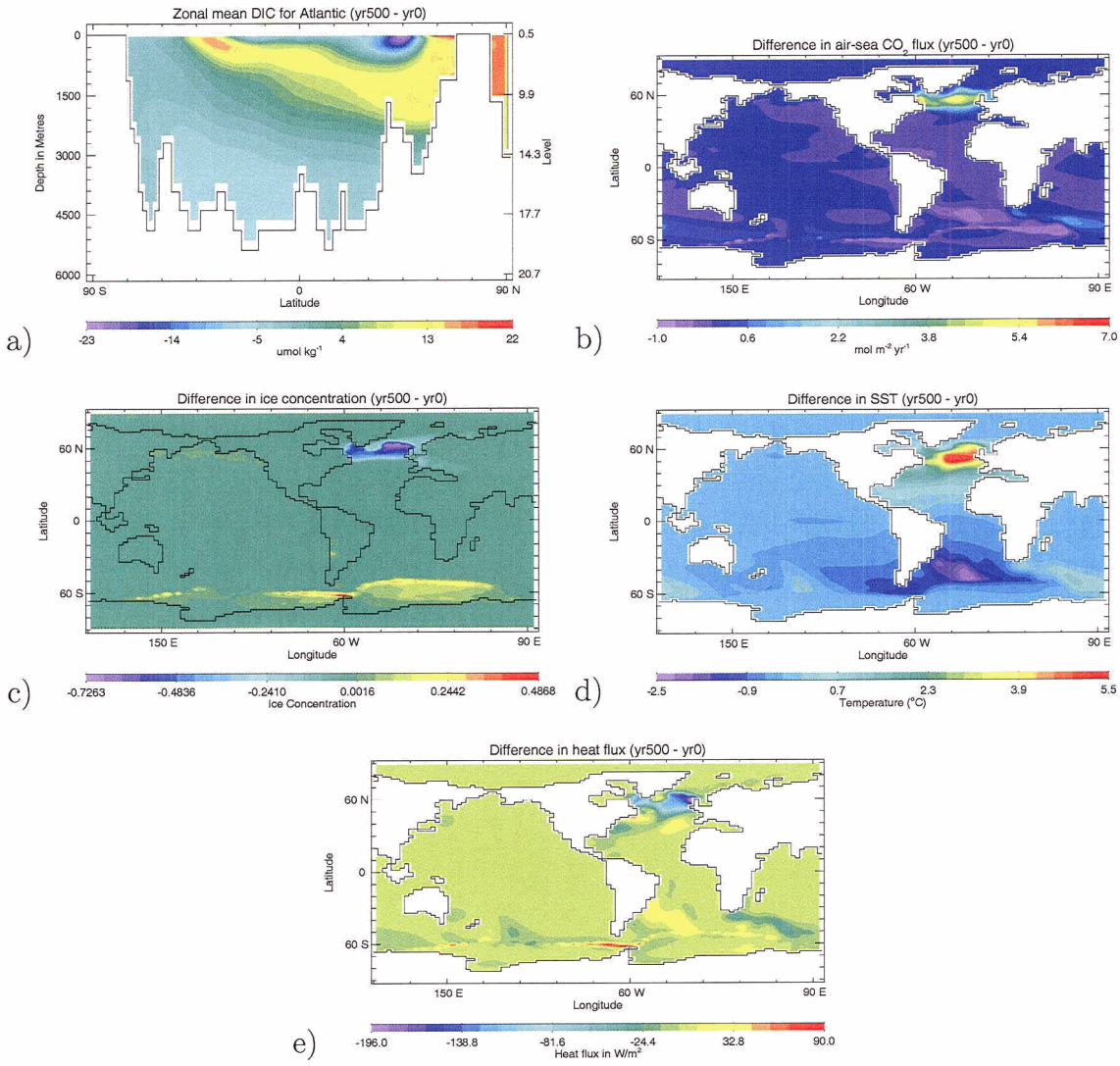

Figure 4.5: Changes obtained from experiment NA2 at year 500 relative to the LGM initial condition (year 0), after 500 years of freshwater extraction: (a) zonal mean DIC in the North Atlantic; (b) air-sea CO_2 flux; (c) sea ice concentration; (d) SST; (e) heat flux. Figure 4.6 shows similar maps for experiments at year 1000.

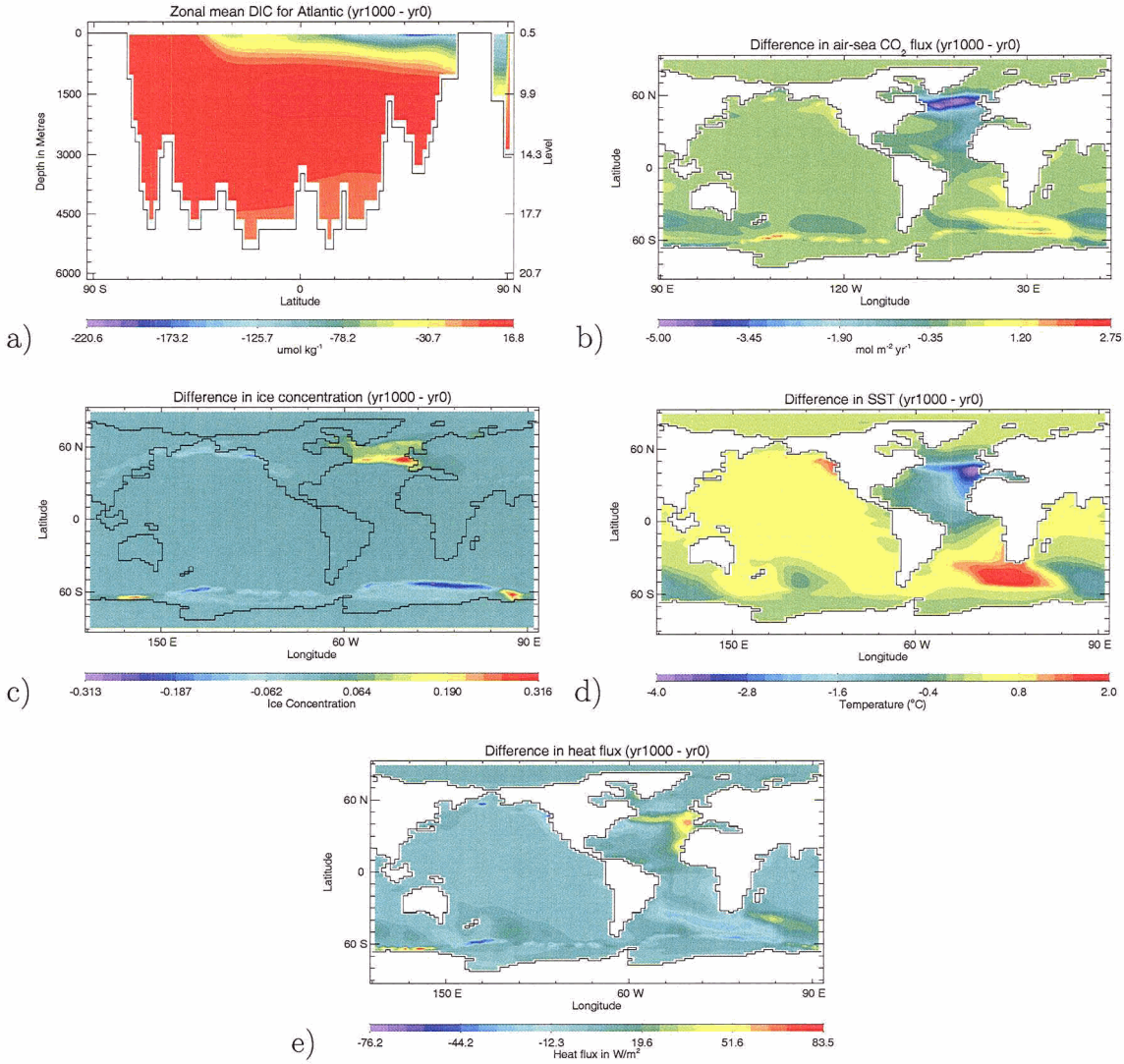

Figure 4.6: Changes obtained from experiment NA2 at year 1000 relative to the LGM initial condition (year 0): (a) zonal mean DIC in the North Atlantic; (b) air-sea CO_2 flux; (c) sea ice concentration; (d) SST; (e) heat flux. Freshwater extraction is carried out until year 500 and then a freshwater forcing is introduced until year 1000 corresponding to Fig. 4.2a.

depth (m)	yr0	yr500	yr1000
0-1257	9409	9420	9377
1257-2148	6510	6513	6512
2148-5137	14050	14035	14047

Table 4.2: Integrated global DIC (GtC) over different depths at equilibrium (yr0) and after 500 (yr500) and 1000 (yr1000) years of freshwater forcing in the North Atlantic experiment NA2.

Indian Ocean (Fig. 4.5e) with a corresponding decrease in uptake there (Fig. 4.5b). A band from about 60-45°S has increased uptake of CO_2, although further south, there is a significant expansion of the sea ice edge (by almost 10° to about 50°S) and a resulting reduction in carbon uptake.

With the addition of freshwater after year 500, the poleward heat transport begins to decrease until there is a shutdown of NADW formation and a surface temperature decrease of about 4.0°C (Fig. 4.6d). The northern hemisphere sea ice edge also moves further south (Fig. 4.6c) by almost 15° which leads to a large reduction in CO_2 uptake (Fig. 4.6b). The decrease in SSTs and increase in heat flux (Fig. 4.6e) extends from the equator into the North Atlantic where there is also an overall decrease in uptake. The reduction in overturning, and to a lesser extent the heat flux, together with the change in sea ice concentration, account for most of the changes in CO_2 flux after year 1000. Compared to the initial condition, Table 4.2 shows that there is slightly less DIC below 2148 m (about 3 GtC compared to 15 GtC at year 500) and between 1257 and 2148 there is about 2 GtC more (compared to 3 GtC more at year 500). The surface waters, however, show a significant decrease in DIC of 32 GtC (compared to a gain of 11 GtC at year 500) resulting from an alkalinity dilution and a small decrease in the overturning strength.

In the Southern Ocean there is a 2°C increase in SST (Fig. 4.6d), predominantly in the Atlantic between about 58-42°S off the south African coast. These warmer surface waters are associated with a net decrease in heat flux (into the ocean) and an increase in CO_2 flux into the ocean of almost 2 mol m^{-2} yr^{-1} (Fig. 4.6b). The net uptake, however, is negative, predominantly due to a large reduction in the North Atlantic of more than 5 mol m^{-2} yr^{-1}. This leads to an overall increase in atmospheric CO_2 of about 15 ppmv.

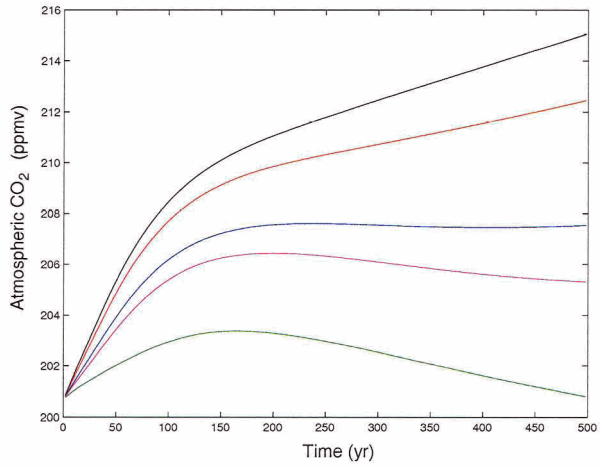

Figure 4.7: Atmospheric CO_2 concentrations for freshwater perturbations in the North Atlantic. The experiments correspond to NA.015 (green), NA.15 (pink), NA.2 (blue), NA.3 (red) and NA.35 (black) with initial conditions and forcing given in Table 4.1.

4.3.1 Effects of freshwater pulse magnitude on atmospheric CO_2

To address the effects of varying the magnitude of the freshwater perturbation on atmospheric CO_2 concentrations we apply continuous freshwater forcing at varying levels between 0.015 and 0.35 Sv. All experiments were carried out as in NA2, where a freshwater perturbation is introduced at a constant rate after year 500. The five separate experiments are referred to as NA.015, NA.15, NA.2, NA.3 and NA.35, corresponding to a freshwater perturbation of 0.015, 0.15, 0.2, 0.3 and 0.35 Sv, respectively (Table 4.1).

As might be expected, the magnitude of the freshwater perturbation has a large effect on the final atmospheric CO_2 concentration (Fig. 4.7). NA.015 yields a maximum change of only 2 ppmv after the first 150 years of freshwater input, which subsequently begins to decrease until it reaches 201 ppmv. When the volume of freshwater input is increased to 0.15 Sv over 500 years, the maximum in atmospheric CO_2 is reached after 175 years before decreasing slightly to a final value of about 205 ppmv. At a volume input of 0.2 Sv over 500 years, a maximum is reached after 175 years and then the level of atmospheric CO_2 remains relatively constant at about 207 ppmv to year 500. NA.015, NA.15 and NA.2 all have a minimum overturning strength of >1 Sv after the first 100 years of freshwater input. Both NA.35 and NA.3,

however, have minimum overturning strengths <1 Sv after the first 100 years. This reduction in overturning, to a point where NADW is no longer forming, leads to a threshold wherein atmospheric CO_2 concentrations continue to increase. In Fig. 4.7, both experiments NA.3 and NA.35 show a sharp increase in atmospheric CO_2 over the first 120 years and then CO_2 continues to increase, but at a lower rate, over the remaining 500 year period of freshwater input. After 500 years, the atmospheric CO_2 is 212 ppmv for NA.3 and 215 ppmv for NA.35. These experiments suggest that in order to have any significant increase in atmospheric CO_2 there must be a significant reduction in NADW formation (to less than 1 Sv in this case) or a strong dilution of surface waters. These experiments have also been carried out with a linear increase of freshwater input (corresponding to similar total volumes of water above) yielding a similar overturning threshold for continued positive atmospheric CO_2 accumulation to year 500.

4.4 Sensitivity of atmospheric CO_2 to freshwater events in the Southern Ocean

Recent sea-level fingerprinting (Clark et al., 2002a) has shown that the Laurentide Ice Sheet could not have been the only source of mwp-1A and that a large part probably came from the Antarctic Ice Sheet. In a modelling study, Weaver et al. (2003) show that if mwp-1A originated from the Antarctic ice sheet, rather than from the Laurentide or Fennoscandian ice sheets, an increase in NADW takes place, increasing poleward heat transport and providing an increase in temperatures to sufficiently explain the onset of the Bølling-Allerød.

Using a model version similar to Weaver et al. (2003) with initial conditions as described in the previous section and the addition of an inorganic solubility model, we introduced a meltwater pulse of the same magnitude and location in the Southern Ocean in order to study changes in atmospheric CO_2 concentrations corresponding to a meltwater pulse of southern hemisphere origin. Monnin et al. (2001) show that there were significant changes in atmospheric CO_2 concentrations during the last glacial termination as seen in Dome C CO_2 records. Corresponding to the onset of the Bølling-Allerød interval was a jump of about 8 ppmv in the record. In a study using a zonally-averaged coupled model, Marchal et al. (1998) found that the influence of Southern Ocean freshwater forcings did not significantly alter atmospheric CO_2 in their model. In our study, we find large changes in atmospheric CO_2 concentrations corresponding to freshwater forcings which may explain some of the variation seen in

the ice core record.

Freshwater inputs in the Southern Ocean were applied just north of the Antarctic circumpolar current (ACC). We chose the region at the southern tip of South America where Antarctic Intermediate Water (AAIW) forms in our model (Saenko et al., 2002). This region spans a small part of Drake passage extending into both the Atlantic and Pacific Oceans (region B in Weaver et al., 2003). An initial freshwater perturbation was applied to the North Atlantic for 200 years so that there was no active NADW formation as in Weaver et al. (2003). The end of this experiment was subsequently used as the initial condition for experiments SO1b and SO2.

Figure 4.8 shows the transient evolution of the atmospheric CO_2 concentration (Fig. 4.8a) and overturning strength (Fig. 4.8b) for three separate experiments. In SO1a and SO1b (Table 4.3) a linearly-increasing freshwater pulse was applied at a rate of 0.3 Sv per 500 years (Fig. 4.8c). In SO2 this was increased to 1 Sv per 500 years. SO1a begins from the equilibrium LGM climate, described in Section 4.2, and SO1b and SO2 use the initial conditions described above in which there is no NADW formation. In the SO1a and SO1b cases, the differences in initial conditions account exclusively for the differences in the evolution of atmospheric CO_2 concentration between year 0 and year 500 (Fig. 4.8a). In the SO1b run, there is a maximum concentration of 213 ppmv after 500 years whereas in SO1a, a maximum concentration of 208 ppmv occurs after only about 250 years. At year 500 the freshwater forcing is removed (Fig. 4.8c) and a quasi-equilibrium is reached in experiments SO1a and SO1b after 1500 years, at which point the atmospheric CO_2 concentrations converges to 203 ppmv.

The Atlantic overturning in SO1b increases from a state with no deep water formation ($<$ 1 Sv) to $\sim$3 Sv, whereas the overturning in SO1a increases slightly in the first 100 years, and then decreases and remains constant (at $\sim$4 Sv) by 500 years (Fig. 4.8b). In both SO1a and SO1b the freshwater forcing and initial atmospheric CO_2 concentrations are the same. The uptake in the North Atlantic is not significantly different between the two experiments, although small changes in the overturning may contribute slightly to the minor difference in atmospheric CO_2 (Fig. 4.8a). The largest differences in uptake, however, are due to changes related to the southern sea ice edge between the two runs. SO1b has larger ice concentrations primarily in the southern hemisphere. There is also a slight warming in the Northern Hemisphere, both through increased SSTs and surface air temperatures (SATs), which occurs mainly in the Pacific Ocean. There is a cooling in the southern hemisphere, predominantly in the region where the freshwater flux is applied, and

experiment	initial condition	forcing
SO1a	equil, CO_2 = 200 ppmv	linear: 0.3 Sv over 500 yrs
SO1b	trans, CO_2 = 200 ppmv	linear: 0.3 over 500 yrs
SO2	trans, CO_2 = 200 ppmv	linear: 1 Sv for 500 yrs
SO160	equil, CO_2 = 160 ppmv	constant: 1 Sv for 500 yrs
SO200	equil, CO_2 = 200 ppmv	constant: 1 Sv for 500 yrs
SO220	equil, CO_2 = 220 ppmv	constant: 1 Sv for 500 yrs
SO260	equil, CO_2 = 260 ppmv	constant: 1 Sv for 500 yrs
SOp_nodyn	pi-equil, CO_2 = 280 ppmv, thermo ice	constant: 1 Sv for 500 yrs
SOp_dyn	pi-equil, CO_2 = 280 ppmv	constant: 1 Sv for 500 yrs
SOn_nodyn	pi-equil, CO_2 = 280 ppmv, thermo ice	constant: -1 Sv for 500 yrs
SOn_dyn	pi-equil, CO_2 = 280 ppmv	constant: -1 Sv for 500 yrs

Table 4.3: Summary of the Southern Ocean perturbation experiments. The initial conditions correspond to either an equilibrium LGM climate (equil), an equilibrium preindustrial climate (pi-equil) or a transient LGM run (trans). Orbital parameters for the equil and trans are for 21 kyr BP and for pi-equil they are for 1850. The trans experiments were integrated from the equil initial condition with freshwater forcing introduced into the North Atlantic over 200 years so that the NADW formation is ceased. Atmospheric CO_2 concentrations are initially prescribed for the equilibrium runs and then allowed to evolve over time. All experiments were carried out with the inclusion of a dynamic-thermodynamic sea ice model except for a few cases where only a thermodynamic sea ice model was used (thermo ice). Freshwater forcing is introduced at either a constant or linear varying rate.

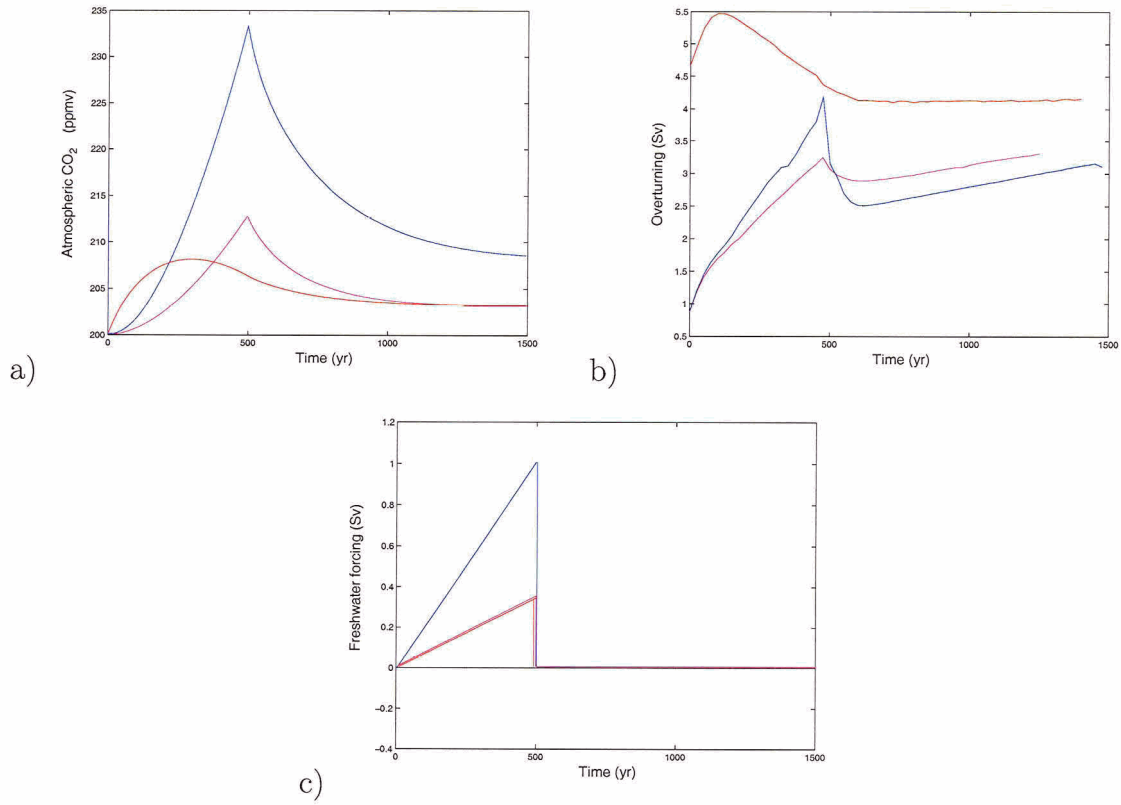

Figure 4.8: (a) Atmospheric CO_2 concentration (ppmv), and (b) overturning strength (Sv) corresponding to freshwater perturbations applied to the Antarctic Intermediate Water formation region in Southern Ocean (SO). (c) The timeseries of the freshwater forcing for each experiment with positive forcing indicating freshwater addition. The curves correspond to SO1a (red), SO1b (pink) and SO2 (blue) with forcing and initial conditions outlined in Table 4.3.

an increase in the southern sea ice edge around Antarctica, except south of Africa, where there is reduced carbon uptake of about 5 mol m^{-2} yr^{-1}.

SO2 corresponds to a more dramatic increase in atmospheric CO_2 of 33 ppmv (Fig. 4.8a). There is initially no NADW formation in SO2, although with the introduction of freshwater into the Southern Ocean, it gradually increases until it peaks just over 4 Sv (Fig. 4.8b). While a positive freshwater forcing applied to the North Atlantic causes a reduction in NADW formation, a positive forcing introduced into the Southern Ocean causes the opposite effect and the rate of NADW formation increases. An increase in NADW can happen whenever the potential density of NADW (ρ_{NADW}) is greater than the potential density of AAIW (ρ_{AAIW}), as described in Weaver et al. (2003). This can happen when either a positive freshwater perturbation is applied to

a region in the Southern Ocean or a negative perturbation is applied to a region in the North Atlantic. In SO2, the initial state has reduced NADW formation so that $\rho_{AAIW} > \rho_{NADW}$, but when we apply a positive freshwater perturbation to the region in the Southern Ocean, the potential density difference becomes, $\rho_{NADW} > \rho_{AAIW}$ and NADW formation increases.

The increase in overturning strength, however, is not very large due to the weak LGM equilibrium which has an overturning strength of around 5 Sv. After the maximum is reached, the overturning quickly reduces again once the freshwater perturbation in the Southern Ocean is removed (year 500). After a further 1000 years of integration, the atmospheric CO_2 levels reach quasi-equilibrium. Although the overturning in SO2 and SO1b is similar, the rate of freshwater input and corresponding changes in atmospheric CO_2 are quite different. The steep increase in atmospheric CO_2 in SO2 corresponds to a small increase in overturning strength in the North Atlantic.

Figure 4.9 shows difference plots for the SO2 experiment between year 500 (corresponding to the end of the Southern Ocean freshwater forcing) and year 0 (corresponding to a state in which there is no NADW formation — Fig. 4.8b). In Section 4.3 we found that a large increase in overturning (of ~20 Sv) did not lead to a significant change in overall uptake (although there was a large regional increase in the North Atlantic). Here, we apply the freshwater perturbation to the Southern Ocean and dramatic differences in uptake occur in this region. The large increase in uptake (Fig. 4.9f) in the North Atlantic is largely due to a reduction in sea ice cover (Fig. 4.9e), which in turn is a result of an increase in the northward heat transport at year 500 relative to the initial state with no NADW formation (year 0).

There is also an overall increase in SSTs across the northern hemisphere with a maximum increase of about 5°C occurring in the eastern North Atlantic Ocean and Mediterranean Sea (Fig. 4.9d). Cooling in the southern hemisphere occurs in two regions: off the South American continent; in the southern Indian Ocean where surface air temperatures are also lower by ~4°C. Decreased SSTs off the coast of South America have a corresponding heat flux signature (Fig. 4.9c) and result from the increase in heat transport away from this region into the North Atlantic. There is a net downward heat flux due to cooler SSTs and changes in ice concentration in the Southern Ocean leading to an overall reduction in carbon uptake by the ocean with an average of about 4 mol m^{-2} yr^{-1} (Fig. 4.9f).

Both SAT and SST are reduced off the southern coast of South America where the maximum decrease in uptake in this region reaches almost 20 mol m^{-2} yr^{-1}. Over-

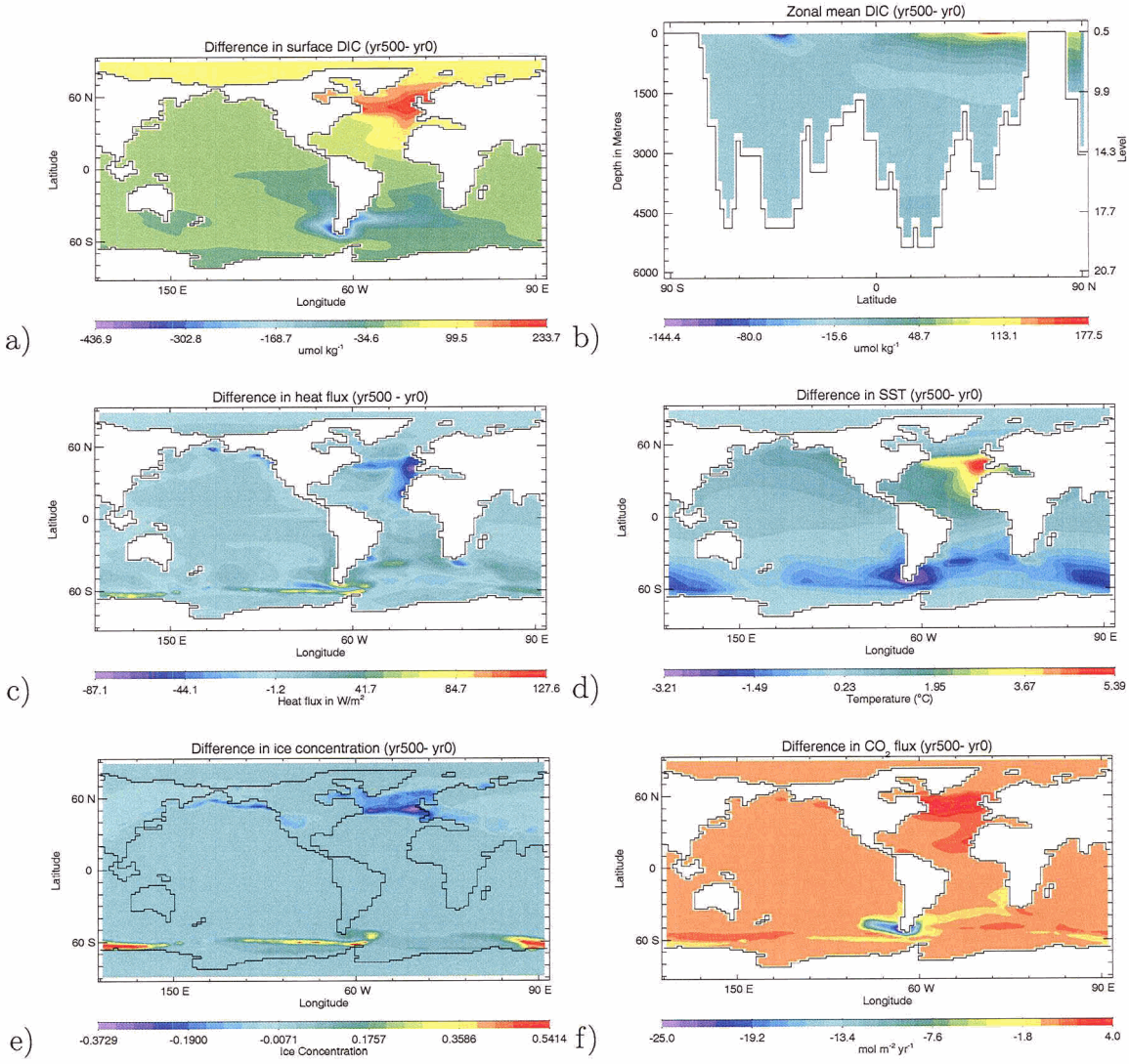

Figure 4.9: Changes obtained from experiment SO2 at year 500 relative to the initial condition (year 0): (a) surface DIC; (b) zonal mean North Atlantic DIC; (c) heat flux; (d) SST; (e) sea ice concentration; (f) air-sea CO_2 flux. Year 0 corresponds to a transient initial condition (Table 4.3) once formation of NADW is ceased, and year 500 corresponds to the end of the application of the positive freshwater perturbation to the Southern Ocean. The strength of the overturning at year 0 and year 500 and the prescribed freshwater forcing are shown in Fig. 4.8b,c.

depth (m)	yr0	yr500
0-1257	9362	9348
1257-2148	6508	6478
2148-5137	14049	14019

Table 4.4: Integrated global DIC (GtC) after 500 years of freshwater input in the Southern Ocean (yr500). Integrated DIC for the equilibrium run is shown in Table 4.2. yr0 shows values after 200 years of freshwater input into the North Atlantic corresponding to transient (trans) runs in Table 4.3.

turning in this region becomes much shallower and slightly weaker and the maximum depth of the overturning cell is reduced from about 3700 m to 2100 m. The zonal mean DIC in the Atlantic (Fig. 4.9b) shows a large decrease in the surface region of the overturning cell (between 74-63°S) and the entire deep basin has an overall negative change in the DIC concentration. The entire water column is depleted in DIC after 500 years by almost 74 GtC (Table 4.4). The surface layer to 1257 m is reduced by 15 GtC whereas the deeper layers are reduced by about 30 GtC each. Uptake off the southern coast of South America is also affected by changes in alkalinity due to dilution which leads to a much more significant local effect on the uptake than either changes in the overturning or heat flux. When globally-averaged, there is a large positive outgassing of carbon to the atmosphere which results in an increase in atmospheric CO_2 concentrations of 33 ppmv.

4.4.1 The role of sea ice on atmospheric CO_2 changes

In this section, oceanic carbon uptake obtained using a dynamic-thermodynamic sea ice model is compared to that obtained using a thermodynamic only model when freshwater perturbations (both positive and negative) are applied in the same region in the Southern Ocean. Carbon uptake in the high latitudes is significantly affected by changes in the sea ice edge. As we have seen, large changes in the sea ice edge in both hemispheres contribute to large differences in atmospheric CO_2 concentrations. Thus we need to better understand whether the choice of sea ice parameterization has a significant influence on carbon uptake under freshwater forcings, or if the changes we have seen in atmospheric CO_2 concentration are independent of the chosen parameterization. Carbon uptake in the high latitudes is significantly affected by changes in the sea ice edge so we examine whether the choice of sea ice parameterization has a significant influence on carbon uptake under freshwater forcings. The thermodynamic

sea ice model is based on Semtner (1976) and Hibler (1979) and a elastic-viscous-plastic rheology (Hunke and Dukowicz, 1997) is used to represent dynamics. Similar experiments (not shown) have also been carried out in the northern hemisphere although little variation in atmospheric CO_2 was found due to the differences in sea ice physics.

For these experiments we use, as an initial condition, a preindustrial equilibrium climate with an equilibrium CO_2 concentration of 280 ppmv and orbital parameters for the calendar year 1850. Two experiments were carried out using each representation of sea ice. Both positive and negative freshwater forcing were applied in each case in the same region as in experiment SO2 with a rate of 1 Sv for 500 years (again the same as in SO2). The runs with dynamical sea ice will be referred to as SOp_dyn (positive forcing) and SOn_dyn (negative forcing). Similarly, the runs with only thermodynamic sea ice are referred to as SOp_nodyn and SOn_nodyn (Table 4.3). Unlike SO2, a preindustrial climate was used for the initial state and freshwater was not added to initially reduce NADW formation. Since the aim of this section is to determine whether the choice of sea ice parameterization has an influence on carbon uptake under freshwater forcing, we choose a preindustrial equilibrium for our sensitivity analysis as it is computationally less expensive. The initial overturning strength for SO-dyn is 14.2 Sv and for SO-nodyn 11.5 Sv.

Figure 4.10 (b,c) shows the difference in atmospheric CO_2 and in overturning between SOp_dyn and SOp_nodyn. Both experiments driven by a positive freshwater perturbation yield slightly increasing overturning strengths in the North Atlantic over the first 100 years, and a subsequent decrease (Fig. 4.10c). The overall increase in atmospheric CO_2 is large for both runs: starting at 280 ppmv SOp_dyn increases by $\sim$48 ppmv and reaches 328 ppmv; SOp_nodyn increases by $\sim$40 ppmv. The most significant differences in CO_2 uptake occur where there are changes in the sea ice edge (Fig. 4.10a). With the inclusion of sea ice dynamics there is a lower concentration of sea ice along the Antarctic continent and in the North Atlantic, as this ice is transported equatorward by the winds. With the movement of the ice edge in both hemispheres, there is less overall uptake (up to 2.5 mol m^{-2} yr^{-1}) in SOp_dyn compared to SOp_nodyn (Fig. 4.10a). This leads to an atmospheric CO_2 increase of about 8 ppmv in SOp_dyn relative to SOp_nodyn.

When the Southern Ocean is perturbed with a similar negative freshwater flux (extraction), there is a significant increase in uptake in the Southern Ocean (Fig. 4.10d) which is also reflected in the decrease in atmospheric CO_2 (Fig. 4.10e). The overturning reduces from about 14.2 Sv in SOn_dyn and 11.5 Sv in SOn_nodyn to <1

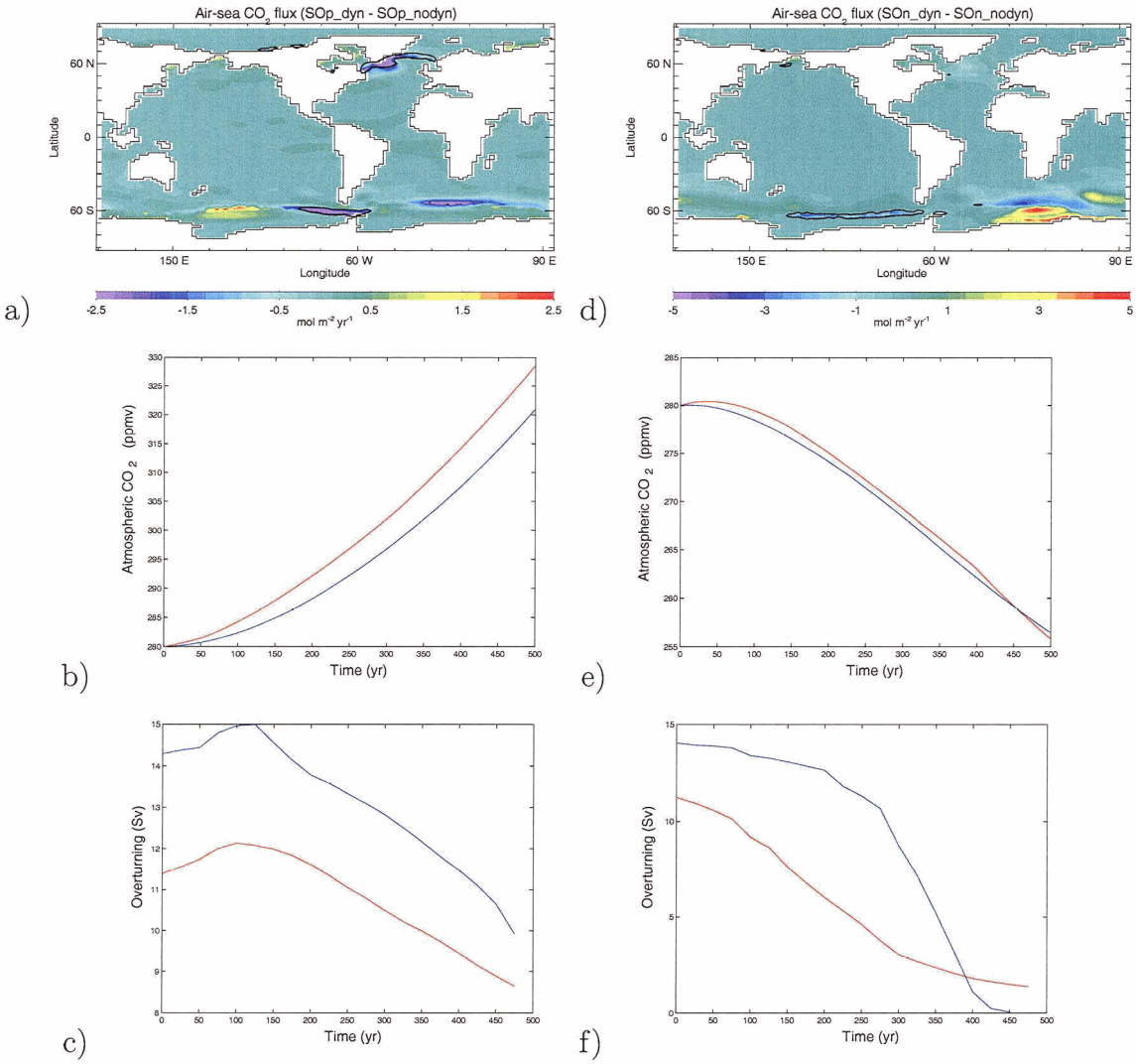

Figure 4.10: (a,d) Difference in air-sea CO_2 flux for experiments SOp and SOn with and without sea ice dynamics. The black line indicates an increase in the sea ice edge which corresponds to a decrease in uptake in these regions. (b,c) Atmospheric CO_2 concentration (ppmv) and overturning (Sv) for positive freshwater forcing (input), corresponding to experiments SOp_dyn (red) and SOp_nodyn (blue). (e,f) As in (b,c) but for a negative freshwater forcing (extraction) corresponding to SOn_dyn (red) and SOn_nodyn (blue) experiments. Initial conditions and forcing are given in Table 4.3.

Sv in each run (Fig. 4.10f), and there is an increase in Antarctic Intermediate Water (AAIW) formation. In this case the negative freshwater flux causes the potential density difference to become, $\rho_{AAIW} > \rho_{NADW}$ and formation of NADW ceases. Since AAIW formation increases, the uptake of CO_2 in this region also increases and there is an overall reduction in atmospheric CO_2 from 280 ppmv to 256 ppmv in both SOn experiments.

Differences in uptake between SOn_dyn and SOn_nodyn occur almost entirely in the Southern Ocean and are due to differences in the sea ice edge (Fig. 4.10d). There is a thin band of sea ice relocation equatorward in SOn_dyn off the western tip of South America and extending to the western side of the Ross Sea. There is a negative difference in uptake in this region of $\sim$3 mol m^{-2} yr^{-1}. Off the south African coast and along the Antarctic continent to the south there are also regions with a negative difference in uptake. This difference in uptake leads to an overall decrease in DIC in the surface layer in the Indian Ocean south of 45°S. There is also a negative difference in uptake in the North Atlantic (Fig. 4.10d) which leads to a large decrease seen in the surface DIC concentration. The uptake in the Pacific is almost the same in both runs. Overall, the atmospheric CO_2 concentration varies by less than 1 ppmv between these runs although there are significant regional differences in the air-sea CO_2 flux as well as surface DIC concentrations.

4.5 Sensitivity to initial CO_2 concentration

In this section we address the sensitivity to initial atmospheric CO_2 concentration. We carry out equilibrium runs where the atmospheric CO_2 concentration is held constant at 160, 200, 220, and 260 ppmv for 3800 years. Two sets of experiments are then carried out using these equilibrium runs: one set in which North Atlantic meltwater events are simulated (NA160, NA200, NA220 and NA260); a second set where meltwater events are introduced in the Southern Ocean (SO160, SO200, SO220 and SO260). These experiments address whether initial atmospheric CO_2 concentration affect ocean carbon uptake under freshwater forcing. This is an important question as the initial CO_2 concentration may be a determining factor in whether an abrupt change occurs or not and in the previous sections we have only address changes from an LGM equilibrium.

In the North Atlantic, freshwater is introduced into the same region as in Section 4.3 at a constant rate of 0.35 Sv over 500 years. Figure 4.11a,b shows an increase in atmospheric CO_2 for all runs over the first 500 years. The initial conditions and

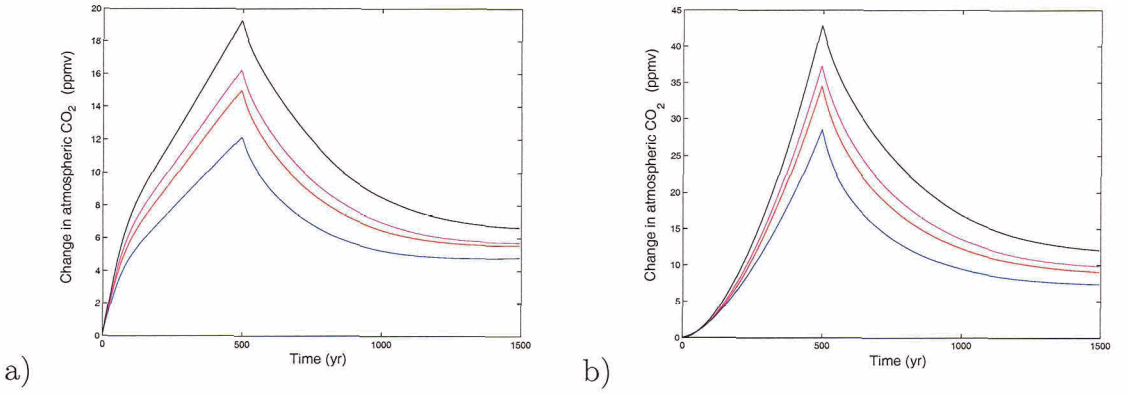

Figure 4.11: (a) Evolution of atmospheric CO_2 (ppmv) for North Atlantic freshwater perturbations. A perturbation of 0.35 Sv over a 500 year period has been applied to all curves. Equilibrium runs were carried out at four different atmospheric CO_2 concentrations (ppmv), NA160 (blue), NA200 (red), NA220 (pink) and NA260 (black) with LGM orbital parameters as outlined in Table 4.1. (b) Evolution of atmospheric CO_2 for a Southern Ocean freshwater perturbation increasing at a linear rate of 1 Sv per 500 years. Equilibrium runs correspond to SO160 (blue), SO200 (red), SO220 (pink) and SO260 (black) with initial conditions outlined in Table 4.3.

forcing for NA200 are identical to NA1 in Section 4.3 and the mechanisms which govern the reduced uptake are the same, predominantly the reduction in NADW formation leading to a reduction in carbon transport to the deep ocean. There is also less air-sea exchange due to the sea ice edge moving southward resulting in reduced uptake.

If we compare the difference between the NA260 run and the NA160 run at 500 years, there is less overall uptake in NA260 (Fig. 4.12a) and the atmospheric CO_2 concentration increases by about 19 ppmv in NA260 compared to 12 ppmv in NA160 (Fig. 4.11a), although the character of the curves is the same. Carbon uptake is affected by changes to the sea ice in the high latitude regions (Fig. 4.12c). In the Southern Ocean there is less sea ice cover in NA260 along 60°S and consequently the greater area of exposed ocean leads to more uptake in NA260 compared to NA160 (with an average of >4 mol m^{-2} yr^{-1}). In the North Atlantic, there is also reduced sea ice concentration in NA260 extending across the Atlantic, likely due to increased stratification from melting ice and a decrease in downwelling between 53° and 63°N. The result is decreased uptake in NA260 relative to NA160 with a local maximum of 5 mol m^{-2} yr^{-1}. The global ocean has a 1.6°C higher mean surface temperature in NA260 than in NA160 . This leads to a reduction in uptake due to

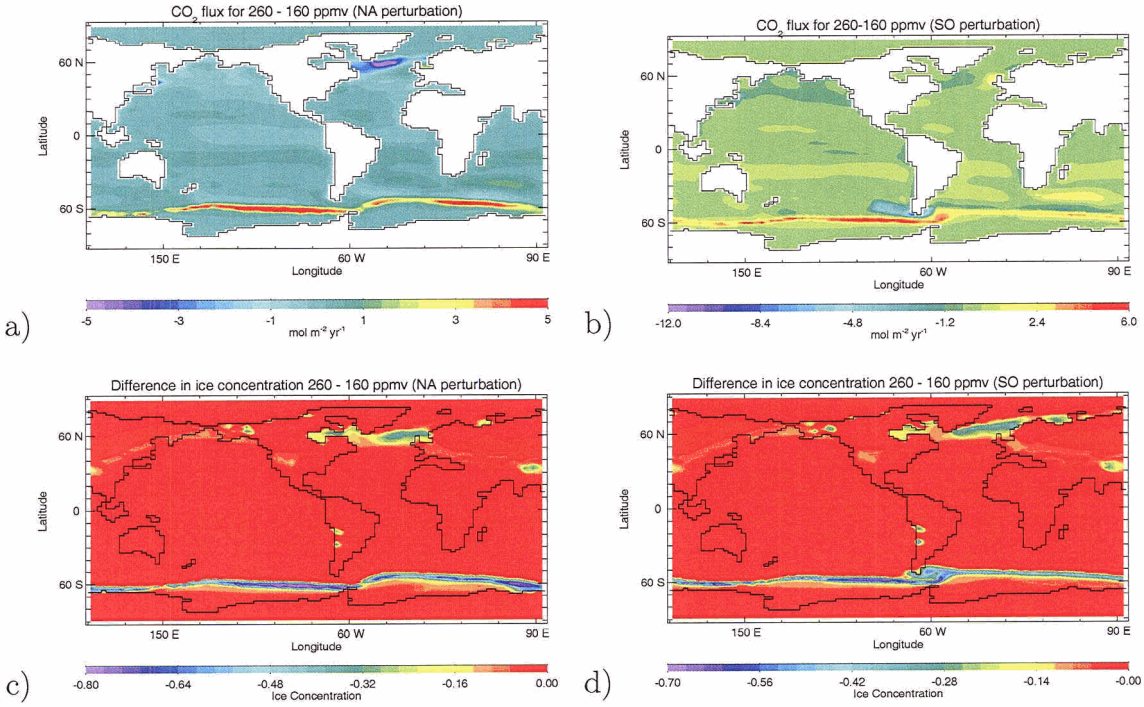

Figure 4.12: Difference in CO_2 flux (a,b) and ice concentration (c,d) between the 160 ppmv and 260 ppmv experiments for NA and SO freshwater perturbations.

solubility changes between the two runs. Although the maximum atmospheric CO_2 concentration increases are 12 and 19 ppmv for NA160 and NA260, respectively, the difference in equilibrium concentrations after the forcing is removed is only about 2 ppmv (Fig. 4.11a).

In the Southern Ocean, we introduced the freshwater perturbation into the same region as in Section 4.4 at a rate of 1 Sv for 500 years. The overturning strength varied little between experiments and over the 500 years of freshwater input, the overturning increased only by about 1-2 Sv overall. Of the four experiments (Table 4.3), the SO260 experiment shows the largest increase in atmospheric CO_2 ($\sim$43 ppmv) and the SO160 experiment the least ($\sim$28 ppmv). The largest difference in uptake between the two runs occurs in the Southern Ocean, where there is reduced sea ice concentration (Fig. 4.12b,d). In the North Atlantic the ice edge has also retreated but this only leads to a small difference in uptake. Although difference plots for both the NA and SO perturbation experiments show similar changes to sea ice cover in the North Atlantic, the North Atlantic perturbations show a much more dramatic decrease in carbon uptake in this region. When freshwater is put into the Southern Ocean, there is a slight increase in the production of deep water formation in the North Atlantic. On the other hand, when freshwater is put into the North Atlantic, there is a reduction in deep water formation. This difference leads to small changes in the amount of carbon which is transported to the deep ocean, which in turn affects the carbon flux in this region. There are also decreases in solubility due to warmer tropical and subtropical regions. Together the decreased deep water formation and solubility counteract the increase in uptake that would otherwise occur with a retreating sea ice edge.

The magnitude of the sea ice differences (and corresponding uptake differences) are much larger in the Southern Ocean, however (Figs 4.12b,d). In SO160 Drake passage is ice covered from Antarctica to South America, whereas in SO260 this ice has retreated thereby leaving a larger ice free region for uptake across Drake passage as well as along the retreated ice edge near the Antarctic continent (Fig. 4.12d). Slightly north of the region of high uptake is a region of outgassing where there is a net freshwater flux to the ocean from the melting ice off the eastern coast of South America and a corresponding decrease in uptake occurs here of up to 5 mol m^{-2} yr^{-1} (Fig. 4.12b). There is also reduced uptake between the experiments off the western South American coast associated with differences in solubility arising from increased SSTs and SSSs in SO260 over SO160. SO260 has a global mean SST of 1.5°C more than SO160 leading to an overall reduction in uptake due to solubility. Additional differences exist due to differences in the circulation and downwelling associated with

a closed Drake passage, further reducing the difference in uptake. Taken together, these results demonstrate that changes in sea ice significantly affect CO_2 uptake locally, predominantly in the Southern Ocean. Overall however, atmospheric CO_2 concentrations increase in all perturbation runs with the largest changes in NA260 and SO260 runs. This indicates that global solubility changes, due to increased SSTs, play a significant role in determining the final atmospheric CO_2 concentrations.

4.6 Summary and Discussion

In this chapter we have investigated the response of the inorganic carbon cycle to simulated - under LGM radiative forcing - meltwater pulses in both northern and southern hemispheres. In particular we have shown that atmospheric CO_2 concentrations increase by about 14 ppmv when a freshwater pulse equivalent in amount to a Heinrich event is added to the North Atlantic. These changes in CO_2 are a response to changes in solubility partly due to dilution effects on alkalinity, reduced formation of NADW and associated changes in sea ice extent. The increase in atmospheric CO_2 is approximately what is seen during strong D-O oscillations, when atmospheric CO_2 increases between 15-20 ppmv, coincident with Antarctic warming events A1 and A4 (Stauffer et al., 1998). These changes seem to be a response to large meltwater events in the North Atlantic.

We also showed that meltwater perturbations added to the Southern Ocean lead to significant changes in atmospheric CO_2. By introducing a volume of freshwater corresponding to meltwater pulse 1A, we found an increase in atmospheric CO_2 of 32 ppmv. This increase is significantly greater than that found in the Dome C record concurrent with mwp-1A — 8 ppmv (Monnin et al., 2001).

The sensitivity of carbon uptake to the representation of sea ice in our model was also studied. We found slight differences in the net carbon uptake between experiments using a dynamic-thermodynamic sea ice model and those using only a thermodynamic model when positive freshwater perturbations were applied to both the Southern Ocean and the North Atlantic. When a negative freshwater forcing was applied, however, there was little variation and the inclusion of sea ice dynamics did not contribute significantly to the difference in overall atmospheric CO_2 concentrations, although the regional differences in uptake lead to differences in the surface distribution of DIC.

Further sensitivity studies showed that the initial amount of atmospheric CO_2 has an effect on the total amount of carbon that is taken up by the ocean. Increased

warming due to increased CO_2 in the atmosphere leads to significant differences in solubility and sea ice cover, predominantly in the Southern Ocean, which results in less uptake when starting from an equilibrium with a higher initial CO_2 concentration. We also found that the atmosphere-ocean carbon system establishes a new equilibrium when the forcing is removed in all cases.

Taken together these experiments show that if meltwater events are introduced into either hemisphere, they lead to changes in circulation and solubility which affect the air-sea carbon flux and atmospheric CO_2 concentrations. It was shown that solubility changes alone do not account for all of the changes in atmospheric CO_2, and that changes in carbon uptake by the oceans associated with both climatic and circulation changes are especially important to consider if we want to understand abrupt climate change. The changes that we see in atmospheric CO_2 using an oceanic solubility model are sufficient to explain changes of 15-20 ppmv associated with meltwater input into the North Atlantic.

5 Sensitivity of CO_2 uptake to glacial-interglacial forcing

5.1 Introduction

Ice core records from Antarctica reveal that glacial atmospheric CO_2 concentrations were about 80 ppmv lower than preindustrial levels. It is unknown what mechanisms led to the glacial-interglacial atmospheric CO_2 cycles and whether atmospheric CO_2 changes acted as a primary driver or merely an amplifier of the glacial cycles. Planetary perturbations cause changes in the geographical receipt of solar insolation (Berger, 1978) although they do not provide a sufficient explanation for the large amplitude changes recorded in the ice cores. It is thought that they may act as a primary trigger with climatic feedbacks amplifying these changes to produced glacial cycles. The observation that the CO_2 concentration seems bounded and there is a regularity in the variations may imply that a few dominant mechanisms are responsible for the glacial cycles.

The biological carbon cycle is thought to play an integral role in glacial cycles (for a review see Sigman and Boyle (2000)). However changes in atmospheric CO_2 concentrations resulting from physical processes are potentially just as important and have been poorly studied. Several box model studies have recently examined this problem. Toggweiler (1999) showed that changes in high latitude vertical ventilation and increased stratification accounted for an 80 ppmv difference in atmospheric CO_2 concentrations, without changes in biological production or nutrient chemistry. By increasing sea ice cover in the Southern Ocean, thereby decreasing air-sea gas exchange, Stephens and Keeling (2000) were able to explain a change of $\sim$67 ppmv in their box model. Gildor and Tziperman (2002) showed that both variations in vertical mixing and sea ice cover in the Southern Ocean led to a change in atmospheric CO_2 of $\sim$75 ppmv. This change resulted mainly from reduced vertical mixing in the Southern Ocean leading to less upwelling of CO_2 rich waters and less outgassing to the atmosphere, resulting in lower atmospheric CO_2 concentrations. Using a model version similar to ours, Schmittner (2003) showed that an increase in sea ice cover over the Southern Ocean reduces ventilation and radiocarbon storage in the deep ocean. With reduced air-sea gas exchange, radiocarbon ages in the Southern Ocean were found to increase by 100 years, consistent with reconstructions of bottom water

properties. Large differences exist however with respect to air-sea partitioning of CO_2 due to solubility effects and organic cycling between box models and general circulation models (GCMs) (Gildor and Tziperman, 2002). GCMs do not show box model sensitivity to high latitude changes in sea ice and stratification and pCO_2 is controlled in a more distributed way. Archer et al. (2003) suggests that until the high latitude sensitivity of the real ocean is better understood and represented in models, Southern Ocean theories should be approached with skepticism.

In this study, we address the sensitivity of the inorganic carbon cycle to changes in orbital and CO_2 radiative forcing. In order to understand the effects of different model parameterization on CO_2 uptake, we perform three sets of experiments in which both sea ice and mixing parameterizations are varied. We further analyze the extent to which physical processes such as ocean circulation and sea ice extent govern changes in atmospheric CO_2. A coupled ocean-atmosphere-sea ice model, which has been shown to reproduce an LGM climate well (Weaver et al., 1998, 2001), and an inorganic ocean carbon cycle based on OCMIP protocol (Orr et al., 1999) are used for this study. A more detailed description of each model component is given in Chapter 2.

Using a similar model version, the inclusion of wind driven sea ice was shown to improve CFC tracer distributions in the Southern Ocean (Saenko et al., 2002). Robitaille and Weaver (1995) showed that the inclusion of the Gent McWilliams parameterization (Gent and McWilliams, 1990) also improved the distribution of CFCs due to a reduction in uptake in the Southern Ocean over the standard horizontal-vertical sub-grid-scale mixing. In Chapter 4, we have also shown that both sea ice and mixing parameterizations affect regional CO_2 fluxes, particularly in the Southern Ocean, and resulting atmospheric CO_2 concentrations in present day model simulation. More importantly, we showed that neglecting an important physical process (dynamic sea ice) has an effect on ocean carbon uptake. In the following section CO_2 uptake under LGM forcing is discussed and the differences between model parameterizations are outlined. In Section 5.3, the sensitivity to changes in radiative forcing (both orbital and CO_2) is examined with each model parameterization, and in Section 5.3.1 we examine the sensitivity of atmospheric CO_2 to each boundary condition. In Section 5.3.2 we further investigate changes in sea ice cover and overturning on corresponding CO_2 fluxes followed by discussion and conclusions in Section 5.4.

5.2 CO_2 uptake under LGM forcing

In this section we analyze the LGM equilibrium, from which we begin our perturbation experiments in the following sections, in order to determine differences between mixing and sea ice parameterization. We also examine CO_2 uptake in the context of our LGM equilibrium climate for each parameterization used throughout the remainder of this chapter. In order to simulate an LGM climate, each run has been forced with an atmospheric CO_2 concentration of 200 ppmv and orbital parameters for 21 kyr BP (thousands of years before present - hereafter written as kBP). We have not however included a dynamical continental ice model in these experiments (as used in Yoshimori et al., 2001) although continental land ice is prescribed according to (Peltier, 1994). We have carried out three separate equilibrium experiments: LGM_evp_gm includes both sea ice dynamics and GM mixing parameterization, LGM_noevp_gm includes thermodynamic sea ice and GM mixing, and LGM_noevp_nogm includes thermodynamic sea ice and standard horizontal/vertical diffusion. For each experiment the parameterizations for both sea ice and mixing as well as boundary conditions are outlined in Table 5.1. These boundary conditions are the same for PMIP model reconstructions of LGM climate; discussion of our LGM climate can be found in Weaver et al. (2001).

Figure 5.1 shows CO_2 flux maps for all three equilibrium experiments and difference maps of CO_2 flux for both the sea ice and mixing parameterization used under an LGM climate. The general patterns of uptake are similar to the flux maps for preindustrial CO_2 with high uptake (positive values) in the high latitude regions and outgassing in the warmer equatorial regions (negative values). There are large magnitude flux differences between the parameterizations for both sea ice and mixing however. The inclusion of sea ice dynamics (a) shows greater equatorward extent of sea ice in the North Atlantic over the thermodynamic only model (b) which leads to a large negative difference in uptake (c). The North Atlantic extent of sea ice in our present day equilibrium, which includes wind driven sea ice, is too far equatorward however - and probably also the case here; although the strength of the overturning circulation for the LGM (Table 5.1) seems reasonable when compared to estimates. In the Southern Ocean there is also greater sea ice coverage equatorward which leads to a negative difference in uptake of up to 3.5 mol m^{-2} yr^{-1} shown in the difference map. The difference in sea ice cover is outlined in black (c). In most of the Pacific Ocean there is no difference in CO_2 uptake. One notable feature occurs off the southern tip of Africa where there is a large negative difference in uptake. This occurs

experiment	sea ice and mixing parameterization	boundary conditions	MO (Sv)	DIC (Pg C)
LGM_evp_gm	ice dynamics GM	CO_2 = 200 orb = lgm/21kBP	5	29969
LGM_noevp_gm	thermo ice GM	CO_2 = 200 orb = lgm/21kBP	11	30234
LGM_noevp_nogm	thermo ice horizontal/vertical	CO_2 = 200, orb = lgm/21kBP	21	30112

Table 5.1: LGM equilibrium experiments. Mixing parameterization used are either Gent McWilliams (GM) or standard horizontal/vertical diffusion. Sea ice is either wind driven (ice dynamics) or thermodynamic only (thermo ice). Boundary conditions for each experiment are for an LGM climate and are run to equilibrium with an atmospheric CO_2 concentration of 200 ppmv and orbital parameters for 21 kBP (orb). Meridional overturning (MO) strength in the Atlantic is weaker with the inclusion of both sea ice dynamics and GM mixing. Ocean carbon inventory (DIC) at equilibrium is also shown (Pg C). Note that these values are unrealistically low (as is our preindustrial carbon distribution) due to the lack of ocean biology and carbonate pumps in our model. This results in a low vertical gradient of DIC, with surface DIC concentrations not much larger than those at depth, and unrealistically low carbon storage at depth.

due to the difference in both sea ice cover and heat flux between the models in this region.

The difference in heat flux results in large CO_2 flux differences. When there is a positive heat flux into the ocean, the ocean gains heat, which results in decreased CO_2 solubility in the surface layer. Similarly when there is a loss of heat to the atmosphere, the surface layer of the ocean can then take up more carbon and there is a positive flux of CO_2 into the ocean. The heat flux off the coast of southern Africa in the LGM_evp_gm model is negative, although it is less negative than that in LGM_noevp_gm which results in an overall positive difference. This is also true in the North Atlantic where sea ice cover in the LGM_evp_gm model extends further equatorward and there is heat being lost by the ocean (negative) although less heat is lost than in the LGM_noevp_gm which has less equatorward sea ice cover resulting in a positive heat flux here. Sea ice provides an insulating barrier on the ocean surface and an increased albedo helps to reflect radiation that might otherwise penetrate the upper layer of the ocean. When there is a net flux of heat downwards, the presence of sea ice will reduce the heat flux due to an increase in the albedo. When the net heat flux is upwards however, the resulting heat flux will increase due to the increased

albedo of the sea ice. Altogether, the LGM_evp_gm model has a global ocean carbon inventory of 265 Pg C less than LGM_noevp_gm. The global carbon inventory for each model as well as overturning strength is shown in Table 5.1. Note that these global carbon inventories do not reflect realistic LGM inventories, due to the lack of a biological carbon model, and are shown simply to compare the difference in deep ocean inorganic carbon storage between the models. Although the meridional overturning is also reduced in the LGM_evp_gm model ($\sim$5 Sv as compared to $\sim$11 Sv in LGM_noevp_gm), the negative difference in uptake between the models is due to the difference in sea ice cover.

The inclusion of GM and isopycnal mixing parameterizations provides a more realistic representation of sub-grid scale mixing along isopycnals while accounting for isopycnal thickness diffusion. This tends to reduce unrealistic convective plumes and excessive communication between the top and bottom of the ocean since standard horizonal/vertical diffusion tends to have unrealistically high diapycnal diffusion in regions where isopycnals slope steeply. In this version of the UVic model the inclusion of GM tends to reduce the strength of the meridional overturning from $\sim$21 Sv (LGM_noevp_nogm) to $\sim$11 Sv (LGM_noevp_gm) and thus the meridional heat transport (Table 5.1). An overturning strength of $\sim$21 Sv is perhaps unrealistically high for an LGM climate however (Weaver et al., 2001). The inclusion of the Gent McWilliams parameterization over standard horizontal/vertical diffusion shows the most dramatic differences in CO_2 flux in the Southern Ocean (Fig 5.1e). The differences in the ice edge lead to differences in CO_2 uptake and the inclusion of GM leads to less uptake in both the North Atlantic, North Pacific and Southern Oceans due to less air-sea interaction. Slightly south of the sea ice edge there is more uptake in the LGM_noevp_gm model as the base of the NADW layer is shallower and doesn't penetrate as far northward.

Altogether the total ocean carbon inventory is less with the inclusion of GM by about 112 Pg C (Table 5.1). One notable feature is the large positive difference in uptake in the south Atlantic, extending south of Africa and into the Indian Ocean, where LGM_noevp_nogm has less uptake ($\sim$2 mol m^{-2} yr^{-1}). In the Southern Ocean isopycnals surfaces outcrop further south in the GM experiment. Since uptake of carbon in the Southern Ocean occurs where isopycnal surfaces outcrop and it is transported along isopycnals to the subtropical convergence where most is stored (between 30 and 40°S) (see for e.g. Caldeira and Duffy, 2000), CO_2 uptake is probably more realistic with the inclusion of GM.

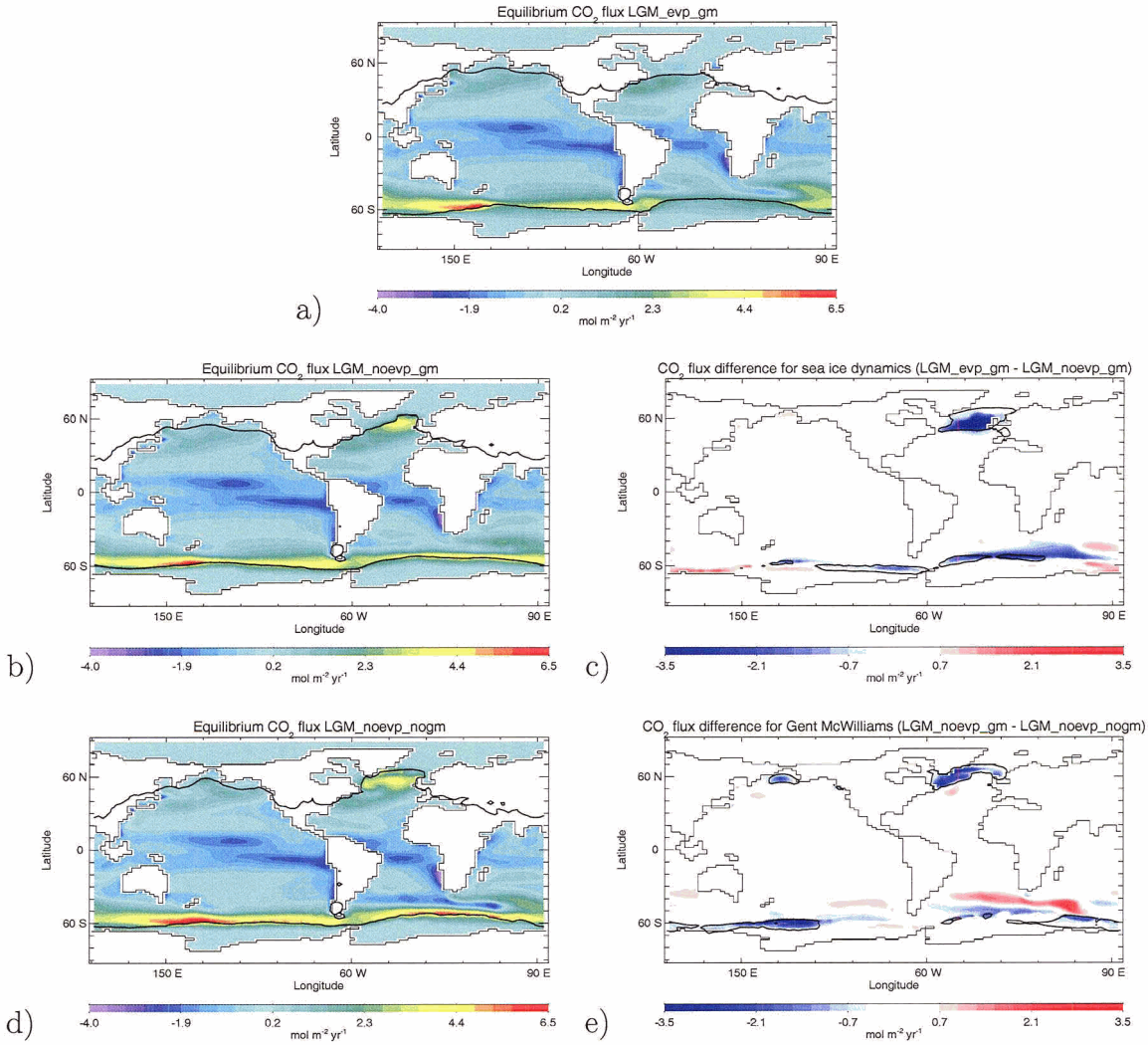

Figure 5.1: LGM equilibrium CO_2 fluxes for each model parameterization (outlined in Table 5.1). Difference maps for parameterization of both sea ice and sub-grid-scale ocean mixing are shown. The sea ice and snow line edge is outlined in black.

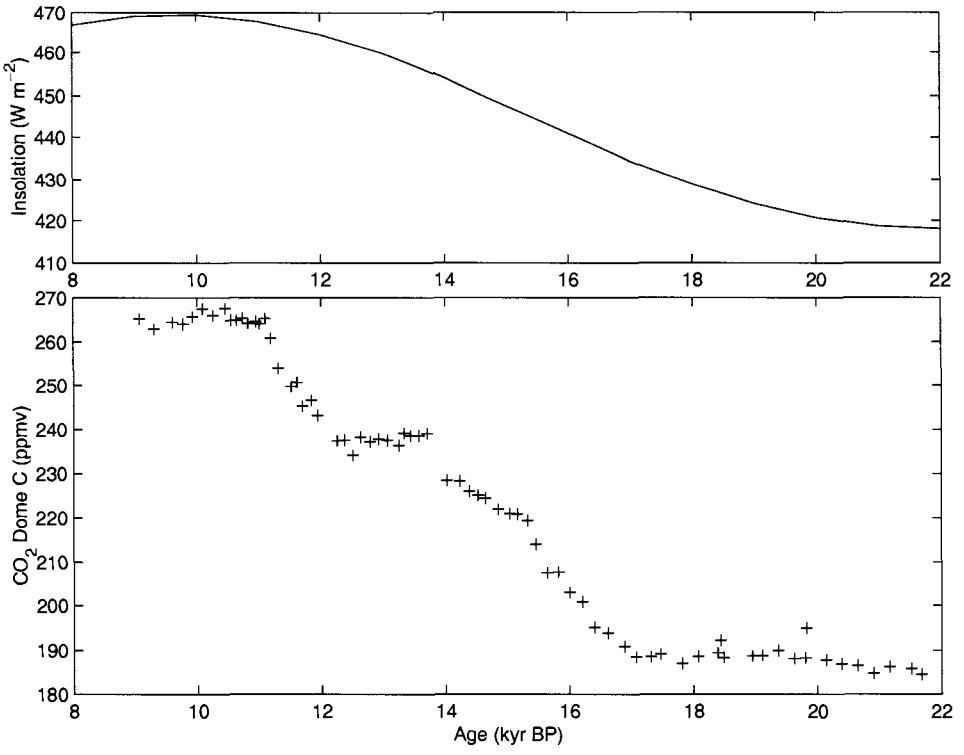

Figure 5.2: Dome Concordia (Dome C) CO_2 data taken from Monnin et al. (2001) and insolation in July at 65°N (Berger, 1978) over the last deglaciation. The maximum insolation occurs between 9 and 10 kBP.

5.3 Sensitivity of CO_2 uptake to changes in radiative forcing

In this section we address the sensitivity of our LGM equilibrium climate to 8 kBP boundary conditions, namely, orbital parameters for 8 kBP and radiative forcing corresponding to a CO_2 concentration of 280 ppmv. These boundary conditions are applied to the LGM equilibrium runs described in the previous section, and atmospheric CO_2 is allowed to evolve over time. With these experiments we hope to better understand whether these boundary conditions, acting alone, together or in combination with other climate feedbacks, help to explain some of the atmospheric CO_2 variations recorded in the ice cores (Petit et al., 1999). Figure 5.2 shows Dome Concordia (Dome C) CO_2 data (Monnin et al., 2001) and insolation (Berger, 1978) over the last deglaciation. The maximum insolation occurs between 9 and 10 kBP. At 8 kBP most of the continental ice has disappeared (Crowley and North, 1991) and insolation remains close to the maximum value over this interval.

Table 5.2 shows all perturbation experiments that have been carried out with

experiment	initial condition	boundary condition
evp_cntrl	LGM_evp_gm, CO_2 = 200	olw = 280, op = 8kBP
evp_olw	LGM_evp_gm, CO_2 = 200	olw = 280, op = lgm/21kBP
evp_orb	LGM_evp_gm, CO_2 = 200	olw = 200, op = 8kBP
noevp/gm_cntrl	LGM_noevp_nogm, CO_2 = 200	olw = 280, op = 8kBP
noevp/gm_olw	LGM_noevp_nogm, CO_2 = 200	olw = 280, op = lgm/21kBP
noevp/gm_orb	LGM_noevp_nogm, CO_2 = 200	olw = 200, op = 8kBP
noevp_cntrl	LGM_noevp_gm, CO_2 = 200	olw = 280, op = 8kBP
lgm_trans_orb	LGM_evp_gm, CO_2 = 200	olw = evolves, op = evolves

Table 5.2: Perturbation experiments showing both initial and boundary conditions used. Each experiments is run from one of the equilibrium experiments shown in Table 5.1 and is listed as the initial condition. noevp/gm and nogm experiments use standard horizontal/ vertical diffusion. Boundary conditions are indicated by their prescribed radiative CO_2 forcing (olw) and orbital forcing (orb). Note that CO_2 concentration is given in ppmv

initial and boundary conditions used. Both LGM_evp_gm and LGM_noevp_nogm have been run with both boundary conditions changed (denoted by the extension _cntrl) and with only one of the boundary conditions changed (denoted by either _orb or _olw extension). These experiments will be discussed in the following subsection while we present the results for the _cntrl experiments below. Difference maps in Fig. 5.3 through Fig. 5.5 show the effects of applying both 8kBP boundary conditions - both orbital and radiative forcing - to each equilibrium experiment listed in Table 5.2. All differences are taken between the equilibrium and after 100 years of running the control (cntrl) run as this time gives the most dramatic changes in the atmospheric CO_2 associated with changing boundary conditions - before the system begins to equilibrate.

Maps of CO_2 and heat flux are shown in Figure 5.3 for the three models. Fig 5.3 (a,b) show differences between year 100 and the equilibrium for the model which includes both sea ice dynamics and GM mixing parameterization. It is clear that heat and CO_2 flux are related; where there is high heat flux out of the ocean (negative values in red) more CO_2 is taken up by the ocean (positive CO_2 uptake in red) and vice versa. One notable difference between the CO_2 and heat flux fields occurs in the North Atlantic where there is a band of negative heat flux (red) with positive heat flux (blue) on either side of this. The CO_2 uptake however is positive over this region, even where the heat flux is positive, which can be explained by the loss of sea ice here (Fig. 5.4a). This area is ice covered in the equilibrium run, although

the ice melts when 8 kBP boundary conditions are applied, leading to increased interaction between the surface water and the atmosphere above. Although heat can pass through the ice cover, CO_2 does not, and surface waters are not in equilibrium with the atmosphere. Thus the newly exposed ocean surface will have an initial uptake of CO_2 as SSTs in this area are low and pCO_2 in the surface waters are lower than the atmospheric pCO_2, resulting in a positive CO_2 flux into the ocean until an equilibrium is reached. The remaining pattern in heat flux looks similar to that of CO_2 flux except in the high latitudes where there is permanent ice cover. Differences in heat flux between the model experiments can still result in these high latitude regions due to the heat flux through the ice.

In the experiments which neglect ice dynamics, the highest fluxes of both heat and CO_2 occur in the North Atlantic where there is actually an increase in sea ice (Fig. 5.3c,d). The magnitude of the heat flux here is very large, almost 150 W m^{-2} and almost -3 mol m^{-2} yr^{-1} of CO_2 difference in flux (the maximum magnitude on the colour scale is smaller in order to better discern smaller scale features). Large differences in heat and CO_2 flux also occur in the Southern Ocean where there is a reduction in sea ice concentration (Fig. 5.4 c), except one small region close to the Ross Sea which shows an increase in sea ice concentration, corresponding to a decrease in CO_2 uptake and a positive difference in heat flux. Overall there is more CO_2 uptake in the Atlantic ocean between 45°N and 45°S, and in the southern Indian Ocean, with the neglect of ice dynamics. There is also less upwelling along the western South American coast with the inclusion of this parameterization, and thus less outgassing of CO_2.

When standard horizontal/vertical diffusion is included (instead of GM), the largest changes in heat and CO_2 flux occur in the Southern Ocean. The large more circular features are a result of unrealistic convective plumes that occur in this area due to the differences in mixing scheme. The large differences in heat flux in the North Atlantic (Fig.5.3e,f) result primarily from a decrease in the sensible heat flux (positive upwards) in this region. The model which includes GM mixing also shows similar changes in heat flux in the North Atlantic (Fig.5.3c,d), although in this case there is a decrease in the (upward) sensible heat flux due to a large increase in sea ice cover over this region. Although there is a decrease in the overturning strength of about 3 Sv (also see Fig. 5.12c) this does not seem to affect the heat flux. With a reduced overturning there is reduced heat transport to the North Atlantic and less heat being lost to the atmosphere here, resulting in the positive difference. It is interesting to note that this feature is similar in pattern to that when GM is included

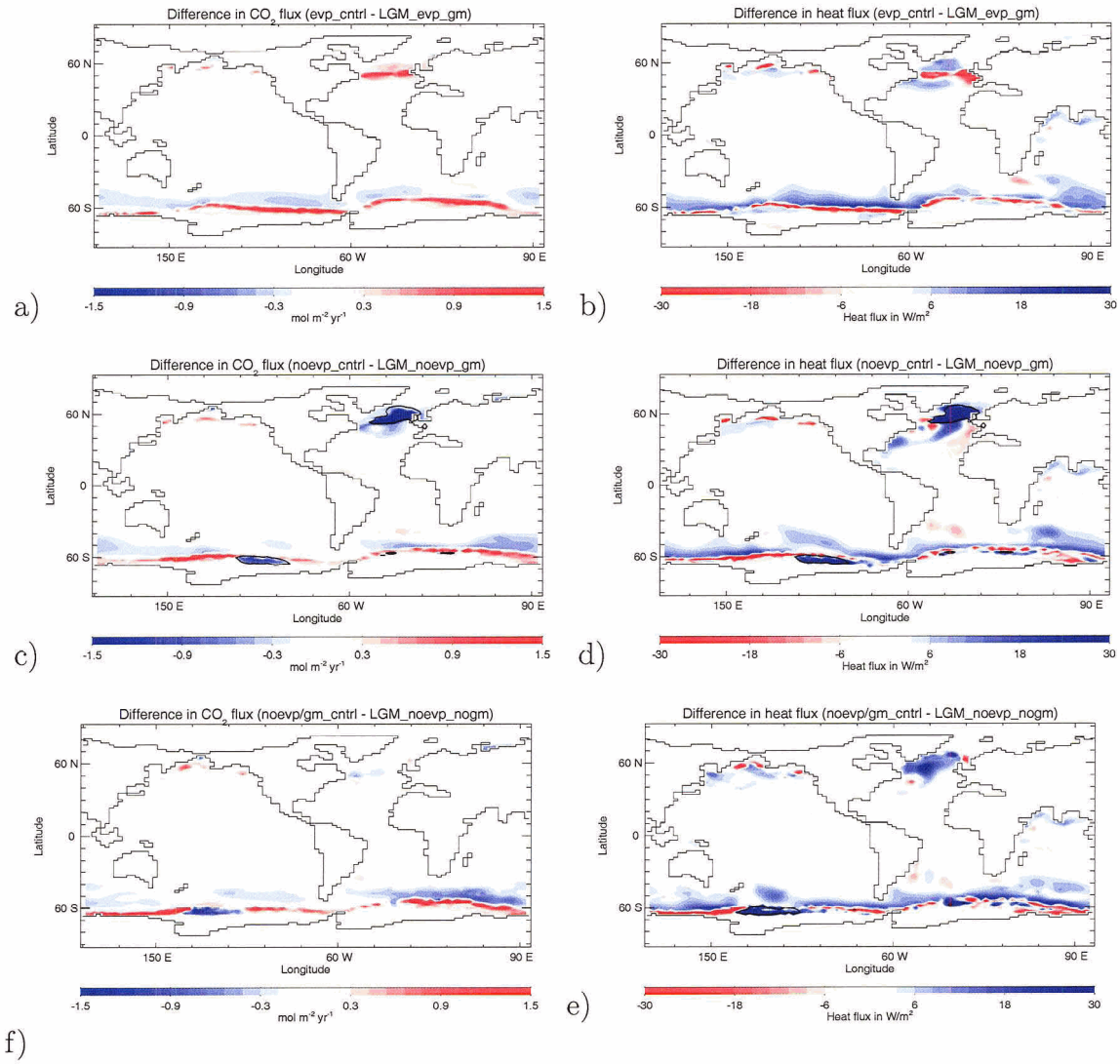

Figure 5.3: Differences of CO_2 and heat flux for _cntrl perturbation experiments between year 100 and the equilibrium. _cntrl experiments include changes in both orbital and CO_2 radiative forcing. _evp and _noevp differences are taken between year 100 and the equilibrium, whereas _noevp/gm is taken between year 200 and the equilibrium, corresponding to the maximum increase in atmospheric CO_2 for each experiment.

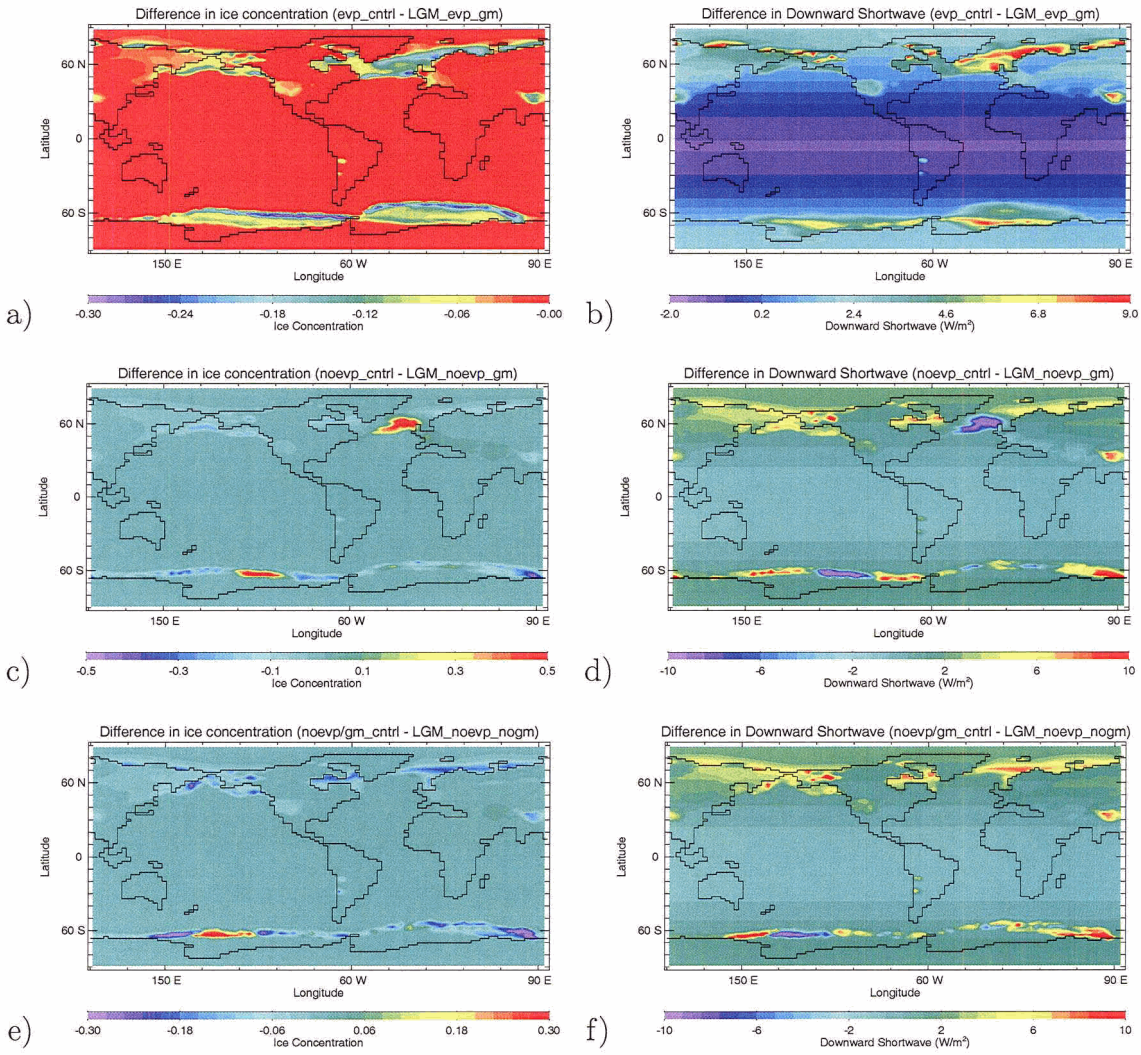

Figure 5.4: Difference plots of sea ice concentration and downward shortwave radiation for _cntrl perturbation experiments (as in Figure 5.3) between year 100 and the equilibrium experiment. _cntrl experiments include changes in both orbital and CO_2 radiative forcing. _evp and _noevp differences are shown at year 100 (year 100 - equilibrium), whereas _noevp/gm is shown at year 200 (year 200 - equilibrium), corresponding to the maximum increase in atmospheric CO_2 for each experiment

(Fig 5.3d) although in this case, there is a large change in sea ice cover.

Maps for both sea ice concentrations and downward shortwave radiation are shown in Figure 5.4. The orbital parameters have been changed from 21 kBP (in the equilibrium) to 8 kBP and the differences in the annual mean downward shortwave for each experiment are plotted in (Fig 5.3b,d,f). Although the increase in the insolation shown in Fig. 5.2 is is about 50 W m^{-2}, it is in July at 65°N and occurs at a specific location. Our model also shows quite large differences along this latitude, however we have shown only the annual mean. The zonal mean along this latitude is shown in Fig 5.8a,b for the evp_cntrl and noevp/gm_cntrl experiments, and the largest values are $\sim$4 Wm^{-2}. It is important to note however that although this zonal change in the insolation is not great, the seasonal and latitudinal distribution of insolation can be amplified, particularly in the high latitudes through changes in sea ice and wintertime convection (Weaver et al., 2001). Changes in radiative forcing from 21 to 8 kBP due to atmospheric CO_2, on the other hand, have a more pronounced effect on the annual mean radiative forcing. All the maps show an increase in radiative forcing in the high latitude regions. A loss of sea ice due to an increase in the radiative forcing (from an increase in CO_2) results in a decrease in the latitudinally dependent albedo. The difference in radiative forcing due to orbital parameters also causes changes. There is an increase in downward shortwave in the high latitudes, which is more pronounced in the north, and a decrease to the equatorial regions. These effects will be discussed separately in the following subsection. Sea ice concentrations are generally decreased in all models with the exception of noevp_cntrl which shows increased sea ice concentrations in the North Atlantic and in the Southern Ocean, from the equilibrium run. The noevp/gm_cntrl model also has an increase in sea ice concentration just north of the Ross Sea. An increase in sea ice affects the downward shortwave due to increased albedo in these regions, although this is very localized.

Maps of surface and zonal Atlantic DIC concentrations for each model are shown in Figure 5.5. The largest changes occur in the North Atlantic where surface DIC concentrations are larger, corresponding to differences in the ice concentration and higher uptake. The evp_gm run (a,b) shows a sharp interface where decreased sea ice concentrations correspond to increased surface DIC concentration due to the increase in CO_2 flux. In general where there is a reduction in ice concentration, the resulting increase in CO_2 flux leads to higher surface DIC concentrations, and vice versa. In the equatorial regions there is a slight decrease in the surface DIC concentration. This is also shown in the Atlantic zonal difference of DIC. The largest negative differences in surface DIC occur in the North Pacific which correspond to regions of slightly

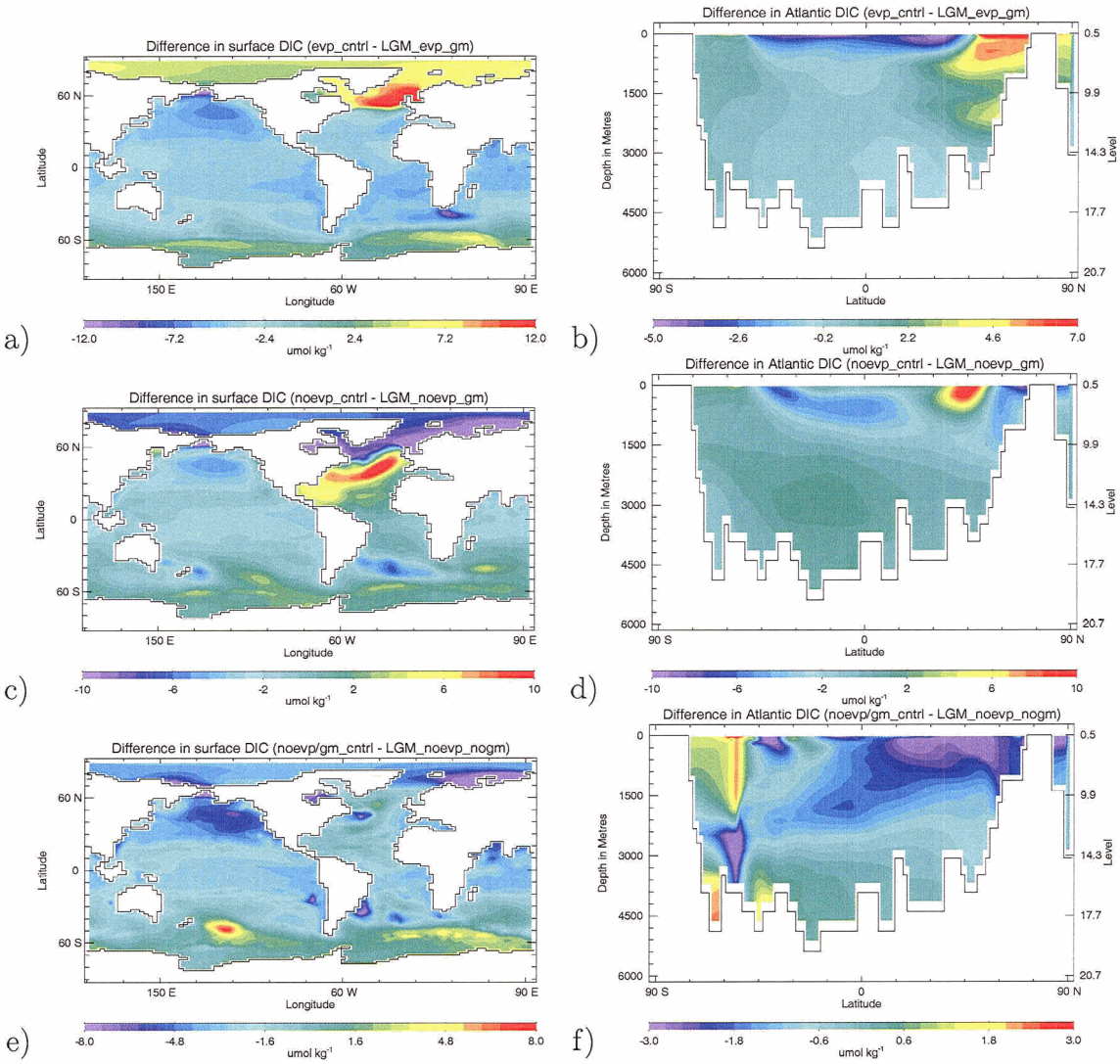

Figure 5.5: Maps of surface DIC and zonal DIC for the Atlantic for _cntrl perturbation experiments (as in Figure 5.4) between year 100 and the equilibrium. _cntrl experiments include changes in both orbital and CO_2 radiative forcing. _evp and _noevp differences are taken between year 100 and the equilibrum, whereas _noevp/gm is taken between year 200 and the equilibrium, corresponding to the maximum increase in atmospheric CO_2 for each experiment. Note that the perturbation DIC concentration differences are not very large compared to an average background DIC concentration of ~2000 $\mu molkg^{-1}$.

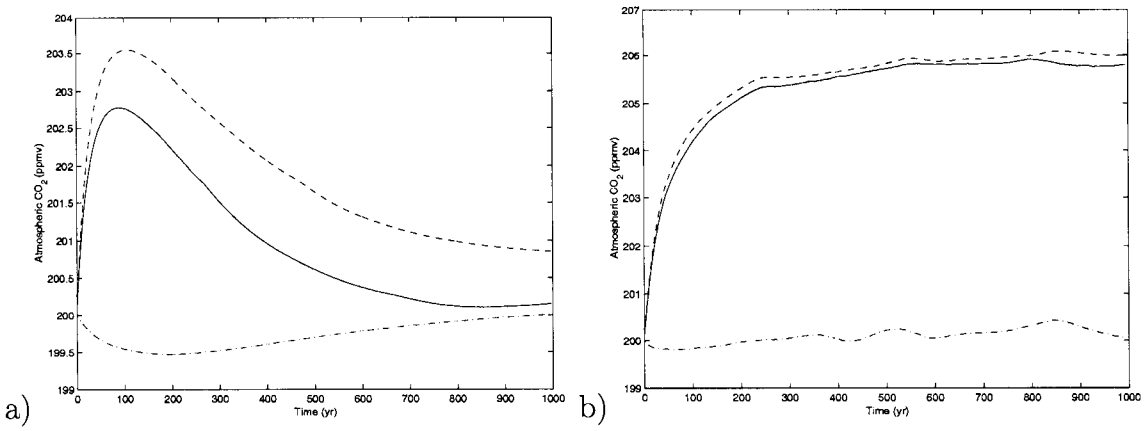

Figure 5.6: Atmospheric CO_2 concentrations (ppmv) for _cntrl experiments (solid line), _orb (dash-dotted line) and _olw (dotted line). Sea ice dynamics and GM mixing are used in a, and thermodynamic sea ice and standard horizontal/vertical diffusion in b.

reduced CO_2 uptake here. Fig. 5.5e,f on the other hand, show little change in the North Atlantic. There is little change in sea ice cover here resulting in little differences between both heat and CO_2 flux. In this experiment, standard horizontal/vertical diffusion is used and there is an unrealistic circular feature in the South Pacific which has high surface DIC concentrations corresponding to higher heat and CO_2 uptake. The Atlantic zonal DIC map also shows some spurious features in the Southern Ocean which most likely correspond to regions of unrealistic convection when GM mixing is removed.

Although each parameterization gives quite different results, on a regional scale the overall effect on atmospheric CO_2 is small. Figure 5.6 shows the changes in atmospheric CO_2 concentrations for model runs which include GM and sea ice dynamics (a) and thermodynamic sea ice and horizontal/vertical diffusion (b). The solid curves in Figs. 5.6a,b, show the effects of changing both boundary conditions on atmospheric CO_2. The dotted curve shows the effects of changing radiative CO_2 forcing (olw) and the dash-dotted curve shows changes in orbital forcing (orb) - these will be discussed further in the following section. In Fig. 5.6a, the overall change in CO_2 concentrations is very small, less than 3 ppmv altogether, and certainly not very significant in explaining a change of 80 ppmv as recorded in the ice cores. The change when sea ice dynamics is removed (not shown) is also small, with an increase of only 5 ppmv. When standard horizontal/vertical diffusion is used the change in CO_2 is slightly higher, around 5.5 ppmv, although still not very significant.

5.3.1 Sensitivity to individual boundary conditions

In this subsection differences between individual boundary conditions, corresponding to Fig. 5.7 through Fig. 5.9, are examined. Experiments in which the orbital parameters are held fixed at 21 kBP are denoted by the _orb extension (radiative CO_2 changing from 200 to 280 ppmv). Those in which radiative CO_2 is held fixed at 200 ppmv are denoted by the _olw extension and correspond to changing orbital parameters from 21 to 8 kBP (see Table 5.2). In these experiments, CO_2 is allowed to freely evolve over time however the CO_2 radiative forcing is fixed at either 200 or 280 ppmv.

The differences maps relating to the evp_cntrl model, which includes both sea ice dynamics and the GM mixing parameterization, are shown in Figure 5.7. The left hand column shows the difference associated with changing the radiative CO_2 forcing while the right hand column shows differences associated with orbital parameters. The largest magnitude differences occur in the CO_2 flux, SST and ice concentrations fields for the experiments where CO_2 radiative forcing is changed. Most of these differences occur as a result of the large differences in sea ice concentration (Fig 5.7.e). Differences in SST and ice concentration corresponding to changes in orbital forcing show both positive and negative differences of smaller magnitude (d,f) than for the experiments with CO_2 radiative forcing changed. Difference in downward shortwave radiation are shown in the bottom panels and zonal averages in Fig. 5.8. The differences due to changes in orbital forcing are much larger than those associated with CO_2.

Fig. 5.8b shows the combined zonal average difference in shortwave radiation whereas c and d show the individual contributions. Clearly changes in CO_2 radiative forcing have the dominant effect when both boundary conditions are considered as the shape of the curve is similar in character for both. Fig. 5.8c on the other hand, shows difference only in high latitudes as a result in changes to sea ice, and the Southern Ocean is dominated by these effects when both boundary conditions are considered. These positive and negative differences seen in Fig. 5.7h and Fig. 5.8d in the shortwave radiation lead to the positive and negative differences in the CO_2 flux, SST, and ice concentration fields shown in Fig. 5.7. The ice concentration for example, shows both a negative difference in sea ice and a positive difference in the continental ice, which is expected for 21 kBP.

Figure 5.9 shows similar plots for the experiments which include thermodynamic sea ice and standard horizontal/vertical diffusion. Although the overall change in

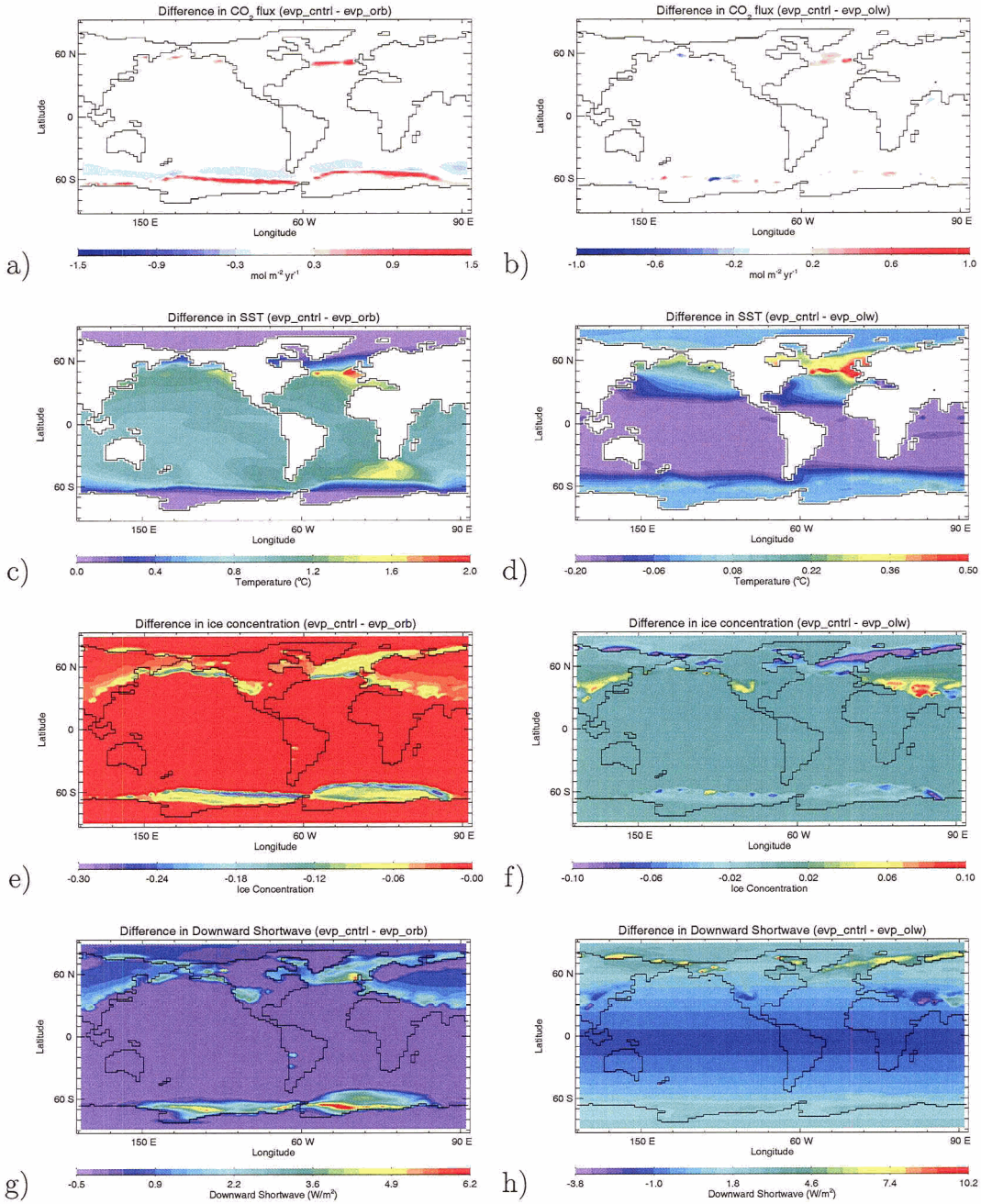

Figure 5.7: Difference maps for evp experiments including CO_2 flux, SST, ice concentration and downward shortwave differences, all taken at year 100. Left hand plots show differences between _cntrl and _orb (orbital forcing fixed at 21 kBP). Right hand plots show differences between _cntrl and _olw (radiative CO_2 forcing fixed at 200 ppmv).

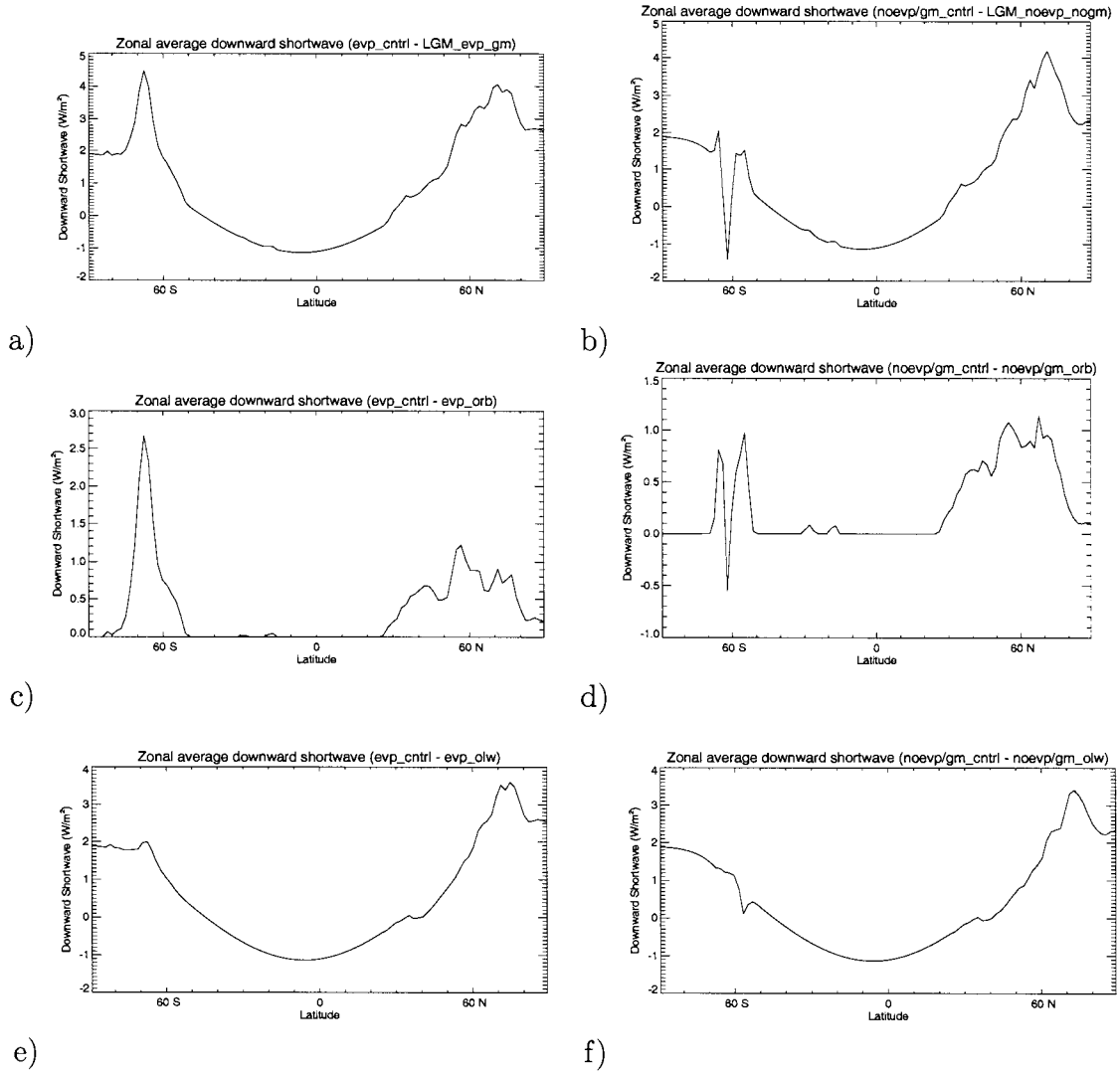

Figure 5.8: Difference in zonally averaged downward shortwave for evp and noevp/gm experiments. Top panel (a,b) show differences between _cntrl and LGM equilibriums, middle panel (c,d) show differences between _cntrl and _orb (orbital forcing held fixed at 21 kBP) and bottom panel (e,f) shows difference between _cntrl and _olw (radiative CO_2 forcing held fixed).

atmospheric CO_2 due to changing orbital parameters is negligible in this model (Fig 5.6b) we can clearly see that there are large regional differences in the maps shown for both orbital and CO_2 boundary conditions. In the _olw experiments, the most notable differences are in the CO_2 and SST fields (b,d) where most of the oceans except for the high latitude regions show outgassing.

The shortwave radiation also shows a negative difference (Fig. 5.9f and Fig. 5.8f) which is reflected in the heat flux and results in CO_2 outgassing. If we compare the zonally averaged shortwave radiation for _cntrl experiments (a,b) the largest differences occur in the Southern Ocean - evp_cntrl shows a positive difference of 4.5 W m^{-2} whereas noevp/gm_cntrl shows a negative difference of 1.5 W m^{-2}. This large negative spike in Fig 5.8b is a result of neglecting sea ice dynamics. This corresponds to a small region of increased sea ice cover, which can also be seen in Fig. 5.9e.

Comparing the effect of the individual boundary conditions on atmospheric CO_2 (Fig. 5.6), orbital forcing alone (dash-dotted curve) has little effect on the overall atmospheric CO_2 concentration for each model. In fact the response shown in the _evp model is slightly negative. When the radiative CO_2 forcing is changed however, there is a slightly larger increase in atmospheric CO_2 of about 1 ppmv (a) which is not very significant overall. In (b), the combined effect on CO_2 is almost entirely a result of changes in CO_2 radiative forcing. This is interesting as Fig. 5.9 showed that there were still large regional differences as a result of changing the orbital forcing only.

These experiments have also been carried out beginning with both preindustrial and 8 kBP equilibrium runs (orbital parameters for both 1850 and 8 kBP and CO_2 of 280 ppmv) and then applying LGM boundary conditions to each equilibrium. Overall, the changes in atmospheric CO_2 concentration are also quite small. The largest change ($\sim$8 ppmv) is with a present day equilibrium without the inclusion of sea ice dynamics. A transient experiment has also been carried out starting from LGM_evp_cntrl in which both orbital and radiative forcing evolve over the simulation time period. This simulation was run from 21 kBP for 5000 years and resulted in only 1 ppmv increase in atmospheric CO_2 concentrations.

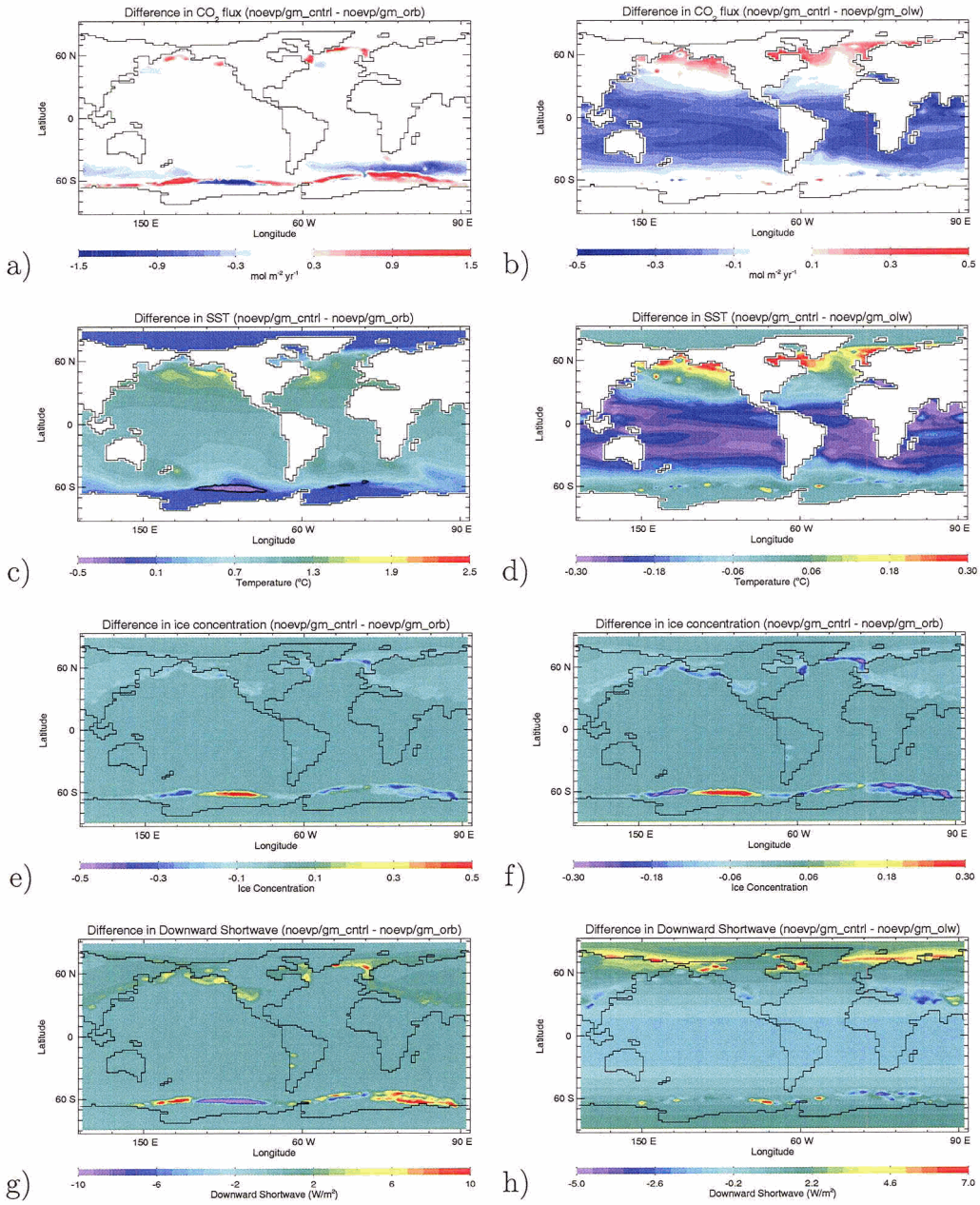

Figure 5.9: Difference maps as in Fig 5.7 except for noevp/nogm experiments all taken at year 200. Left hand plots show differences between _cntrl and _orb (orbital forcing fixed at 21 kBP). Right hand plots show differences between _cntrl and _olw (radiative CO_2 forcing fixed at 200 ppmv).

5.3.2 Effects of sea ice cover and overturning on CO_2 flux

In the previous sections, differences in sea ice extent and concentration appear to correspond to the largest differences in oceanic CO_2 flux. Below, we further analyze the relationship between sea ice cover and meridional overturning on CO_2 flux. In order to better understand changes in sea ice cover and CO_2 flux during the LGM we first look at the seasonal cycles in the equilibrium LGM_evp_gm experiment.

Figures 5.10a,b show the relationship between the seasonal cycle of sea ice cover and CO_2 flux in both hemispheres (over 3 years) in equilibrium. Both curves are plotted on the same scale which clearly shows the dominance of the northern hemisphere in the global seasonal changes in sea ice cover and CO_2 flux. The cycle in the northern hemisphere begins as the area covered by sea ice starts to increase while the CO_2 flux remains fairly constant, $\sim$-0.5 Pg C yr^{-1}. As the sea ice approaches its maximum concentration, the CO_2 outgassing begins to decrease (becomes less negative) and then quickly becomes positive over the northern hemisphere (overall uptake) while the sea ice cover remains around 2.3×10^{12} m^2 (although slightly decreasing) until a peak is reached in CO_2 uptake of 0.7 Pg C yr^{-1}. After this point there is an abrupt (small) increase in sea ice cover which corresponds to a decrease in CO_2 uptake and the uptake continues to decrease with a corresponding decrease in sea ice cover.

Although there is a relationship between the sea ice cover and the CO_2 flux, it does not seem to be governed solely by the change in air-sea interaction due to changes in ice cover. As the sea ice cover increases however, there is almost a linear relationship with the increase in the overturning strength in the North Atlantic. Fig. 5.10c shows the relationship between the seasonal overturning strength in the North Atlantic and CO_2 flux in the northern hemisphere, plotted for one year only. In general, the CO_2 flux increases with an increase in the overturning strength and vice versa. Although difference maps show locally high uptake of CO_2 when there is a decrease in sea ice cover (for e.g. Fig. 5.3 showing CO_2 flux and Fig. 5.4, sea ice concentration), the seasonal changes in CO_2 flux seem to be influenced more by the change in overturning strength which result from the changes in sea ice growth and melt.

Although surface waters do not take long to equilibrate with atmospheric pCO_2 ($\sim$ 1 year, much shorter than the scale considered here), and the main rate-limiting process for CO_2 flux is between the transfer from the surface mixed layer to the deep ocean, changes in sea ice immediately affect the local air-sea exchange by growth and melting of the sea ice. Sea ice melting and formation also leads to changes in water

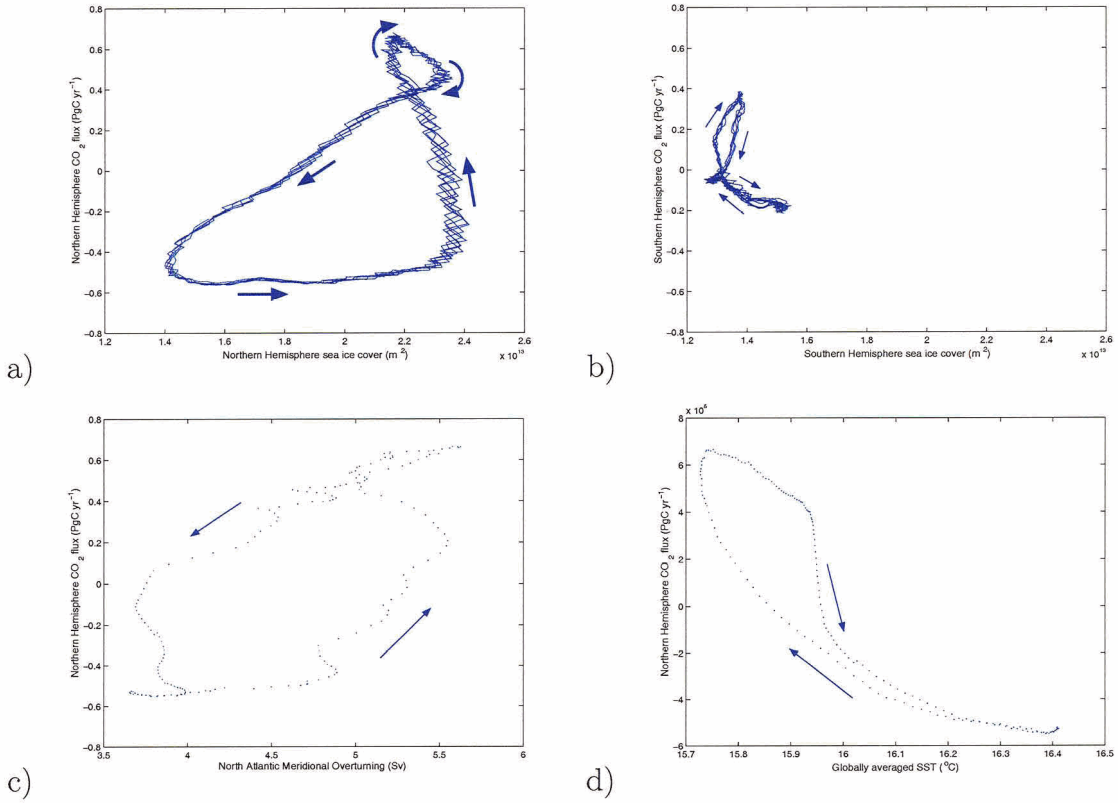

Figure 5.10: LGM_evp_gm seasonal sea ice, air-sea CO_2 flux, overturning and SSTs. Top panel (a,b): northern and southern hemisphere CO_2 flux (Pg C yr^{-1}) plotted with sea ice cover (m^2). Bottom panel: CO_2 flux and corresponding meridional overturning strength in the North Atlantic (c) and CO_2 flux plotted with globally averaged SST (d).

mass properties which affect deep convection. An increase in freshwater input through sea ice melt decreases the density of surface waters and reduces convection. On the other hand, sea ice formation, which rejects dense brine, has the opposite effect. Thus changes in sea ice lead to immediate local changes in CO_2 uptake through increased or decreased air-sea exchange and secondarily through changes in water mass properties which are not immediately felt on the oceanic pCO_2. In the LGM_evp_gm experiment, it seems that the daily integrated flux over the northern hemisphere is influenced more by slower changes in the overturning strength than by local increases in air-sea interaction. Changes in SST also affect CO_2 uptake; as SSTs increase, solubility of CO_2 in surface waters decreases. Fig. 5.10d shows that as the globally averaged SST decreases, CO_2 flux increases and vice versa.

Figure 5.11 shows both north and southern hemisphere changes in sea ice cover

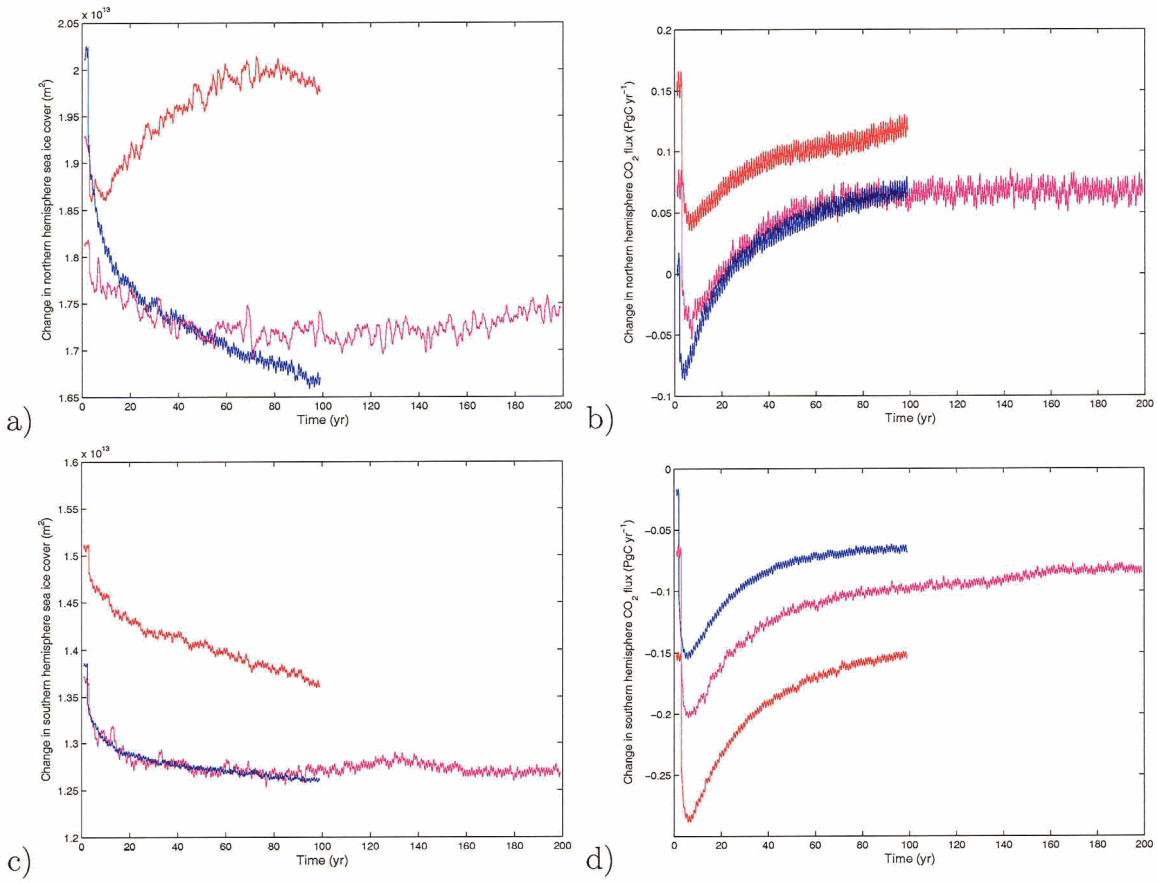

Figure 5.11: Changes in northern hemisphere sea ice (m^2) and air-sea CO_2 flux (Pg C yr^{-1}) (a,b) for evp_cntrl (blue), noevp_cntrl (red) and noevp/gm_cntrl (pink). (c,d) are the same except for southern hemisphere.

and CO_2 flux over the first 100 years of model runs for evp_cntrl (blue curves) and noevp_cntrl (red curves) and for the first 200 years of model run for noevp/gm_cntrl (pink curves). These time intervals correspond to those of the difference maps seen in the previous sections. In both hemispheres, CO_2 flux and sea ice cover initially decrease for each experiment when 8 kBP boundary conditions are applied. After the initial decrease in both CO_2 and sea ice cover, CO_2 flux begins to increase slowly while sea ice cover slowly decreases over the interval. CO_2 flux in the northern hemisphere however is positive for each experiment over the first 100 year period, indicating that the ocean is taking up CO_2 rather than outgassing. One exception to this is the noevp_cntrl run where both CO_2 flux and sea ice cover slowly increase over the first 50 years.

Altogether the northern hemisphere sea ice cover changes the most dramatically in evp_cntrl (from 20×10^6 km^2 to 16.6×10^6 km^2 compared to southern hemisphere

experiment	integrated CO_2 flux SH (Pg C)	integrated CO_2 flux NH (Pg C)	total CO_2 (atm) (ppmv)
evp_cntrl	-8.71	2.74	-2.77
noevp_cntrl	-19.09	9.38	-4.51
noevp/gm_cntrl	-21.47	10.43	-5.13

Table 5.3: Integrated carbon flux for southern and northern hemispheres during 100 years of model runs (corresponding to Fig. 5.11). The total carbon flux is negative in each case, indicating an overall outgassing to the atmosphere. The integrated carbon in the southern hemisphere shows an outgassing for each experiment whereas in the northern hemisphere there is an overall uptake of carbon. The total integrated carbon flux can be compared to the increase shown in the atmosphere (Fig 5.9).

changes of 13.9 $\times$ 10^6 km^2 to 12.6 $\times$ 10^6 km^2). Table 5.3 shows the integrated CO_2 flux for each hemisphere. The southern hemisphere integrated CO_2 flux for each experiment is negative, indicating an overall outgassing of CO_2 to the atmosphere whereas the northern hemisphere shows an overall uptake. The southern hemisphere however seems to dominate changes in CO_2 flux as the overall effect is a net outgassing and corresponding increase in atmospheric CO_2. The dominance of the southern ocean outgassing can also be seen in Fig. 5.3a,c,e. Although there is increased uptake where sea ice concentrations have decreased, there is a large regional increase in outgassing (more negative) after 100 years in each model. This outgassing occurs between about 60-45°S and corresponds to an increase in heat flux along this band. Although each model shows a net positive flux in the northern hemisphere, they are not regionally consistent in their patterns of uptake if the flux maps in Fig. 5.3 are compared. The evp_cntrl model shows the smallest difference in uptake which is likely due to the change in sea ice cover in the North Atlantic. noevp_cntrl on the other hand, shows an increase in sea ice cover here and a corresponding decrease in uptake, although the tropical Atlantic shows a large regional increase in uptake. The integrated uptake in noevp/gm_cntrl is the largest (10.43 Pg C) although except for small increases along the tropical Pacific and Atlantic, there are no obviously large regional differences.

Our model's present day sea ice cover in the Southern Ocean is slightly larger than observations (8.2 $\times$ 10^6 km^2 compared to our model, 11.6 $\times$ 10^6 km^2). Although sea ice concentrations in the Southern Ocean increase in our LGM simulation (13.9 $\times$ 10^6 km^2), the equatorward extent is underestimated in both the Drake passage and south of Australia as compared to estimates made by Crosta and Pichon (1998). Since

changes in sea ice in the Southern Ocean affect air-sea gas exchange and production of AABW, further influencing CO_2 flux, our modelled sea ice cover may lead to slight differences in CO_2 flux, although it is unlikely that they are significant as the overall changes shown here are very small.

It has been suggested that changes in Antarctic sea ice cover have little influence on atmospheric CO_2 concentrations in ocean GCMs model studies due to excessive low-latitude upwelling of deep water in the Southern Ocean (Stephens and Keeling, 2000). Using a similar model version to ours, Saenko et al. (2002) show improved Southern Ocean tracer distributions with the inclusion of wind advected sea ice and Schmittner (2003) showed good agreement between radiocarbon ages in glacial bottom water reconstructions also using a similar model version which included wind advected sea ice, isopycnal and GM mixing. Gnanadesikan and Toggweiler (1999), using the GFDL ocean model (Pacanowski, 1995), showed that including both isopycnal and GM mixing reduces the overall rate of vertical exchange in the Southern Ocean and significantly improves silicate fluxes when compared to data. Using our pd_evp_gm model, we also show good agreement with anthropogenic CO_2 data (Gruber, 1998) under global warming scenarios (Chapter 3). Without the inclusion the GM parameterization (including isopycnal mixing) and dynamical sea ice both LGM_noevp_gm and LGM_noevp_nogm show no overturning cell in the Southern Ocean. It is generally thought that the Southern Ocean was saltier during the LGM due to both a decrease in sea level and an increase in brine rejection due to sea ice formation. It is likely that the formation of AABW increased and certainly the two models which show no overturning seem unrealistic.

Figure 5.12a shows the meridional overturning streamfunction south of 30°S for the equilibrium run LGM_evp_gm. The rate of the overturning is about 8 Sv, whereas the other equilibrium models show no overturning, or Deacon cell, when sea ice dynamics is not included. Improvements in model CFC distributions in the Southern Ocean are mostly a result of improved AABW formation (see for e.g. Saenko et al., 2002; Dutay et al., 2002).

The rate and location of bottom water formation is controlled by the wind driven divergence of sea ice around Antarctica. AABW is fed by brine release during regrowth of sea ice around Antarctica. This is enhanced by sea ice movement away from Antarctica, exposing open water to cold air and increased heat loss, leading to further sea ice growth and associated brine rejection (Saenko et al., 2002). The rate of AABW formation is slightly stronger in our LGM simulation over our present day simulation (with the same sea ice and mixing parameterizations) due to an increase

in density of AABW, consistent with Schmittner (2003).

The 8 kBP equilibrium run (8kBP_evp_gm) has a slight reduction in the meridional overturning strength in the Southern Ocean (1 Sv). Fig. 5.12b shows the difference between the equilibrium 8kBP_evp_gm and the perturbation evp_cntrl (with 8 kBP boundary conditions) experiments. There is little difference in the Southern Ocean overturning between the equilibrium and perturbation run, however the overturning strength in the North Atlantic is about 4 Sv stronger in the equilibrium run. North Atlantic overturning strength for each model is plotted in (c), where the individual data points plotted represent the equilibrium overturning strengths for evp_cntrl and noevp_cntrl models.

There is clearly a large difference between the equilibrium and perturbation overturning strengths in the North Atlantic (Fig. 5.12c). Over the 100 yr period, there is almost no change in the strength of the overturning in either evp_cntrl or noevp/gm_cntrl. The equilibrium overturning however is $\sim$ 8 Sv stronger than in the perturbation. noevp_cntrl shows a very large reduction after 100 yrs from 12 Sv to 3 Sv, compared to the equilibrium overturning of 14 Sv. This is due to the increase in sea ice cover in the North Atlantic which causes a much shallower and weaker formation of bottom water in this region. This decrease in overturning leads to a reduction in North Atlantic CO_2 uptake. Corresponding to 8kBP radiative forcing, the SSTs in each model also increase, leading to a reduction in overall uptake through solubility effects.

5.4 Discussion and Conclusions

In this chapter, we applied 8kBP boundary conditions (orbital and radiative) to three different LGM models, varying sea ice and mixing parameterizations, in order to study changes in oceanic CO_2 uptake and resulting atmospheric CO_2 concentrations during glacial to interglacial transition. Using a coupled ocean-atmosphere-sea ice model, including an inorganic carbon cycle, we find little change in atmospheric CO_2 concentrations under changed glacial-interglacial boundary conditions.

Recent box model studies have shown promising results in explaining glacial-interglacial CO_2 changes through changes in either sea ice cover or water column stratification in the Southern Ocean (for e.g. Stephens and Keeling, 2000; Toggweiler, 1999; Gildor and Tziperman, 2002). Archer et al. (2003) suggests that atmospheric pCO_2 in box models is largely controlled by the high latitudes, whereas in GCMs the control of high and low latitudes is more evenly distributed making the Southern

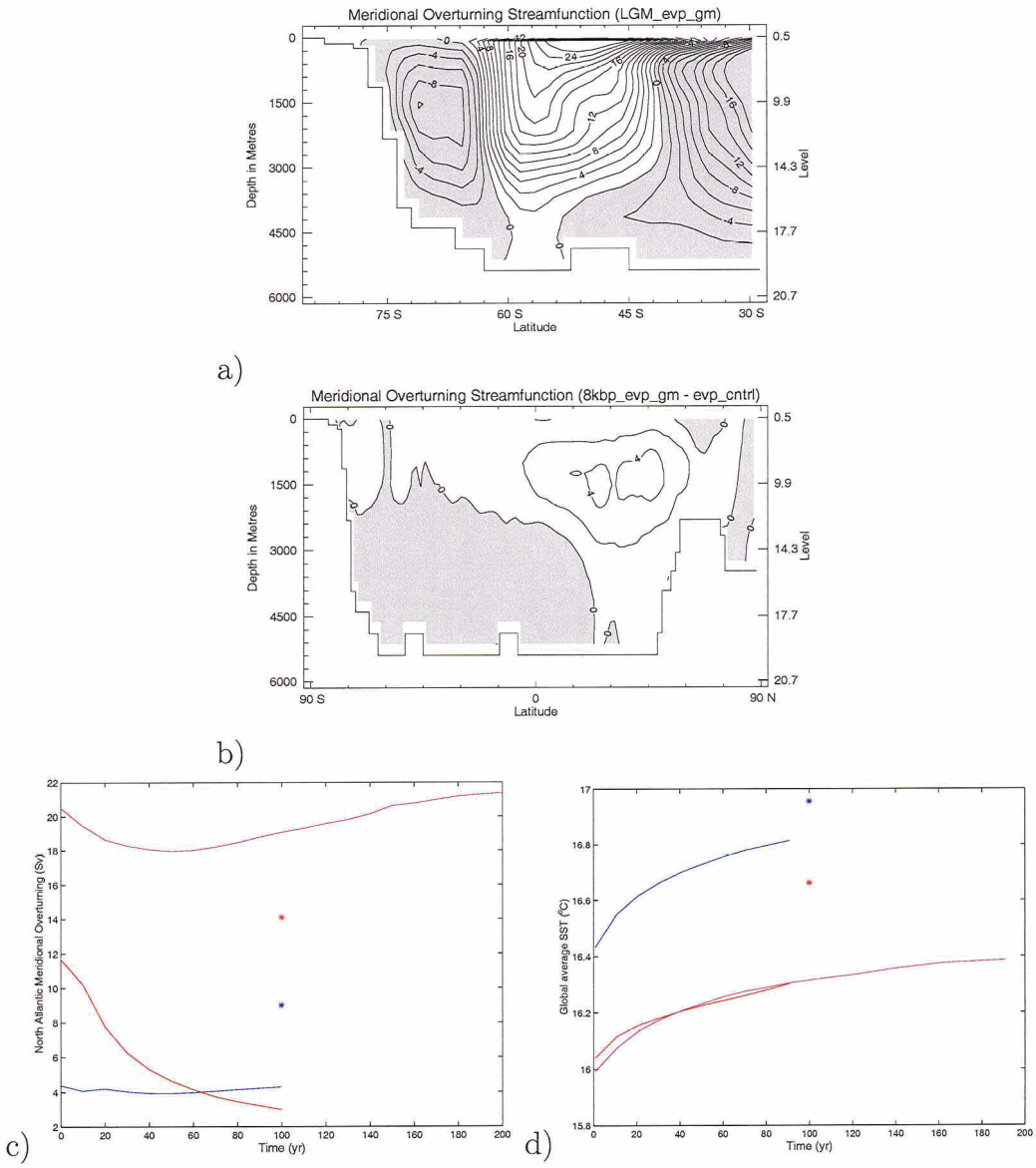

Figure 5.12: (a) Meridional overturning streamfunction in the southern hemisphere for LGM_evp_cntrl. Shaded regions (negative contours) are counterclockwise. The maximum strength is ~8 Sv. (b) Difference in overturning streamfunction between equilibrium (8kBP_evp_gm) and perturbation (evp_cntrl). (c) North Atlantic overturning strength (Sv) for evp_cntrl (blue), noevp_cntrl (red) and noevp/gm_cntrl (pink) experiments. Individual data points indicate equilibrium value at 8kBP for evp model (blue) and noevp (red). (d) Globally averaged SSTs for each experiment as in c.

Ocean mechanisms (increased sea ice cover and/or stratification) significantly less important. In this chapter, we have explored changes in CO_2 concentration related to sea ice changes and model sea ice parameterization, by applying 8 kyr BP boundary conditions to an LGM equilibrium. Although we find large changes in both northern and southern hemisphere sea ice cover, and large inter-model variation in the rates of AABW, we find atmospheric CO_2 concentrations change by at most 6 ppmv.

When each boundary condition is considered separately, changes in both orbital and radiative forcing lead to large regional changes in CO_2 uptake. Changes in radiative CO_2 forcing however lead to the largest changes in CO_2 flux and are responsible for a positive increase in atmospheric CO_2. Orbital forcing, on the other hand, resulted in a slight decrease in atmospheric CO_2. Using a similar model, taking into account the presence of ice sheets via an ice albedo feedback, Weaver et al. (1998) showed that the most important forcing in representing an LGM climate is atmospheric CO_2, with ice sheet albedo feedbacks also contributing to cooling. With the inclusion of an interactive continental ice sheet to this model, Yoshimori et al. (2001) found that orbital forcing is more important than CO_2 forcing for ice-sheet maintenance and deglacial processes, although both need to act together for complete deglaciation to occur. This suggests that the inclusion of the continental land ice model may be an important component if we are to properly address glacial-interglacial CO_2 uptake.

When 8 kBP boundary conditions are applied to each LGM equilibrium, sea ice cover in both hemispheres decreases. Correspondingly, there is an initial decrease in CO_2 flux which then gradually increases as sea ice cover decreases. The meridional overturning in the Southern Ocean does not change significantly in the dynamics sea ice (evp) model, however there is no formation of AABW when thermodynamic only sea ice is included in either the LGM or perturbation experiments. The strength of the North Atlantic overturning changes little except when thermodynamic only sea ice is used (including GM parameterization for tracer mixing) which shows an increase in sea ice cover in the North Atlantic and a corresponding decrease in overturning of 9 Sv. Global SSTs are shown to increase in each model and related solubility changes contribute to a decrease in uptake. Overall, the southern hemisphere dominates the changes in CO_2 flux and the integrated flux is negative indicating a decrease in uptake and corresponds to the increase in atmospheric CO_2. The resulting increase in atmospheric CO_2 is dominated by decreased oceanic uptake between 60-45°S in the southern hemisphere. This feature corresponds to a similar pattern in increased heat flux. Although the decrease in northern hemisphere sea ice cover is larger than

that in the southern hemisphere, the integrated CO_2 flux is positive in the north and negative in the southern hemisphere.

We show that different model parameterizations for both sea ice and mixing result in large regional differences in CO_2 uptake although we find little overall variation in atmospheric CO_2 through physical mechanisms alone. The importance of the biological carbon cycle in addressing glacial-interglacial transition cannot be overlooked. It is possible that these physical 'Southern Ocean' mechanisms, may have a much larger effect on atmospheric CO_2 with the inclusion of both biological and carbonate pumps and so cannot be excluded. We also suggest that the coupling of a continental land ice model (Yoshimori et al., 2001), which improves LGM climatology, may also be a critical component to improving our understanding of glacial-interglacial CO_2 cycles.

6 Conclusions

In this thesis, an investigation of the inorganic carbon cycle under both past and future climate change has been carried out. The UVic Earth System Model was used, which incorporates a three-dimensional ocean general circulation model coupled to an energy moisture balance model of the atmosphere and a thermodynamic-dynamic sea ice model. To this model, I have coupled an inorganic carbon component, largely based on the OCMIP protocols (Orr et al., 1999). This model is an important step in addressing questions concerning the inorganic carbon cycle. In particular, an analysis of the feedbacks acting on the inorganic carbon cycle under future atmospheric CO_2 forcing is carried out. The response of the carbon cycle to past climate change, including glacial-interglacial and abrupt transitions, is then examined.

Future climate experiments were carried out whereby atmospheric CO_2 concentrations were increased exponentially from 1850 to 2100. In this study, the importance of the oceans in buffering atmospheric CO_2 is reaffirmed. It was found that the oceans have the ability to take up an additional 65-75% of the excess CO_2 in the atmosphere when climate feedbacks are included, confirming earlier studies carried out by Archer et al. (1997). Excess CO_2 that can potentially be taken up by the oceans depends on the final atmospheric CO_2 concentration, where a lower final concentration reveals that more CO_2 will be taken up in the long run. When climate feedbacks are assessed by removing their effects on carbon uptake, it was found that the oceans are able to take up an additional 44 PgC. Although there is an increase in SST under climate feedbacks, there is a slight increase in overturning once the atmospheric forcing is removed and a significant reduction in sea ice extent in both hemispheres which together help to counteract the solubility changes.

Model parameterizations of both sea ice and sub-grid-scale mixing processes have also been examined. We find that the inclusion of the Gent McWilliams mixing scheme leads to less uptake globally, $\sim$6%, and significant regional differences in uptake. The inclusion of this parameterization has been shown to improve model results in the UVic coupled model when compared to both CFC and radiocarbon observations (Robitaille and Weaver, 1995; Saenko et al., 2002; Schmittner, 2003) and this study also reveals the importance of ocean model parameterizations in obtaining better model estimates of oceanic carbon fluxes. The inclusion of both thermodynamic sea ice and dynamic sea ice have also been examined. We find little difference in the

overall global uptake between sea ice representations, although there are significant differences in regional uptake patterns and sea ice extent, most notably in the North Atlantic and southern hemisphere. Since the high latitude regions play a critical role in excess carbon sequestration, it is imperative that climate models include improved parameterizations of these processes in order to gain a better understanding of how carbon uptake will be affected in these regions.

Paleoclimate studies have also been carried out in this thesis, in particular an examination of the sensitivity of the carbon cycle to changes in radiative forcing during glacial-interglacial transition as well as abrupt climate changes in the past. Abrupt climate changes are documented in paleoclimate records which reveal that changes in the overturning circulation in the North Atlantic played a key role in these transitions. In order to investigate the response of the carbon cycle to abrupt transitions, we investigate the effects of freshwater forcing in both hemispheres under an LGM climate. In order to simulate possible Heinrich events, meltwater pulses were introduced into the North Atlantic. This reveals that atmospheric CO_2 concentration increases by 14 ppmv, primarily due to a reduction in overturning strength and changes in sea ice extent. The difference in atmospheric CO_2 concentration correspond well with the 15-20 ppmv difference as recorded during strong D-O oscillations (Stauffer et al., 1998).

Southern ocean perturbations have also been examined following Weaver et al. (2003) that suggest meltwater pulse 1A may have originated from the Antarctic ice sheet rather from a northern hemisphere source. By introducing a freshwater pulse just north of the Antarctic Circumpolar Current where AAIW water forms in our model (Saenko et al., 2002), we find a large increase in atmospheric CO_2 concentrations of 32 ppmv. Although this is a much larger change ($\sim$ 25 ppmv) than recorded in Antarctic ice core records from Dome C (Monnin et al., 2001), it is an important result in gaining insight into this period. Overall, this study finds that circulation changes as well as solubility changes affect CO_2 uptake when modelling abrupt changes originating in both hemispheres.

In order to examine the response of the carbon cycle during glacial-interglacial transition, 8 kyr BP boundary conditions were applied to an LGM equilibrium climate, namely orbital parameters corresponding to 8 kyr BP and atmospheric CO_2 radiative forcing set to 280 ppmv. By changing both the orbital forcing and the CO_2 radiative forcing there is little change in the resulting atmospheric CO_2 due to physical processes alone. This finding does not confirm recent box model studies (Toggweiler, 1999; Stephens and Keeling, 2000; Gildor and Tziperman, 2002) which

suggest that an 80 ppmv change in atmospheric CO_2 occurred due to physical processes, in particular changes in Southern Ocean sea ice extent and stratification. Certainly this result yields a large discrepancy between our 3-dimensional GCM and the box model studies, and following Archer et al. (2003) we advise that more work is needed in order to improve our understanding of these differences, certainly regarding the differences in the high latitude sensitivity of these models. As a general consensus, more observational evidence for CO_2 uptake in the high latitude regions, particularly the Southern Ocean are needed to improve validation of our models.

Although we find little overall change in atmospheric CO_2, there are significant changes in the Southern Ocean, indeed the southern hemisphere changes dominate the overall differences in carbon uptake. Changes due to CO_2 radiative forcing from 200 to 280 ppmv are also found to be more important than the difference in uptake due to orbital forcing alone. Although there is a decrease in solubility due to increased SST, which favour outgassing, decreases in sea ice in both hemispheres lead to increased uptake due to greater air-sea interaction. The Southern Ocean dominates the uptake however through a large increase in heat flux throughout, leading to a significant decrease in uptake here. Decreased sea ice cover, primarily in the North Atlantic, mostly counteracts this change however, resulting in a small net increase in atmospheric CO_2.

Overall, this suggests that climate feedbacks affect carbon uptake under both future and paleoclimate perturbations which have been examined in this thesis. This analysis also reveals that changes in uptake are due to several different feedbacks acting on the carbon system including solubility effects, buffering capacity, and changes in sea ice extent and circulation. Another key finding throughout this study is the importance of sea ice and sub-grid-scale mixing parameterizations on carbon uptake. The inclusion of both the Gent McWilliams parameterization for mixing of tracers and a dynamical sea ice component show significant differences in regional carbon uptake and zonal DIC profiles. Significant improvements are seen in the high latitude regions, which are the most important regions for carbon uptake and thus should be included in model studies. Although assessing changes in inorganic ocean carbon uptake under anthropogenic forcing without the consideration of biological processes is perhaps justified, our studies reveal that these processes cannot be overlooked. Certainly when examining glacial-interglacial cycles, we suggest that the inclusion of both biological and carbonate pumps may be important components to unlocking the mystery of these cycles.

Bibliography

Archer, D., Kheshgi, H., Maier-Reimer, E., 1997. Multiple timescales for neutralization of fossil fuel CO_2. Geophys. Res. Lett. 24, 405–408.

Archer, D. E., Martin, P. A., Milovich, J., Brovkin, V., Plattner, G.-K., Ashendel, C., 2003. Model sensitivity in the effect of Antarctic sea ice and stratification on atmospheric pCO_2. Paleoceanography 18(1), 1012, doi:10.1029/2002PA000760.

Archer, D. E., Winguth, A., Lea, D., Mahowald, N., 2000. What caused the glacial/interglacial atmospheric pCO_2 cycles? Reviews of Geophysics 38, 159–189.

Aumont, O., Orr, J. C., Jamous, D., Monfray, P., Marti, O., Madec, G., 1998. A degradation approach to accelerate simulations to steady-state in a 3-D tracer transport model of the global ocean. Clim. Dyn. 14, 101–116.

Barnola, J. M., Raynaud, D., Korotkevich, Y. S., Lorius, C., 1987. Vostok ice cores provides 160,000-year record of atmospheric CO_2. Nature 329, 408–414.

Berger, A. L., 1978. Long-term variations of daily insolation and Quarternary climate change. J. Atmos. Sci. 35, 2362–2367.

Bitz, C. M., Holland, M. M., Weaver, A. J., Eby, M., 2001. Simulating the ice-thickness distribution in a coupled climate model. J. Geophys. Res. 106, 2441–2464.

Bitz, C. M., Lipscomb, W. H., 1999. An energy-conserving thermodynamic model of sea ice. J. Geophys. Res. 104, 15669–15677.

Blunier, T., Brook, E., 2001. Timing of millennial-scale climate change in Antarctica and Greenland during the last glacial period. Science 291, 109–112.

Bolton, D., 1980. The computation of equivalent potential temperature. Mon. Weather Rev. 108, 1046–1053.

Bond, G. C., Lotti, R., 1995. Iceberg discharges into the North Atlantic on millennial time scales during the last glaciation. Science 267, 1005–1010.

Boning, C. W., Holland, W. R., Bryan, F. O., Danabasoglu, G., McWilliams, J. C., 1995. An overlooked problem in model simulations of the thermohaline circulation and heat transport in the Atlantic ocean. J. Clim. 8, 515–523.

Bopp, L., Kohfeld, K. E., Le Quéré, C., Aumont, O., 2003. Dust impact on marine biota and atmospheric CO_2 during glacial periods. Paleoceanography 18(2), doi:10.1029/2002PA000810.

Bopp, L., Le Quéré, C., Heimann, M., Manning, A. C., 2002. Climate-induced oceanic oxygen fluxes: Implications for the contemporary carbon budget. Global Biogeochem. Cycles 16(2), doi:10.1029/2001GB001445.

Boyle, E. A., Keigwin, L. D., 1985. Comparison of Atlantic and Pacific paleochemical records for the last 215,000 years: Changes in deep ocean circulation and chemical inventories. Earth and Planetary Science Letters 76, 135–150.

Broecker, W. S., 1993. The Glacial World According to Wally. Eldigio Press, Palisades, NY.

Broecker, W. S., Ledwell, J. R. Takahashi, T., Weiss, R., Merlivat, L., Memery, L., Peng, T.-H., Jahne, B., Munnich, K. O., 1986. Isotopic versus micrometeorlogic ocean CO_2 fluxes. J. Geophys. Res. 91, 10517–10527.

Broecker, W. S., Peng, T.-H., 1982. Tracers in the sea. Eldigio Press, Palisades, NY.

Bryan, K., 1984. Accelerating the convergence to equilibrium of ocean- climate models. J. Phys. Oceanogr. 14, 666–673.

Bryan, K., Lewis, L., 1979. A water mass model of the world ocean. J. Geophys. Res. 84, 311–337.

Budyko, M. I., 1969. The effect of solar radiation variations on the climate of the earth. Tellus 21, 611–619.

Caldeira, K., Duffy, P. B., 2000. The role of the Southern Ocean in uptake and storage of anthropogenic carbon dioxide. Science 287, 620–622.

Christy, J. R., Clarke, R. A., Gruza, G. V., Jouzel, J., Mann, M. E., Oerlemans, J., Salinger, M. J., Wang, S. W., 2001. Observed Climate Variability and Change. In: Houghton, J. T., Ding, Y., Griggs, D. J., Noguer, M., van der Linden, P. J., Dai, X., Maskell, K., Johnson, C. A. (Eds.), IPCC, Climate Change 2001: The

Scientific Basis. Contribution of Working Group I to the Third Assessment Report of the Intergovernmental Panel on Climate Change. Cambridge University Press, Cambridge, UK.

Clark, P. U., Alley, R. B., Pollard, D., 1999. Northern hemisphere ice-sheet influences on global climate change. Science 286, 1104–1111.

Clark, P. U., Marshall, S. J., Clarke, G. K. C., Hostetler, S. W., Licciardi, J. M., Teller, J. T., 2001. Freshwater forcing of abrupt climate change during the Last Glaciation. Science 293, 283–287.

Clark, P. U., Mitrovica, J. X., Milne, G. A., Tamisiea, M. E., 2002a. Sea-level fingerprinting as a direct test for the source of global meltwater pulse 1A. Science 295, 2438–2441.

Clark, P. U., Mix, A. C., 2002. Ice sheets and sea level of the Last Glacial Maximum. Quaternary Science Reviews 21, 1–7.

Clark, P. U., Pisias, N. G., Stocker, T. F., Weaver, A. J., 2002b. The role of the thermohaline circulation in abrupt climate change. Nature 415, 863–869.

Cox, M. D., 1987. Isopycnal diffusion in a z-coordinate ocean model. Ocean Modelling 74, 1–5.

Cox, P. M., Betts, R. A., Jones, C. D., Spall, S. A., Totterdell, I. J., 2000. Acceleration of global warming due to carbon-cycle feedbacks in coupled model. Nature 408, 184–187.

Crosta, X., Pichon, J. J., 1998. Application of modern analog technique to marine Antarctic diatoms: Reconstruction of maximum sea-ice extent at the Last Glacial Maximum. Paleoceanography 13(3), 284–297.

Crowley, T. J., North, G. R., 1991. In: Paleoclimatology. Oxford Monographs on geology and geophysics. Oxford University Press, New York.

Danabasoglu, G., McWilliams, J. C., 1995. Sensitivity of the global ocean circulation to parametrizations of mesoscale tracer transports. J. Clim. 8, 2967–2987.

Danabasoglu, G., McWilliams, J. C., Gent, P. R., 1994. The role of mesoscale tracer transports in the global ocean circulation. Science 264, 1123–1126.

Dansgaard, W., Johnsen, S. J., Clausen, H. B., Dahl-Jensen, D., Gundestrup, N., Hammer, C. U., 1984. North Atlantic climatic oscillations revealed by deep greenland ice cores. In: Hansen, J. E., Takahashi, T. (Eds.), Climate Processes and Climate Sensitivity. Vol. 29 of Geophysical Monograph Series. American Geophysical Union, Washington, DC, pp. 288–298.

Dickson, A. G., Goyet, C. (Eds.), 1994. DOE, Handbook of methods for the analysis of the various parameters of the carbon dioxide system in sea water. Version 2. ORNL/CDIAC-74.

Duffy, P. B., Eby, M., Weaver, A. J., 2001. Climate model simulations of increased atmospheric CO_2 and loss of sea ice on ocean salinity and tracer uptake. J. Clim. 14, 520–532.

Duffy, P. B., Eltgroth, P., Bourgeois, A. J., Caldeira, K., 1995. Effect of improved subgrid scale transport of tracers on uptake of bomb radiocarbon in the GFDL ocean general circulation model. Geophys. Res. Lett. 22, 1065–1068.

Dutay, J.-C., Bullister, J. L., Doney, S. C., Orr, J. C., Najjar, R., Caldeira, K., Champin, J.-M., Drange, H., Follows, M., Gao, Y., Gruber, N., Hecht, M. W., Ishida, A., Joos, F., Lindsay, K., Madec, G., Maier-Reimer, E., Marshall, J. C., Matear, R. J., Monfray, P., Plattner, G.-K., Sarmiento, J., Schlitzer, R., Slater, R., Totterdell, I. J., Weirig, M.-F., Yamanaka, Y., Yool, A., 2002. Evaluation of ocean model ventilation with CFC-11: comparison of 13 global ocean models. Ocean Modelling 4, 89–120.

England, M. H., 1995. Using chlorofluorocarbons to assess ocean climate Models. Geophys. Res. Lett. , 3051–3054.

Ewen, T. L., Weaver, A. J., Eby, M., 2004a. Sensitivity of the inorganic ocean carbon cycle to future warming in the UVic coupled model. Atmosphere-Ocean 42, 23–42.

Ewen, T. L., Weaver, A. J., Schmittner, A., 2004b. Modelling carbon cycle feedbacks during abrupt climate change. Quaternary Science Reviews 23, 431–448, 10.1016/j.quascirev.2003.08.007.

Fanning, A. F., Weaver, A. J., 1996. An atmospheric energy-moisture balance model: climatology, interpentadal climate change, and coupling to an ocean general circulation model. J. Geophys. Res. 101, 15,111–15,128.

Farquhar, G. D. Fasham, M. J. R., Goulden, M. L., Heimann, M., Jaramillo, V. J., Kheshgi, H. S., Le Quéré, C., Scholes, R. J., Wallace, D. W. R., 2001. The Carbon Cycle and Atmospheric Carbon Dioxide. In: Houghton, J. T., Ding, Y., Griggs, D. J., Noguer, M., van der Linden, P. J., Dai, X., Maskell, K., Johnson, C. A. (Eds.), IPCC, Climate Change 2001: The Scientific Basis. Contribution of Working Group I to the Third Assessment Report of the Intergovernmental Panel on Climate Change. Cambridge University Press, Cambridge, UK.

François, R., Altabet, M. A., Yu, E.-F., Sigman, D. M., Bacon, M. P., Frank, M., Bohrmann, G., Bareille, G., Labeyrie, L. D., 1997. Contribution of Southern Ocean surface-water stratification to low atmospheric CO_2 concentrations during the last glacial period. Nature 389, 929–935.

Friedlingstein, P., Bopp, L., Ciais, P., Dufresne, J.-L., Fairhead, L., LeTreut, H., Monfray, P., Orr, J., 2001. Positive Feedback between future climate change and the carbon cycle. Geophys. Res. Lett. 28, 1543–1546.

Gent, P. R., McWilliams, J. C., 1990. Isopycnal mixing in ocean circulation models. J. Phys. Oceanogr. 20, 150–155.

Gildor, H., Tziperman, E., 2002. Sea ice switch mechanism and glacial-interglacial CO_2 variations. Global Biogeochem. Cycles 16, 10.1029/2001GB001446.

Gill, A. E., 1982. In: Atmosphere-Ocean Dynamics. Vol. 30 of Int. Geophys. Ser. Academic Press, New York, NY, p. 662 pp.

Gloor, M., Gruber, N., Sarmiento, J., Sabine, C. L., Feely, R. A., Rödenbeck, C., 2003. A first estimate of present and preindustrial air-sea CO_2 flux patterns based on ocean interior carbon measurements and models. Geophys. Res. Lett. 30, 10.1029/2002GL015594.

Gnanadesikan, A., Toggweiler, J. R., 1999. Constraints placed by silicon cycling on vertical exchange in general circulation models. Geophys. Res. Lett. 26, 1865–1868.

Graves, C. E., Lee, W. H., North, G. R., 1993. New parametrizations and sensitivities for simple climate models. J. Geophys. Res. 98, 5025–5036.

Grootes, P. M., Stuiver, M., White, J. W. C., Johnson, S., Jouzel, J., 1993. Comparison of oxygen isotope records from the GISP2 and GRIP Greenland ice cores. Nature 366, 552–554.

Gruber, N., 1998. Anthropogenic CO_2 in the Atlantic Ocean. Global Biogeochem. Cycles 12, 165–191.

Gruber, N., Keeling, C. D., Bates, N. R., 2002. Interannual variability in the North Atlantic ocean carbon sink. Science 298, 2374–2378.

Gruber, N., Sarmiento, J. L., Stocker, T. F., 1996. An improved method for detecting anthropogenic CO_2 in the oceans. Global Biogeochem. Cycles 10(4), 809–837.

Heinrich, H., 1988. Origin and consequences of cyclic ice rafting in the Northeast Atlantic Ocean during the past 130,000 years. Quarternary Research 29, 142–152.

Hibler, W. D., 1979. A dynamic thermodynamic sea ice model. J. Phys. Oceanogr. 9, 815–846.

Holland, M. M., Bitz, C. M., Eby, M., Weaver, A. J., 2001. The role of ice ocean interactions in the variability of the North Atlantic thermohaline circulation. J. Clim. 14, 656–675.

Houghton, J. T., Meira Filho, L. G., Callander, B. A., Harris, N., Kattenberg, A., Maskell, K. (Eds.), 1996. IPCC, Climate Change 1995. The Science of Climate Change. Contribution of Working Group I to the Second Assessment Report of the Intergovernmental Panel on Climate Change. Cambridge University Press, Cambridge, UK.

Hunke, E. C., Dukowicz, J. K., 1997. An elastic-viscous-plastic model for sea ice dynamics. J. Phys. Oceanogr. 27, 1849–1867.

Imbrie, J., Berger, A., Boyle, E. A., Clemens, S. C., Duffy, A., Howard, W. R., Kukla, G., Kutzbach, J., Martinson, D. G., McIntyre, A., Mix, A. C., Molfino, B., Morley, J. J., Peterson, L. C., Pisias, N. G., Prell, W. L., Raymo, M. E., Shackleton, N. J., Toggweiler, J. R., 1993. On the structure and origin of major glaciation cycles. Paleoceanography 8, 699–735.

Imbrie, J., Boyle, E. A., Clemens, S. C., Duffy, A., Howard, W. R., Kukla, G., Kutzbach, J., Martinson, D. G., McIntyre, A., Mix, A. C., Molfino, B., Morley, J. J., Peterson, L. C., Pisias, N. G., Prell, W. L., Raymo, M. E., Shackleton, N. J., Toggweiler, J. R., 1992. On the structure and origin of major glaciation cycles: 1. linear responses to Milankovitch forcing. Paleoceanography 7, 701–738.

Indermühle, A., Monnin, E., Stauffer, B., Stocker, T. F., 2000. Atmospheric CO_2 concentration from 60 to 20 kyr BP from the Taylor Dome ice core, Antarctica. Geophys. Res. Lett. 27, 735–738.

Indermühle, A., Stocker, T. F., Joos, F., Fischer, H., Smith, H. J., Wahlen, M., Deck, B., Mastroianni, D., Tschumi, J., Blunier, T., Meyer, R., Stauffer, B., 1999. Holocene carbon-cycle dynamics based on CO_2 trapped in ice at Taylor Dome, Antarctic. Nature 398, 121–126.

Isemer, H. J., Willebrand, H., Hasse, L., 1989. Fine adjustment of large scale air-sea energy flux parametrizations by direct estimates of ocean heat transport. J. Climate 2, 1173–1184.

Jones, E. P., Nelson, D. M., Treguer, P., 1990. Chemical Oceanography. In: Smith Jr., W. O. (Ed.), Polar Oceanography: Part B Chemistry, Biology and Geology. Academic Press, London.

Joos, F., Plattner, G., Stocker, T. F., Marchal, O., 1999. Global warming and marine carbon cycle feedbacks on future atmospheric CO_2. Science 284, 464–467.

Kalnay, E., Kanamitsu, M., Kistler, R., Collins, W., Deavon, D., Gandin, L., Iredell, M., Saha, S., White, G., Woollen, J., Zhu, Y., Leetmaa, A., Reynolds, R., 1996. The NCEP/NCAR 40 year reanalysis project. Bull. Am. Meteorol. Soc. 77, 431–471.

Keeling, R. F., Peng, T.-H., 1995. Transport of heat, CO_2 and O_2 by the Atlantic's thermohaline circulation. Phil. Trans. R. Soc. Lond. B 348, 133–142.

Le Quéré, C., Orr, J. C., Monfray, P., Aumont, O., Madec, G., 2000. Interannual variability of the oceanic sink of CO_2 from 1979 through 1997. Global Biogeochem. Cycles 14, 1247–1265.

MacAyeal, D. R., 1993. Binge/purge oscillations of the Laurentide ice sheet as a cause of the North Atlantic's Heinrich events. Paleoceanography 8, 775–784.

Madec, G., Imbard, M., 1996. A global ocean mesh to overcome the North Pole singularity. Clim. Dyn. 12, 381–388.

Maier-Reimer, E., 1993. Geochemical cycles in an ocean general circulation model: Preindustrial tracer distributions. Global Biogeochem. Cycles 7, 645–677.

Maier-Reimer, E., Hasselmann, K., 1987. Transport and storage of CO_2 in the ocean - an inorganic ocean-circulation carbon cycle model. Clim. Dyn. 2, 63–90.

Manabe, S., Stouffer, R. J., 1994. Multiple century response of a coupled ocean-atmosphere model to an increase of atmospheric carbon dioxide. J. Clim. 7, 5–23.

Manabe, S., Stouffer, R. J., 1995. Simulation of abrupt climate change induced by freshwater input to the North Atlantic Ocean. Nature 378, 165–167.

Manabe, S., Stouffer, R. J., 1999. Are two modes of the thermohaline circulation stable? Tellus 51A, 400–411.

Marchal, O., Stocker, T. F., Joos, F., 1998. Impact of oceanic reorganizations on the ocean carbon cycle and atmospheric carbon dioxide content. Paleoceanography 13, 225–244.

Marchal, O., Stocker, T. F., Joos, F., Indermühle, A., Blunier, T., Tschumi, J., 1999. Modelling the concentration of atmospheric CO_2 during the Younger Dryas climate event. Clim. Dyn. 15, 341–354.

Marshall, S. J., Clarke, G. K. C., 1997. A continuum mixture model of ice stream thermomechanics in the Laurentide Ice Sheet, II, Application to the Hudson Strait Ice Stream. J. Geophys. Res. 102, 20615–20638.

Martin, J. H., 1990. Glacial-interglacial CO_2 change; the iron hypothesis. Paleoceanography 5, 1–13.

Matear, R., Hirst, A. C., 1999. Climate change feedback on the future oceanic CO_2 uptake. Tellus 51B, 722–733.

McNeil, B. I., Matear, R. J., Key, R. M., Bullister, J. L., Sarmiento, J. L., 2003. Anthropogenic CO_2 uptake by the ocean based on the global chlorofluorocarbon data set. Science 299, 235–239.

McPhee, M. G., 1992. Turbulent heat flux in the upper ocean sea ice. J. Geophys. Res. 97, 5365–5379.

Mitchell, J. F. B., Johns, T. C. Gregory, J. M., Tett, S. F. B., 1995. Climate response to increasing levels of greenhouse gases and sulphate aerosols. Nature 376, 501–504.

Monnin, E., Indermühle, A., Dällenbach, A., Flückiger, J., Stauffer, B., Stocker, T. F., Raynaud, D., Barnola, J.-M., 2001. Atmospheric CO_2 concentrations over the last glacial termination. Science 291, 112–114.

Murnane, R. J.and Sarmiento, J. L., Le Quéré, C., 1999. Spatial distribution of air-sea CO_2 fluxes and the interhemispheric transport of carbon by the oceans. J. Atmos. Sci. 13, 287–305.

North, G. R., 1975. Theory of energy balance climate models. J. Atmos. Sci. 32, 2033–2043.

Oeschger, H., Beer, J., Siegenthaler, U., Stauffer, B., 1984. Late glacial climate history from ice cores. In: Hansen, J. E., Takahashi, T. (Eds.), Climate Processes and Climate Sensitivity. Vol. 29 of Geophysical Monograph Series. American Geophysical Union, Washington, DC, pp. 299–306.

Orr, J. C., Maier-Reimer, E., Mikolajewicz, U., Monfray, P., Sarmiento, J. L., Toggweiler, J. R., Taylor, N. K., Palmer, J., Gruber, N., Sabine, C. L., 2001. Estimates of anthropogenic carbon uptake from four three-dimensional global ocean models. Global Biogeochem. Cycles 15, 43–60.

Orr, J. C., Najjar, R., Sabine, C. L., Joos, F., 1999. Abiotic-HOWTO. Internal OCMIP report LSCE/DEA Saclay, Gif-sur-Yvette, France, 25 pp.

Pacanowski, R., 1995. MOM 2 Documentation User's Guide and Reference Manual. GFDL Ocean Group Technical Report NOAA, GFDL, Princeton, 232pp.

Pagani, M., Arthur, M. A., Freeman, K. H., 1999. Miocene evolution of atmospheric carbon dioxide. Paleoceanography 14, 273–292.

Pearson, P. N., Palmer, M. R., 2000. Atmospheric carbon dioxide concentrations over the past 60 million years. Nature 406, 695–699.

Peixoto, J. P., Oort, A. H., 1992. Physics of Climate. American Institute of Physics.

Peltier, W. R., 1994. Ice age paleotopography. Science 265, 195–201.

Petit, J. R., Jouzel, J., Raynaud, D., Barkov, N. I., Barnola, J. M., Basile, I., Benders, M., Chappellaz, J., Davis, M., Delaygue, G., Delmotte, M., Kotlyakov, V. M., Legrand, M., Lipenkov, V. Y., Lorius, C., Pépin, L., Ritz, C., Saltzman, E., Stievenard, M., 1999. Climate and atmospheric history of the past 420,000 years from the Vostok ice core, Antarctic. Nature 399, 429–436.

Plattner, G.-K., Joos, F., Stocker, T. F., Marchal, O., 2001. Feedback mechanisms and sensitivities of ocean carbon uptake under global warming. Tellus 53B, 564–592.

Ramanathan, V., Sallis, L., Cess, R., Hansen, J., Isaksen, I., Kuhn, W., Lacis, A., Luther, F., Mahlman, J., Reck, R., Schlesinger, M., 1987. Climate-chemical interactions and effects of changing atmospheric trace gases. Rev. of Geophys. 25, 1441–1482.

Redi, M. H., 1982. Oceanic isopycnal mixing by coordinate rotation. J. Phys. Oceanogr. 12, 1154–1158.

Robitaille, D. Y., Weaver, A. J., 1995. Validation of sub-grid-scale mixing schemes using CFCs in a global ocean model. Geophys. Res. Lett. 22, 2917–2920.

Sabine, C. L., Key, R. M., Johnson, K. M., Millero, F. J., Poisson, A., Sarmiento, J. L., Wallace, D. W. R., Winn, C. D., 1999. Anthropogenic CO_2 inventory of the Indian Ocean. Global Biogeochem. Cycles 13, 179–198.

Saenko, O., Schmittner, A., Weaver, A. J., 2002. On the role of wind-driven sea ice motion on ocean ventilation. J. Phys. Oceanogr. 12, 3376–3395.

Sarmiento, J. L., Hughes, T. M. C., Stouffer, R. J., 1998. Simulated response of the ocean carbon cycle to anthropogenic climate warming. Nature 393, 245–249.

Sarmiento, J. L., Le Quéré, C., 1996. Oceanic carbon dioxide uptake in a model of century-scale global warming. Science 274, 1346–1350.

Sarmiento, J. L., Monfray, P., Maier-Reimer, E., Aumont, O., Murnane, R. J., Orr, J. C., 2000. Sea-air CO_2 fluxes and carbon transport: A comparison of three ocean general circulation models. Global Biogeochem. Cycles 14, 1267–1281.

Sarmiento, J. L., Murnane, R. J., Le Quéré, C., 1995. Air-sea CO_2 transfer and the carbon budget of the North Atlantic. Phil. Trans. R. Soc. Lond. B 348, 211–219.

Sarmiento, J. L., Orr, J. C., 1992. A Perturbation Simulation of CO_2 Uptake in an Ocean General Circulation Model. J. Geophys. Res. 97, 3621–3645.

Sarmiento, J. L., Toggweiler, J. R., 1984. A new model for the role of the oceans determining atmospheric pCO_2. Nature 308, 621–624.

Schmittner, A., 2003. Southern Ocean sea ice and radiocarbon ages of glacial bottom waters. Earth and Planetary Science Letters, 213, 53–62.

Schmittner, A., Weaver, A. J., 2001. Dependence of multiple climate states on ocean mixing parameters. Geophys. Res. Lett. 28, 1027–1030.

Schmittner, A., Yoshimori, M., Weaver, A. J., 2002. Instability of glacial climate in a model of the ocean-atmosphere-cryosphere system. Science 295, 1489–1493.

Sellers, W. D., 1969. A global climatic model based on the energy balance of the Earth-atmosphere system. J. Appl. Meteorol. 8, 392–400.

Semtner, A. J., 1976. A model for the thermodynamic growth of sea ice in numerical investigations of climate. J. Phys. Oceanogr. 6, 379–389.

Siegenthaler, U., Oeschger, H., 1978. Predicting future atmospheric carbon-dioxide levels. Science 199, 388–395.

Sigman, D. M., Boyle, E. A., 2000. Glacial/interglacial variations in atmospheric carbon dioxide. Nature 407, 859–869.

Sigman, D. M., McCorkle, D. C., Martin, W. R., 1998. The calcite lysocline as a constraint on glacial/interglacial low-latitude production changes. Global Biogeochem. Cycles 12, 409–427.

Simmons, H. L., Jayne, S. R., St. Laurent, L. C., Weaver, A. J., 2004. Tidally driven mixing in a numerical model of the ocean general circulation. Ocean Modelling 6, 245–263.

Stauffer, B., Blunier, T., Dällenbach, A., Indermühle, A., Schwander, J., Stocker, T. F., Chappellaz, J., Raynaud, D., Hammer, C. U., Clausen, H. B., 1998. Atmospheric CO_2 concentration and millennial-scale climate change during the last glacial period. Nature 392, 59–62.

Stephens, B. B., Keeling, R. F., 2000. The influence of Antarctic sea ice on glacial-interglacial CO_2 variations. Nature 404, 171–174.

Stocker, T. F., 2000. Past and future reorganisations in the climate system. Quaternary Science Reviews 19, 301–319.

Stocker, T. F., Broecker, W. S., Wright, D. G., 1994. Carbon uptake experiments with a zonally averaged global circulation model. Tellus 46B, 103–122.

Stocker, T. F., Schmittner, A., 1997. Influence of CO_2 emission rates on the stability of the thermohaline circulation. Nature 388, 862–865.

Takahashi, T., Feely, R. A., Weiss, R. F., Wanninkhof, R. H., Chipman, D. W., Sutherland, S. C., Takahashi, T. T., 1997. Global air-sea flux of CO_2: An estimate based on measurements of sea-air pCO_2 difference. Proc. Natl. Acad. Sci. 94, 8292–8299.

Thompson, S. L., Warren, S. G., 1982. Parameterization of outgoing infrared radiation derived from detailed radiative calculations. J. Atmos. Sci. 39, 2667–2680.

Toggweiler, J. R., 1999. Variation of atmospheric CO_2 by ventilation of the ocean's deepest water. Paleoceanography 14, 571–588.

Wallace, D. W. R., 2001. Storage and Transport of Excess CO_2 in the Oceans: The JGOFS/WOCE Global CO_2 Survey. In: Siedler, G., Church, J., Gould, J. (Eds.), Ocean Circulation and Climate: Observing and Modelling the Global Ocean. Vol. 77 of International Geophysics Series. Academic Press, London, p. 715 pp.

Wanninkhof, R., 1992. Relationship between wind speed and gas exchange over the ocean. J. Geophys. Res. 97, 7373–7328.

Weaver, A. J., 1999. Millennial timescale variability in ocean/climate models. In: Clark, P. U., Webb, R. S., Keigwin, L. D. (Eds.), Mechanisms of Global Climate Change at Millenial Time Scales. Vol. 112 of Geophysical Monograph Series. American Geophysical Union, Washinton, DC, pp. 285–300.

Weaver, A. J., Duffy, P. B., Eby, M., Wiebe, E. C., 2000. Evaluation of ocean and climate models using present-day observations and forcing. Atmosphere-Ocean 38, 271–301.

Weaver, A. J., Eby, M., Wiebe, E. C., Bitz, C. M., Duffy, P. B., Ewen, T. L., Fanning, A. F., Holland, M. M., MacFayden, A., Saenko, O., Schmittner, A., Wang, H., Yoshimori, M., 2001. The UVic Earth System Climate Model: Model description, climatology, and applications to past, present and future climates. Atmosphere-Ocean 39, 361–428.

Weaver, A. J., Fanning, A. F., Eby, M., Wiebe, E. C., 1998. Simulated influence of carbon dioxide, orbital forcing and ice sheets on the climate of the Last Glacial Maximum. Nature 394, 847–853.

Weaver, A. J., Saenko, O. A., Clark, P. U., Mitrovica, J. X., 2003. Meltwater pulse 1A from the Antarctic ice sheet as a trigger of the Bølling-Allerød warm interval. Science 299, 1709–1713.

Yoshimori, M., Weaver, A. J., Marshall, S. J., Clark, G. K. C., 2001. Glacial termination: sensitivity to orbital and CO_2 forcing in a coupled climate system model. Climate Dynamics 17, 571–588.